

Development of front suspension for an electric two-wheeled amphibious vehicle

JOAKIM LANGE

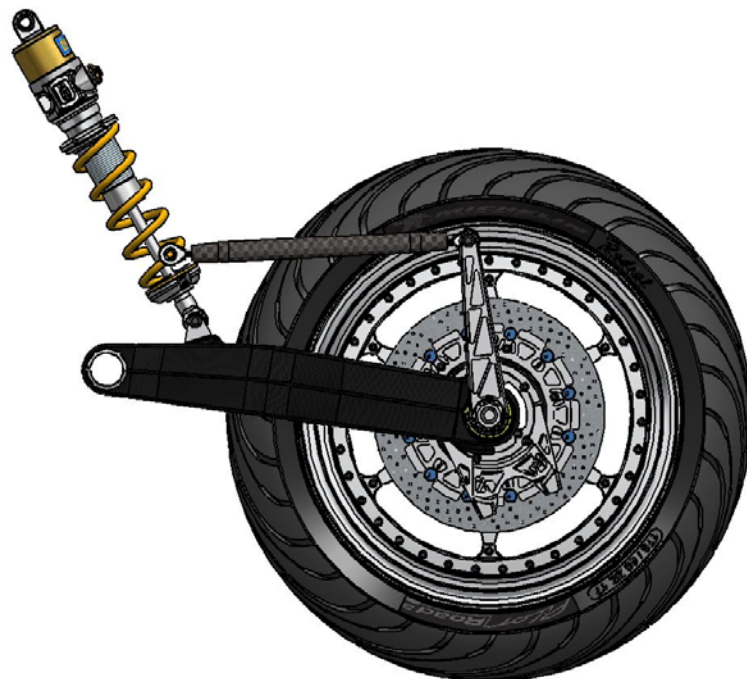


**KTH Industrial Engineering
and Management**

Master of Science Thesis
Stockholm, Sweden 2015

Development of front suspension for an electric two-wheeled amphibious vehicle

Joakim Lange



Master of Science Thesis MMK 2015:12 MKN 130
KTH Industrial Engineering and Management
Machine Design
SE-100 44 STOCKHOLM



KTH Industriell teknik
och management

Utveckling av framhjulsupphängning till en elektrisk tvåhjulig amfibiefarkost

Joakim Lange

Godkänt 2015-04-07	Examinator Ulf Sellgren	Handledare Stefan Björklund
	Uppdragsgivare Ivan Stenius	Kontaktperson Mikael Nybacka

SAMMANFATTNING

Examensarbetet som följer i denna rapport är en del i ett större utvecklingsprojekt som startades på KTH Marina System. Målet med projektet är att utveckla och tillverka en fullskalig prototyp av ett tvåhjuligt elektriskt framdrivet amfibiefordon. Examensarbetets fokus ligger på utvecklingen av fordonets framhjulsupphängning.

I nuläget existerar endast en grov konceptuell idé över hela fordonet och dess framhjulsupphängning. Målet med examensarbetet är att analysera, utvärdera och välja en passande lösning för främre hjulsupphängningen och implementera i en detaljerad konceptuell konstruktion. Eftersom resten av fordonet ännu inte har utvecklats existerar inga direkta angränsande system för konstruktionen. Den föreslagna konstruktionen kommer därför med hög sannolikhet behöva revideras när utvecklingen av fordonet går framåt. För att underlätta ändringar ska konstruktionen vara parametrerad. En annan del av examensarbetet är att ta fram utvecklingsmodeller, även dom parametrerade, som kommer att nyttjas i konstruktionsarbetet. Modellerna anses också som leverabler eftersom de även kommer att användas när konstruktionen behöver revideras för att passa samman med resten av fordonet.

Den information som återfinns i den konceptuella iden över fordonet användes för att ta fram en uppskattning för positionen av fordonets masscentrum. Med hjälp av denna position har ett antal parametrerade analytiska modeller tagits fram och använts för att konstruera en hjulsupphängningsgeometri. Geometrin har optimerats för så kallade anti-dive egenskaper, egenskaper som förhindrar att fordonets nos dyker vid kraftiga inbromsningar. De analytiska modellerna har validerats genom att en parametrerad ADAMS View modell av fordonet har tagits fram.

The resulterande främre hjulsupphängningen är en symmetrisk swingarm med navstyrning, momentarmar och styrlänkar. En elektrisk navmotor är implementerad i hjulet för att tillföra drivkraft till framvagnen. De olika delarna har skapats i Solid Edge ST5 CAD programvara och förenklade hållfasthetsanalyser har genomförts i Ansys Workbench 14.0.

På grund av beroendet mot det resterande fordonet som konstruktionen lider av måste den anses som en konceptuell sammanställningsritning av den slutgiltiga framhjulsupphängningen. Utan några förutbestämda konstruktionsavgränsningar från övriga system behöver komponenterna utvecklas parallellt och iterativt.



KTH Industrial Engineering
and Management

Development of front suspension for an electric
two-wheeled amphibious vehicle

Joakim Lange

Approved 2015-04-07	Examiner Ulf Sellgren	Supervisor Stefan Björklund
	Commissioner Ivan Stenius	Contact person Mikael Nybacka

ABSTRACT

This master thesis is a part of a larger development project initiated at the department of Naval Architecture at KTH. The project goal is to design and manufacture a full scale proof-of-concept prototype of a electric powered two-wheeled amphibious vehicle. The focus of this thesis is the vehicle's front suspension system.

In the present state, only a rough conceptual idea exist of the overall vehicle and its front suspension. The aim of this thesis is to analyze, evaluate and choose a suitable front suspension system and implement it into a detailed conceptual design. The rest of the vehicle is yet to be developed why the design boundaries for the front suspension are open-ended. This means that the design is likely to be revised in continued development. To deal with the open-ended boundaries a parameterized design is requested. An additional segment of the thesis is to produce parameterized development models used to derive the design. These models are considered as deliverables since they will be used when revising the front suspension for it to conform with the rest of the vehicle.

With the information provided by the existing rough concept in terms of major components and vehicle architecture an estimation of the centre of gravity location have been carried out. This location enables a number of parameterized analytical models to be derived and utilized in the design of an optimized front suspension anti-dive geometry. The analytical models have been validated by creating a parametric ADAMS View model of the vehicle with a main purpose of simulating vehicle dynamics.

The resulting design is a symmetric front swing arm suspension with a hub centre steering, torque arms and guide struts. An electric hub motor is also implemented in the wheel to provide tractive power in the front. The subsystem detailed conceptual design have been created in Solid Edge ST5 CAD software. Simplified finite element structural analysis in Ansys Workbench 14.0 is used to provide an initial estimate of the factor of safety for the parts.

Because of the influence of the rest of the vehicle the proposed design delivered by this thesis is to be reviewed as a conceptual blueprint for the final front suspension. As there is no pre-existing design constraints from the rest of the vehicle the different subsystems are required to be parallel and iteratively developed due to their cross dependence.

FOREWORD

The first person I would like to express appreciation for is Linus Fagerberg, CEO of *Lightness by design* and part time employee at KTH Centre for Naval Architecture. Linus was the link between me and Ivan Stenius, the thesis commissioner, and has therefore played a huge role in me attaining this thesis.

Secondly, much gratitude to Ivan Stenius who provided me with the thesis and whose commitment and dedication to the Newt project have resulted in rewarding discussions and inputs during the work process.

I would also lay down a big "thank you" to my supervisors Mikael Nybacka and Stefan Björklund who have contributed immensely with valuable feedback. Extra credit should go to Mikael with his help and expertise concerning ADAMS modeling and simulations.

Lastly I like to thank Peter Georén of KTH Integrated Transport Research Labs who has let me reside in their facilities and who has been a great company during lunches and coffee breaks.

Joakim Lange

Stockholm, April 2015

NOMENCLATURE & USED SOFTWARE

Notations and Abbreviations are continuously explained throughout the master thesis, a summary of these are presented in the lists below.

Abbreviations

<i>ADR</i>	Anti-dive ratio
<i>ALR</i>	Anti-lift ratio
<i>BR</i>	Brake ratio
<i>CAD</i>	Computer aided design
<i>CFD</i>	Computational fluid dynamics
<i>CFRP</i>	Carbon fiber reinforced plastic
<i>CoG</i>	Centre of Gravity
<i>CoP</i>	Centre of Pressure
<i>DV</i>	Design variables
<i>FEA</i>	Finite element analysis
<i>FEM</i>	Finite element method
<i>FOS</i>	Factor of safety
<i>HP</i>	Hardpoints
<i>IC</i>	Instant center
<i>IP</i>	Ingress protection
<i>IR</i>	Installation ratio
<i>ITRL</i>	Integrated transport research labs
<i>MBS</i>	Multibody system
<i>RR</i>	Ride rate

Used software

<i>Matlab</i>	MathWorks [®] , Inc. <i>version</i> R2014b
<i>ADAMS view</i>	MSC Software [®] Corp. <i>version</i> 2012
<i>Ansys Workbench</i>	ANSYS [®] , Inc. <i>version</i> 14.0
<i>Solid Edge</i>	Siemens PLM Software, Inc. <i>version</i> ST5

Notations

Symbol	Description
A	Frontal area, m^2
b	Wheelbase, mm
C_D	Coefficient of drag
C_L	Coefficient of lift
C_R	Rolling resistance coefficient
c_w	Wheel center damping rate, Ns/m
F_c	Wheel damper force, N
F_D	Drag force, N
F_f	Front tractive force, N
F_L	Lift force, N
f_n	Natural frequency, Hz
F_r	Rear tractive force, N
F_t	Tire spring force, N
F_w	Wheel spring force, N
g	Gravitational acceleration, m/s^2
h_g	Vertical distance from ground to CoG, mm
h_p	Vertical distance from ground to CoP, mm
IC_x	Horizontal distance from wheel center to IC, mm
IC_y	Vertical distance from wheel center to IC, mm
k_t	Tire spring rate, N/m
k_w	Wheel center rate, N/m
L_1	Swing arm length, mm
L_2	Torque arm length, mm
L_3	Torque strut length, mm
L_4	Distance between chassis HP, mm
L_{v1}	Torque strut virtual link arm, mm
L_{v2}	Swing arm virtual link arm, mm
L_d	Suspension linkage virtual diagonal, mm
l_x	Horizontal distance from torque arm HP to IC, mm
l_y	Vertical distance from torque arm HP to IC, mm
m	Total vehicle mass, kg
m_u	Mass of unsprung components, kg

m_v	Half vehicle mass, kg
N_f	Front normal load, N
N_r	Rear normal load, N
R_f	Front rolling resistance force, N
R_r	Rear rolling resistance force, N
r	Tire unloaded radius, mm
r_t	Tire rolling radius, mm
r_k	Stiffness ratio
ΔWT_x	Maximum allowed horizontal wheel displacement, mm
x_g	Horizontal distance from front wheel to CoG, mm
x_i	Horizontal distance from wheel center to torque arm HP, mm
x_p	Horizontal distance from front wheel to CoP, mm
y_0	Vertical distance from ground to chassis swing arm HP, mm
y_A	Vertical distance from ground to wheel swing arm HP, mm
y_g	Ground coordinate, mm
y_i	Vertical distance from wheel center to torque arm HP, mm
y_u	Unsprung coordinate, mm
y_v	Suspended mass coordinate, mm
α	Suspension linkage angle 1, rad
β	Suspension linkage angle 2, rad
γ	Torque arm angle, calculated in rad but presented in deg
$\Delta\gamma_{max}$	Maximum torque arm angular change, calculated in rad but presented in deg
ε_{id}	Ideal brake ratio
ζ_w	Wheel damping ratio
θ_1	Swing arm angle 1, rad
θ_2	Swing arm angle 2, rad
θ_3	Torque strut angle, rad
μ_t	Tire friction coefficient
ζ_F	Anti-dive angle, rad
ζ_R	Anti-lift angle, rad
ρ	Ambient air density, kg/m^3
φ	Angle between chassis HP, calculated in rad but presented in deg
ψ	Road inclination angle, calculated in rad but presented in deg
ω_d	Damped natural frequency, rad/s
ω_n	Natural frequency, rad/s

TABLE OF CONTENTS

SAMMANFATTNING	i
ABSTRACT	iii
FOREWORD	v
NOMENCLATURE & USED SOFTWARE.....	vii
TABLE OF CONTENTS	xi
1 INTRODUCTION	1
1.1 Background	1
1.2 Purpose	3
1.3 Delimitations	3
2 METHOD	5
3 FRAME OF REFERENCE.....	7
3.1 Preliminary design and vehicle architecture	7
3.2 Balance of two-wheeled vehicle.....	9
3.3 Benchmarking - suspension.....	12
3.4 Benchmarking - vehicles	17
3.5 Component search - hub motor	18
4 DESIGN FOUNDATION.....	21
4.1 Suspension type evaluation	21
4.2 Vehicle coordinate system.....	22
4.3 Simple CAD model	23
5 ANALYTICAL MODELS	27
5.1 Rigid vehicle model.....	27
5.2 Kinematic analysis model	32
5.3 Anti-dive model.....	36
5.4 Ideal braking model.....	39
5.5 Optimization.....	44
5.6 Transient half vehicle model	49
6 ADAMS MODEL.....	53
6.1 Building the model	53
6.2 Load case for structural analysis	56
7 VALIDATING THE MODELS	59
7.1 Longitudinal dynamics	59
7.2 Transient suspension	63

8	DETAILED CONCEPT DESIGN.....	65
8.1	Main assembly.....	65
8.2	Front wheel.....	67
8.3	Swing arm, torque struts and torque arms.....	75
9	DISCUSSION AND CONCLUSIONS	79
9.1	Discussion	79
9.2	Conclusions	80
10	RECOMMENDATIONS AND FUTURE WORK	81
10.1	Recommendations	81
10.2	Future work	81
11	REFERENCES	83
APPENDIX I	- OPTIMIZATION PRINT-OUT	I
APPENDIX II	- PRELOAD ITERATIONS	III
APPENDIX III	- STRUCTURAL ANALYSIS	V
APPENDIX IV	- KINEMATIC ANALYSIS M-CODE	XI

1 INTRODUCTION

The introduction chapter explains the background to the thesis and the previously conducted work in the overall project of developing the amphibious vehicle. The purpose and deliverables of the thesis deliverables are also established together with the delimitations of the project.

1.1 Background

A project has been launched at the KTH Centre for Naval Architecture, aiming to develop a small two-wheeled amphibious commuter vehicle. The general vehicle concept together with the overall dimensions has been derived by the project initiators prior to this thesis. After generating design sketches and ideas a preliminary design has been established and illustrated in Figure 1.1.

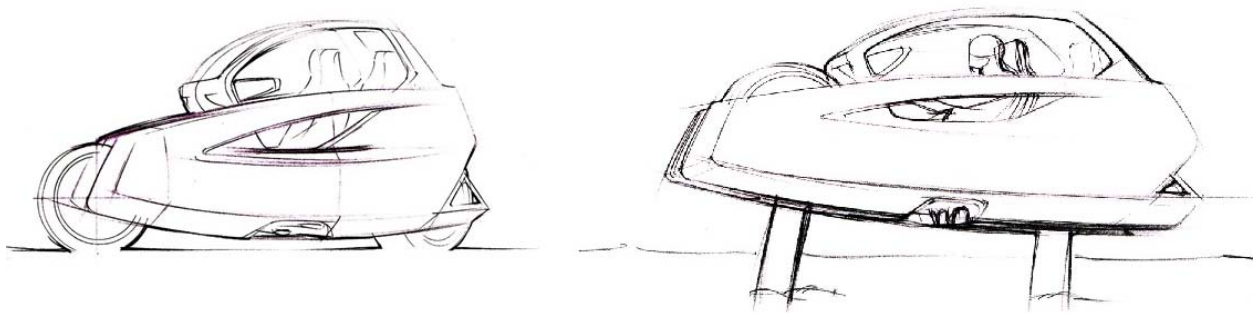


Figure 1.1. The design sketches showing the amphibious vehicle in land and hydrofoil flying mode (Newt, 2013).

The two-wheeled multimodal vehicle, named **Newt**, is fully encapsulated and provides seating for two persons. The three modes in which Newt operates are, land mode, displacement mode and flying mode where the two latter are immersed in water (Sundberg, 2014). On land Newt is powered by electric hub motors and features motorcycle style tires to be able to bank when cornering. Upon water entry the wheels shall retract into the body and two hydrofoils folds out. In sea-mode the propulsion will be provided by two pod-drives located on the aft foil. In order for Newt to maintain upright, especially at low speeds, both when in land- and sea-mode the plan is to utilize active gyroscopic stabilization (Newt, 2013). A Simulink model of this balancing device is being continuously developed by the faculty at Naval Architecture and have been the main focus of Newts development so far.

1.1.1 Existing concept idea

A preliminary design proposal based on the information gathered from the mock-up model has been modeled using the Rhinoceros 3D CAD software from Robert McNeel & Associates. The Rhino model feature a simplified design geometry and should be considered as a conceptual technology demonstrator and as a rough first draft of the vehicle. Figure 1.2 shows the existing concept design with deployed hydrofoils and retracted wheels.

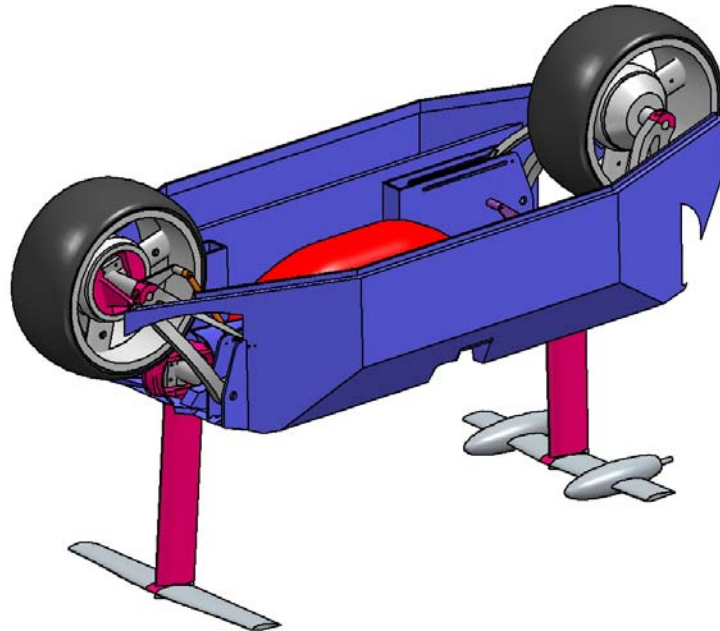


Figure 1.2. The Rhino model of Newt without the top piece, retracted wheels and deployed hydrofoils.

1.1.2 Problem description

The intention of the project is to build a fully functioning proof-of-concept prototype of the vehicle. The conceptual ideas must therefore undergo a development process to reach a point where manufacturing may commence. The subsystems of interest in this thesis are the front suspension and the front unsprung assembly.

Mikael Nybacka, Assistant Professor at the Division of Vehicle Dynamics at KTH, has shortly prior to this thesis been involved in the project. With his influence tasks relating to vehicle dynamics has also been added to the thesis. When Newt operates in land mode it will behave as a banking round-bound vehicle and consequently its driving dynamics needs to be modeled and analyzed.

Being a proof-of-concept the prototype need no adaptation for a larger series and as expressed by Ivan Stenius, the thesis commissioner, it should project a futuristic lightweight design and feature fibre composites where applicable.

The front suspension and front unsprung subsystem in the Rhino model are featured at a level of detail which indicates that the suspension and steering concept are decided. Ivan Stenius have conveyed that these choices of concepts are not definite and may well change if another conceptual subsystem proves to be better suited for the application.

With the vehicle only existing as a conceptual idea the various parts are yet to be designed and consequently the components are highly cross dependent. With no fixed interfaces, designs will influence each other and this require an iterative design process where development of parts progresses in parallel. The parallel design workflow implies that subsystems cannot be designed standalone of other sections of the vehicle. With the thesis limited to only focus on the front suspension there is no meaning of reaching a finalized detailed design since it must be later modified to conform with the rest of the vehicle. To cope with the cross linked dependence *parametric detailed conceptual designs* are introduced. With parameterization the models are quickly and easily altered to new specifications and the detailed conceptual design give the possibility to iterate between subsystems and refine the components.

1.2 Purpose

The purpose of the thesis is to *examine* and *evaluate* the conceptual ideas illustrated by the Rhino model and also *investigate* alternative front suspensions. The knowledge acquired through this analysis is then used to produce a *detailed conceptual design* of the front suspension and front unsprung assembly. A vital part of the thesis is to produce parametric development models used to simulate different elements of the vehicle, e.g. kinematics and dynamics.

The deliverables at the end of the thesis are:

- Parametric kinematic model of the front suspension.
- Parametric ADAMS MBS model of front suspension and front unsprung assembly.
- Parametric CAD model of suggested design of front suspension and front unsprung assembly.

1.3 Delimitations

To define the boundaries of the thesis, the scope of the project is restricted by enforcing delimitations concerning both the analysis and the actual design.

- The only operational mode considered in the thesis is the land based mode, where Newt is a road vehicle.
- The analysis of Newt is restricted to only cover in-plane dynamics, meaning that out-of-plane events like cornering is disregarded.
- Detailed tire modeling is not included in the dynamic analysis.
- The steering actuation system is completely ignored in the design of the front wheel subsystem.
- The design of the brake discs and brake calipers are not considered.

2 METHOD

This short chapter describes the method used to be able to fulfill the thesis deliverables and purpose.

A common and generally accepted approach to product development has been derived by professors Karl T. Ulrich and Steven D. Eppinger. Their process consist of five intrinsic development stages which are illustrated in Figure 2.1.

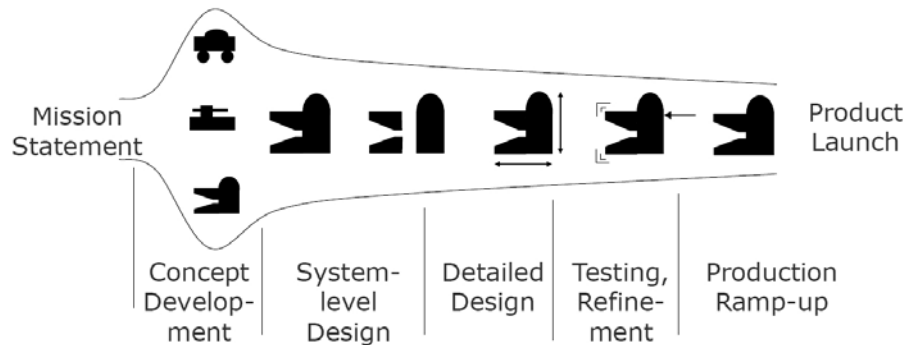


Figure 2.1. The different stages of the product development process (Ulrich & Eppinger, 2011).

The steps in the Ulrich & Eppinger model represent the phases that the overall product undergoes during development. Within these steps the product is decomposed into subsystems consisting of individual parts. On subsystem-/part-level another round of concepts are generated for that particular system and then developed into a viable subsystem design. Benchmarking other products/subsystems is also common practice when generating concepts. By this process the final design of the entire product emerges and may continue into the next step (Ulrich & Eppinger, 2011).

To get an understanding of the overall vehicle and establishing the general design constraints for the thesis the *Rhino model* is studied. The necessary information from this model is extracted while also *preliminary design choices* are determined.

The two-wheeled design of Newt makes the vehicle sensitive to lateral disturbances and prone to capsize if not rebalanced. The gyroscopic balancing unit will strive to keep the vehicle stable, however looking to already existing two-wheelers like motorcycles it is apparent they can remain balanced without such technology. *Analyzing design considerations* and *balancing mechanics* is essential when designing a new front suspension.

To the knowledge of the project initiators, there is no other vehicle like Newt existing in the world, so benchmarking the entire vehicle is not possible, however Newt's inherent subsystems are found in other applications. There is also the possibility that there are other vehicles equivalent to one of the different modes that Newt can take on, for instance the land or flying mode. Another type of suspension than featured in the Rhino model could also be better suited for the vehicle. A *benchmarking* study for similar vehicles and subsystems is going to be conducted and may provide useful ideas and input for the detailed conceptual design.

The most design influential and vital component that will either be purchased or outsourced are the hub motors. A *component search* will be used in order to find suitable motors.

When a principal system design is established, the design phase can be initiated by deriving a kinematic analysis of the suspension. With Matlab, a multivariable *optimization* routine can be programmed to find a suspension geometry that ensures desired kinematic behavior. A simplified

transient vehicle model is also to be programmed in Matlab to derive appropriate spring and damping rates. When designing individual parts, Solid Edge CAD software will be used in parallel with ADAMS View, a dynamic multi body simulation tool used for simulating dynamic behavior. Simplified static structural FEA in Ansys Workbench is performed on critical components in parallel with design progress to assure the structural integrity of the parts.

3 FRAME OF REFERENCE

The frame of reference presents the initial constraints and design considerations of the vehicle as well as the benchmarking studies and the component search.

3.1 Preliminary design and vehicle architecture

The general dimensions of Newt, such as overall height, wheelbase, and ride height were established prior to the thesis using a mock-up model. The dimensions are implemented in the Rhino model, see Figure 3.1.

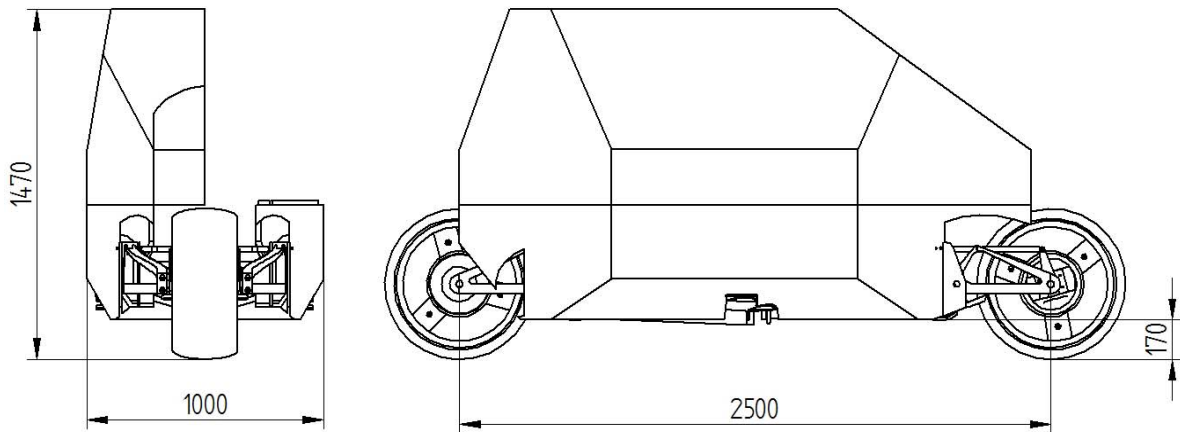


Figure 3.1. The overall dimensions of Newt represented in the Rhino model, dimensions are in *mm*. The left half of the vehicle cockpit has been removed.

Besides the overall dimensions this model is an outline for vehicle architecture and subsystem positioning, see Figure 3.2. The only major part left out is the gyroscopic balancing device, which according to Ivan Stenius will be placed in the rear of the cockpit as low as possible and probably underneath a possible passenger seat.

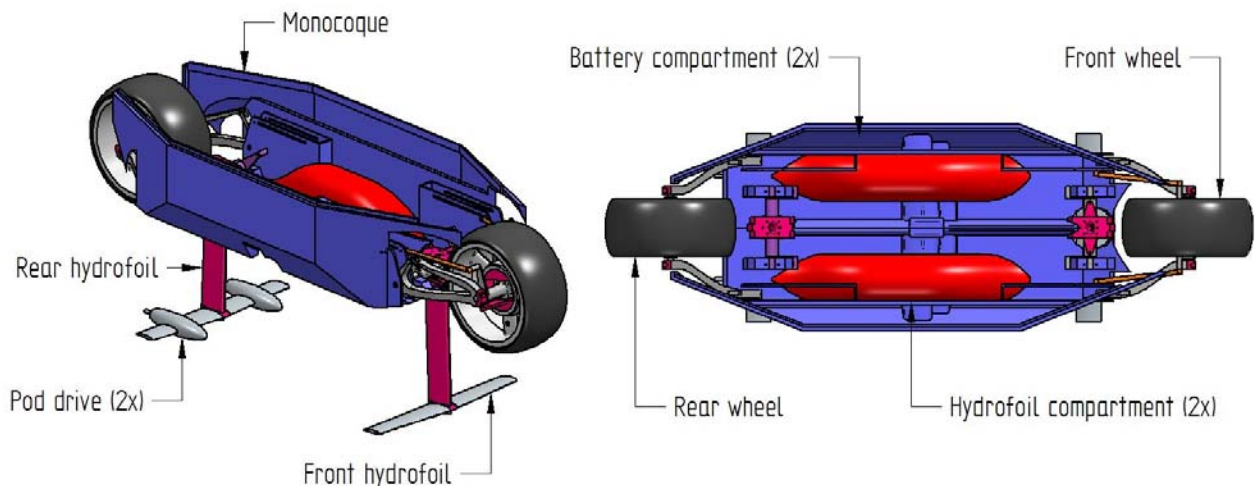


Figure 3.2. The general vehicle architecture established in the Rhino model.

A requirement specified by Ivan Stenius concerning the front unsprung assembly is that a hub motor shall be mounted to the front wheel. The front motor will provide tractive power when ascending from displacement mode into land mode presumably using an inclined water launch

ramp. While approaching the ramp only the front wheel will be in contact with the ground as the rear remains in displacement mode. In this phase the front motor will alone pull the vehicle out of the water up the inclined road until the rear wheel reaches ground contact.

Preliminary design choices were made together with Mikael Nybacka and Ivan Stenius determining the type of tires and rims for the vehicle as well as the total wheel travel for the suspension. The chosen tires are the motorcycle tires called Michelin Pilot Road 3 in dimension 170/60 ZR 17 with a suitable split rim. Total wheel travel is set to ± 50 mm.

3.2 Balance of two-wheeled vehicle

3.2.1 Straight line balancing

Balancing a two-wheeled vehicle is more complicated when traveling in low speed compared to high speed. In a motorcycle or bicycle the balance at low speed is mainly achieved by the riders ability to shift the centre of gravity. This is done by a combination of handlebar movement and small sideways translations of the rider (Foale, 1997). For Newt this low speed balancing is handled by the active gyroscopes. At higher speeds the straight line balancing has three central components, inertia, gyroscopic precession and restoring torque (Rothhämel, 2014).

3.2.1.1 Inertia balancing

The principle of *inertia* balancing is displayed in Figure 3.3. As the motorcycle is subjected to a disturbance causing a lateral velocity component dV , the vehicle wants to change trajectory according to angle α . At higher speeds the influence of dV is considerably less and angle α decreases thus reducing the sensitivity to disturbances (Rothhämel, 2014).

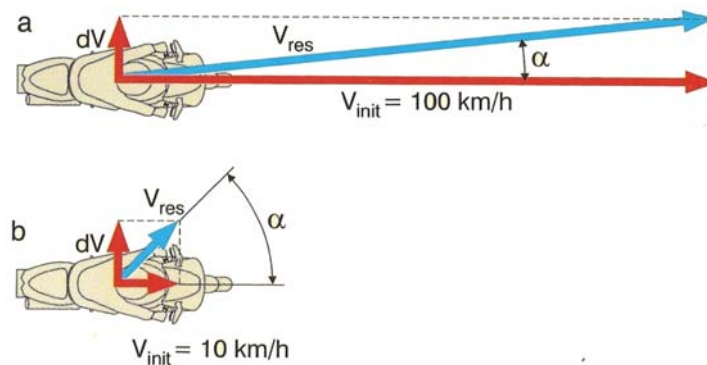


Figure 3.3. Balance, **a** has higher inertia and is less influenced by disturbances compared to **b**, (Rothhämel, 2014).

3.2.1.2 Gyroscopic precession

Gyroscopic precession takes place due to the angular momentum of the rotating front wheel, see Figure 3.4. The gyroscopic effect of the wheels balance the driver both when cornering and when traveling in a straight line. If the motorcycle starts to lean while going straight the gyroscopic effects on the front wheel causes the steering to deflect and sets the bike into a curved trajectory. This curvilinear translation generates a centrifugal force that counteracts the lean and bring the bike back to a vertical position (Foale, 1997-B).

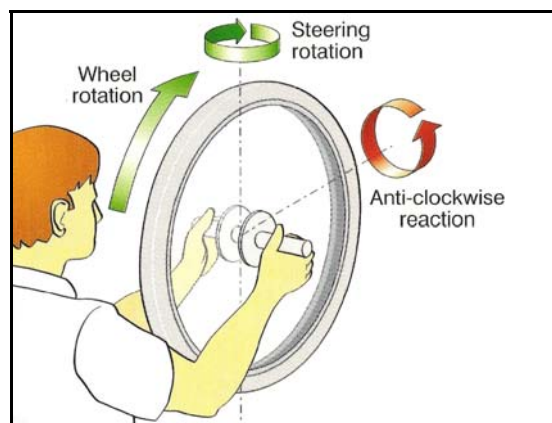


Figure 3.4. Gyroscopic effects of a steered rotating wheel (Rothhämel, 2014).

3.2.1.3 Restoring torque

The design of a motorcycle front suspension most often feature an inclined steering axis. The steering inclination, or rake angle, is defined as the angle from the vertical line going from the ground contact point and through the center of the wheel to the steering axis see Figure 3.5. The rake angle, the diameter of the wheel and, for some designs, the offset determines the parameter called *trail*. Trail is the distance from the steering axis virtual point of contact with the ground and the front wheel's physical contact point. Trail is defined positive as it is presented in Figure 3.5 when the wheel contact point lies behind the steering axis point (Rothhämel, 2014).

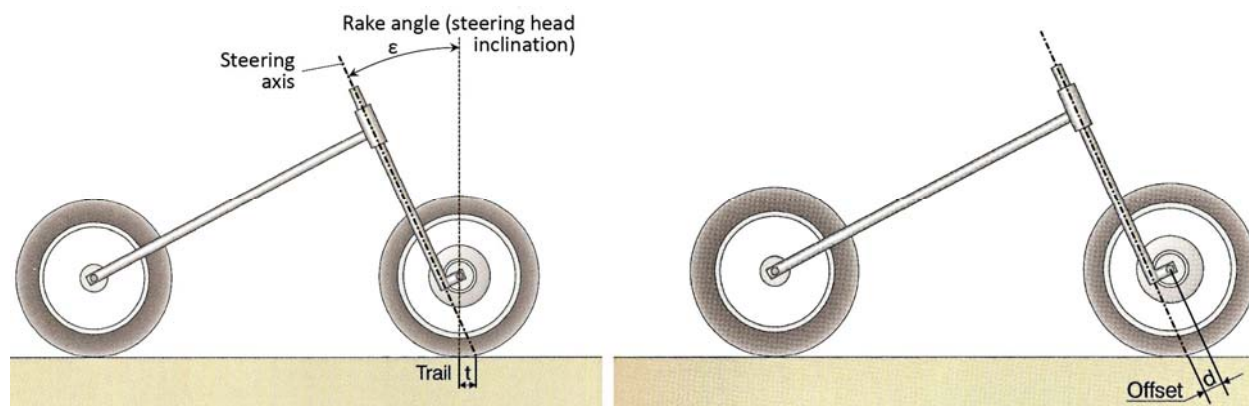


Figure 3.5. Definition of rake angle and trail (left), some suspension designs feature an offset (right) (Rothhämel, 2014).

Restoring torque is the balancing component that maintain the handlebars in a straight line position, it is generated due to trail. The presence of lateral forces generated by steering the front wheel and the lever arm due to trail will give rise to a self-aligning torque on the wheel working to bring it back to a straight ahead position (Foale, 1997-B), see Figure 3.6.

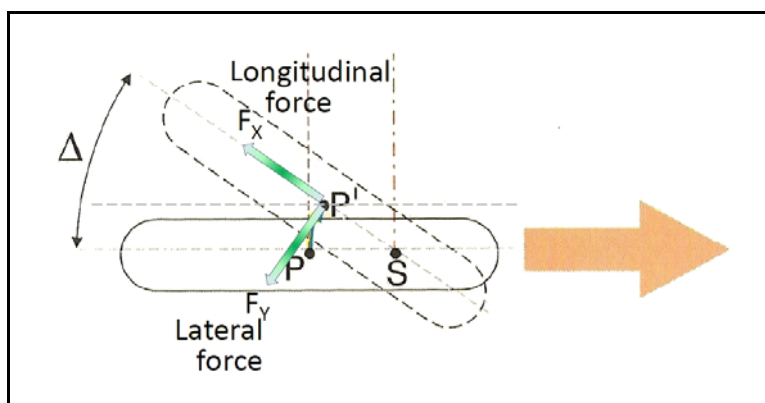


Figure 3.6. The turning of the front wheel causes lateral forces in the contact point P' which, due to trail generates a restoring torque at the steering axis S , (Rothhämel, 2014).

Trail is thus an important design feature as it maintains the straight line stability by counteracting steering displacements.

3.2.2 Two-wheeled oscillating modes

Because of the general geometry that two-wheeled vehicles share they are prone to three vibration modes when traveling in straight motion: *capsize*, *weave* and *wobble*.

The capsize mode indicates a roll and lateral displacement up to a point where the vehicle tips over. This is a non-vibrating mode and usually easily controlled by the rider and counteracted by balancing effects discussed above (Cossalter, et al., 2014).

In weave mode the entire two-wheeled vehicle is oscillating in a slalom trajectory meaning that the direction of front and rear wheel are opposite of each other. The frequency of the weave increases with speed while damping is decreasing, making it an alarming event for the rider (Cossalter, et al., 2014).

Wobble mode is an oscillation mode that may take place at higher speeds. The wobble is mainly due to structural compliance in the steering assembly, road irregularities or wheel imbalance (Cossalter, et al., 2014). When entering the wobbling mode the front steering assembly starts oscillating around the steering axis. The degree of oscillation that is exited can vary from a small shaking in the handlebars to completely uncontrolled oscillation. Unless a steering damper is fitted this event may resonate out of control which generally results in a crash (Foale, 2002).

3.3 Benchmarking - suspension

Among the commonly accepted motorcycle front suspensions there are three general types that differs to the extent that they are considered as fundamentally different from each other. The three types are *telescopic forks*, *double link* and *hub centre steering* (Foale, 2002).

3.3.1 Telescopic forks

A common type is the telescopic forks with integrated springs and shock absorbers. The issues with this design are the outcome when the vehicle is introduced to lateral and braking loads. The forces are acting out of plane with respect to the telescopic motion and give rise to a torque around the headstock. As a result the generated bending moments in the forks may cause lateral deflection or diving behavior, see Figure 3.7. The lever arm also amplifies the strain fed into the motorcycle headstock and chassis thus increasing the required strength of these components. The compliance in the lateral fork deflection is an excitation source of the wobble mode and therefore considered as one of the main drawbacks of such a suspension (Foale, 2002).

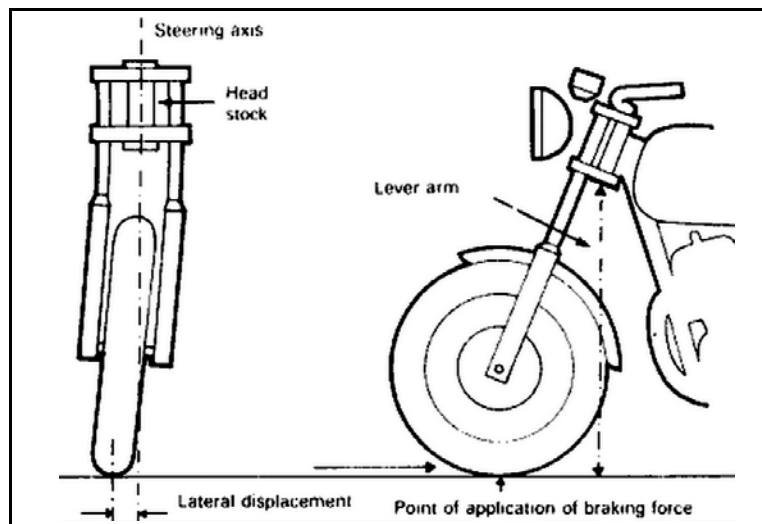


Figure 3.7. Some of the telescopic fork downsides are lateral deflection, prone to nosedive and amplified reaction loads in the headstock/chassis (Foale, 2002).

3.3.2 Double link (Elf, Foale/Parker and Hossack/Fior/Foale)

Three designs fall under the double link category, they all feature two swing arms that connects to an upright. Relative each other they differ mainly in the placement of the swing arms see Figure 3.8.

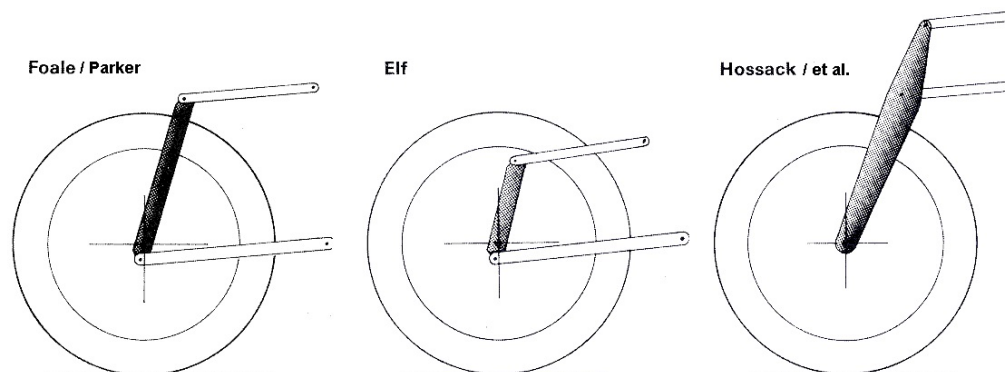


Figure 3.8. The basic principle of the different versions of the double link suspension (Foale, 2002).

Both swing arms of the Elf version and the lower swing arm in the Foale/Parker has a single side connection to the front wheel upright as illustrated by Figure 3.9. By introducing this geometry the swing arms need to cope with asymmetric loading conditions affecting the size and weight.

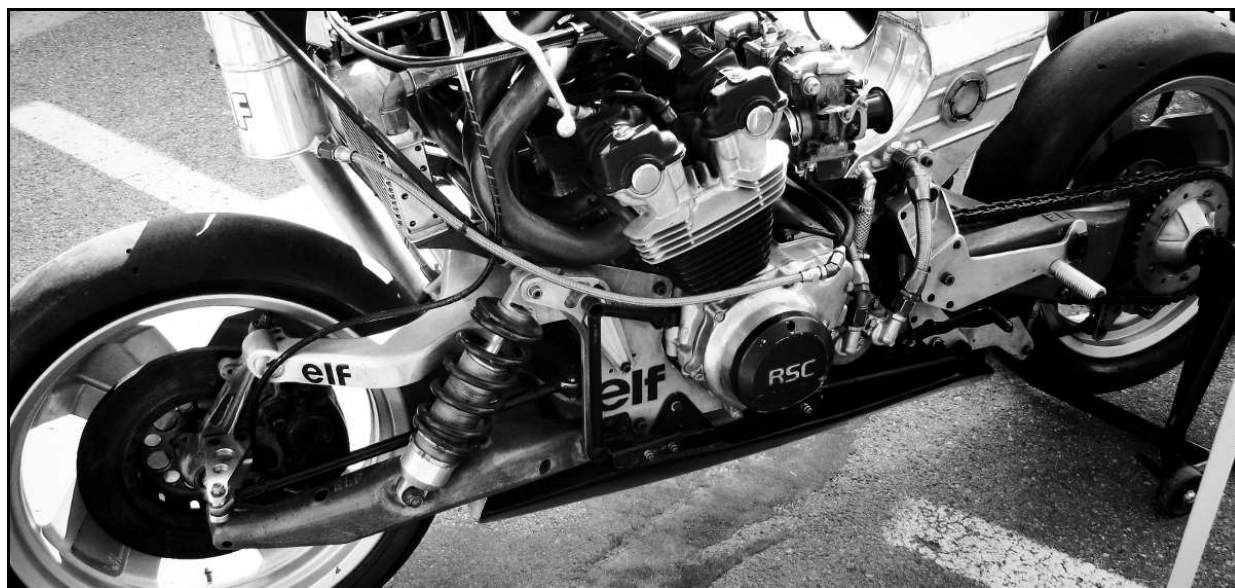


Figure 3.9. The Honda Elf motorcycle with double link suspension in the front, the swing arms are only attached to the upright on one side (Bikeblolocks, 2011).

The Foale/Parker design addresses the issue of asymmetric loading for the shock absorbing swing arm by utilizing a triangulated wishbone above the wheel which carries the shock absorber, see Figure 3.10. To accommodate these suspension arms the upright is elongated and as a consequence heavier and most likely less stiff (Foale, 2002).

Adopted, tweaked and renamed by BMW as the Duolever, the Hossack/Fior/Foale suspension design completely replaces the swing arms with triangulated wishbones (Foale, 2002). The upright takes the form of two stiff forks on each side joined at the top of the wheel while the shock absorber is mounted on the lower wishbone, see Figure 3.10. BMW also uses a special trapezoidal shear joint to decouple the steering from the dampening loads (BMW-Motorrad, 2004).



Figure 3.10. Foale/Parker front suspension design to the left with a single sided lower swing arm and extended upright connected to a triangulated upper wishbone taking normal loads (Foale, 2002). Duolever or Hossack et al. design to the right (Rider Magazine, 2005).

3.3.3 Hub centre steering

3.3.3.1 Carl Neracher and John Difazio

Already in 1919, Carl Neracher patented a hub steering invention at the United States patent office. His design established the general outline of such a mechanism with a steering axis pin fixed to an all through axle that is carried by suspended swing arms see Figure 3.11 (Neracher, 1925).

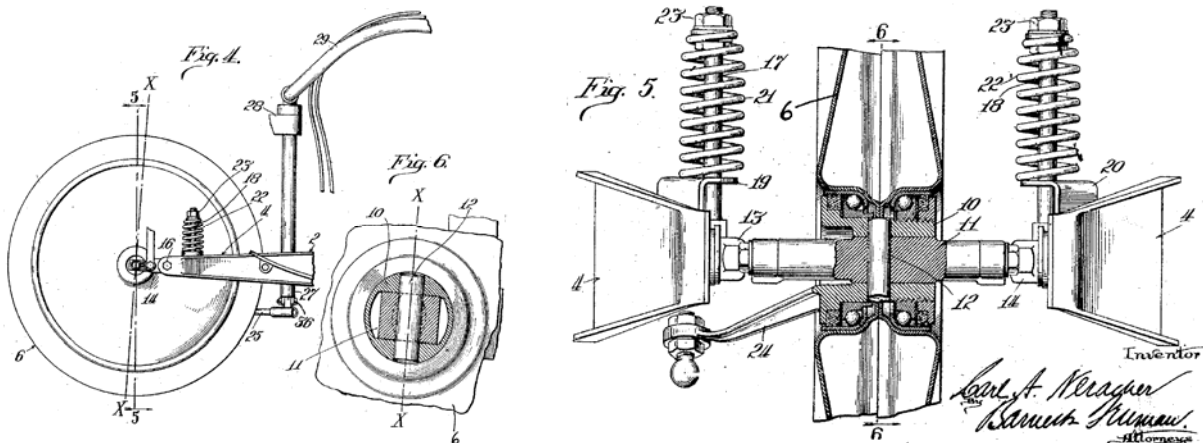


Figure 3.11. Carl Neracher's design as described in his patent application. To the left, the front wheel and a close up of the steering hub whilst to the right a detailed configuration of the steering mechanism (Neracher, 1925).

Filed in 1968 and granted in -72, another patent was registered to British inventor John Difazio. In the Difazio design some of Neracher's ideas resurfaced but the system had been significantly overturned to cope with the progress motorcycles had went through since the 20s e.g. the advances in power and speed (Difazio, 1968). The Difazio design is displayed in Figure 3.12.

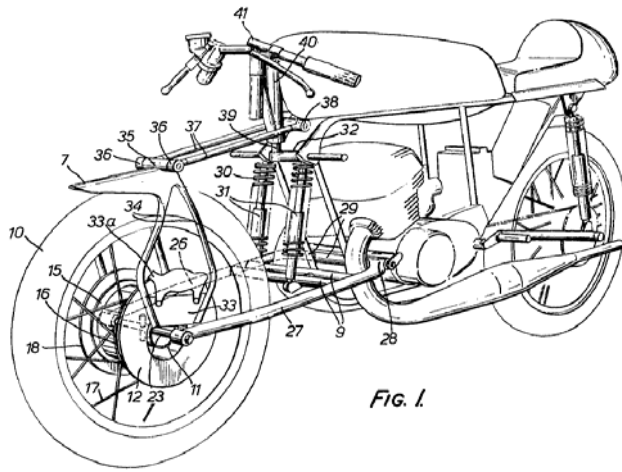


FIG. 1

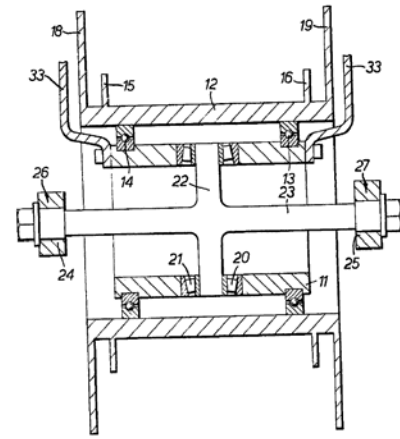


FIG. 2.

Figure 3.12. John Difazio's design as it is illustrated in his patent application (Difazio, 1968).

The design features an inner hub, seen to the right in Figure 3.12 with wheel bearings that connect it to an outer hub fixed to a spoke rim. The brake discs are an integral part of the outer rotating hub and the brake calipers are mounted on a bracket mounted to the inner hub and overhead steering members. In the hollow centre of the hub a transverse axle that is merged with the steering axis extends from side to side (Difazio, 1968).

3.3.3.2 *Bimota Tesi and ISR hub centre steering*

The most recent design modification to the Difazio solution is the principle of adding brake torque arms adopted by the Italian motorcycle manufacturer Bimota. Bimota's first hub centre model, the *Tesi ID* features two struts on each side connected to short torque arms fastened to the transverse axle see Figure 3.13. The struts guide the upright in suspension travel and dissipate brake forces into the chassis. The *Tesi 1D* used a handlebar actuated hydraulic steering which proved itself to be an issue for Bimota since it introduced compliance and as a result the steering feedback was deemed substandard (Foale, 2002).



Figure 3.13. The Bimota Tesi with hub centre steering and struts fixed to torque arms mounted to the transverse axis (SportbikeRider, 2012).

ISR Brakes, located in Stockholm Sweden, is a small company selling custom motorcycle components such as brake calipers, master cylinders and brake discs. ISR Brakes have developed a centre hub steering solution available for order, see Figure 3.14. It can be established that the ISR design has a lot of resemblance to the Bimota solution with a single swing and torque arms. Instead of hydraulic steering it utilizes a Bowden cable based pull system (Rising, 2010).



Figure 3.14. Stellan Egeland's custom BMW Harrier motorcycle front suspension with hub steering from ISR Brakes (Rising, 2010).

The main advantage when replacing telescopic forks with a centre hub swing arm suspension is the parting of loads. The braking, lateral and suspension forces are decoupled by eliminating the forks as the single load path into the chassis. When repositioning the physical steering axis to the centre of the wheel the lateral compliance in a headstock is eliminated. The lateral displacement for the wheel in relation to the steering axis is as a result only dependent on the wheel itself, wheel bearings and steering axis bearings. A drawback with this design is the severe loading on some components, for instance the transverse and steering axle which is stressed with severe braking loads (Foale, 2002).

3.4 Benchmarking - vehicles

Lit Motors is a recently founded company in San Francisco that is developing a gyroscopic balanced two-wheeled electric road vehicle called the C1, see Figure 3.15. When comparing Newt in its land mode to the C1 they are in principle the same type of vehicle though Newt has the added possibility of entering the water. Lit Motors vehicle utilizes a front swing arm and hub steering connected to a drive by wire system taking inputs from the steering wheel. The drive by wire system communicates with the gyros to initiate turns when steering (Lit Motors, 2014).



Figure 3.15. The Lit Motors first prototype with front swing arm, hub steering and rear wheel electric hub motor (Lit Motors, 2012)

Not explicitly stated by Lit Motors, but through ocular inspection in press releases it can be determined that their current prototype, depicted in Figure 3.15, uses the hub steering and swing arm solution provided by ISR Brakes.

3.5 Component search - hub motor

One of the most vital components of the front suspension is the electric hub motor. It is common that the motorcycle/bicycle hub motor is adapted for rear wheel usage or a telescopic fork mounting since they generally are fully enclosed with a stationary shaft extending from both sides. The wheel center or spokes attach to the motor housing while the rear swing arm or front fork connects to the shaft, see Figure 3.16.



Figure 3.16. A common type of motorcycle hub motor with spoke attachment (Electricbike, 2014).

If a hub centre steering and swing arm suspension is utilized the hub motor would require a special design to provide space for the hub and centre steering components. A suitable type of hollow centre ring motors are the *frameless brushless motor*.

3.5.1 Frameless brushless motors

ThingGap, AlliedMotion and Applimotion are United States based companies that provide frameless brushless motors. Allied Motion and Applimotion manufactures frameless brushless electric motors with an internal rotor and stationary coiled outer ring as stator (Allied Motion, 2015) and (Applimotion, Inc, 2015), see Figure 3.17.



Figure 3.17. The ring motor from Applimotion (Applimotion, Inc, 2015).

The ThinGap motor differs slightly as the outer ring act as the rotor and feature a proprietary ironless composite stator displayed in Figure 3.18.



Figure 3.18. ThinGap ring-motor with a stationary inner ring to the right, and a rotary outer ring to the left (ThinGap, 2014).

A final possibility is to manufacture a complete custom motor. BEVI is a Swedish company that specializes in retail and manufacturing of electric motors of different types. They can provide frameless brushless motors either from stock or develop a custom motor together with the customer (Wallmark, 2104).

4 DESIGN FOUNDATION

The design foundation contains the reflections from the frame of reference and establishes the basis for the front suspension design. The derivation of specific vehicle information vital to the continued development are also featured here.

4.1 Suspension type evaluation

4.1.1 Choice of principal design

Looking at the different suspension designs available there are only two options that are applicable to Newt due to geometrical constraints, the ISR/Bimota and the Honda Elf version. The remaining designs all feature struts, wishbones or dampeners on top of the wheel which may cause interference when retracting the wheels upon entering displacement mode. The position and required space of the driver and driver controls also confines placing components in this vicinity.

When comparing the two remaining alternatives, the ISR/Bimota design is the symmetric of the two. It is considered preferable to avoid asymmetric configurations and loading conditions in order to keep a high stiffness in the front suspension assembly without increasing the mass of the swing arm.

One property of the Elf design is the quick wheel changes made possible by a single sided swing, though this is not an imperative feature for Newt. The one argument that highly promotes the Elf design is the fact that a conventional hub motor can be used since the wheel interface will resemble that of a car. If a frameless hub motor is unable to meet the requirements and a conventional motor is needed the Elf design could be a viable back-up choice.

4.1.2 Choice of development

After choosing a *centre hub steering with a double sided swing arm* as the principal layout of the front suspension there are different ways of implementing such a system on the vehicle. The two main diverging choices is whether to purchase a hub steering system from ISR or instead develop an in-house design. In order to decide, some of the general requirements on the front suspension and steering assembly must be considered.

Besides the hub centre steering mechanism's generic purpose it must also, together with the wheel, fit and function together with a frameless motor. The motor also needs to be fully enclosed in order to waterproof the internal electronics. As the motor operates heat will be generated and dissipating this heat is crucial in order to provide proper operating conditions. If the convection cooling proves to be insufficient, conduction surfaces are needed.

The hub motor has a great influence on the design of surrounding components and would therefore require a redesign of the ISR product. With only one set of front suspension required for this proof-of-concept prototype, ordering a redesigned and custom product from ISR would most likely prolong vehicle development and increase cost compared to in-house development. The issue of parallel subsystem development discussed in section 1.1 also promotes an in-house design as it easily facilitates design iterations.

4.1.3 Chosen implementation

It has been shown that the most suitable principal design is the full out centre hub steering similar to that of ISR and Bimota. It has also been clarified that simply purchasing a bolt on hub

centre and swing arm solution is not possible. Designing a new steering and swing arm is therefore the chosen course of development for the front suspension system.

4.1.4 Overall conceptual idea

After choosing this suspension type it is recognized that the rough conceptual design in the Rhino model is a valid starting point for the front suspension development. The Rhino concept feature, like ISR and Bimota, swing arms, hub centre steering, torque arms, transverse axle and guide/torque struts, see Figure 4.1.

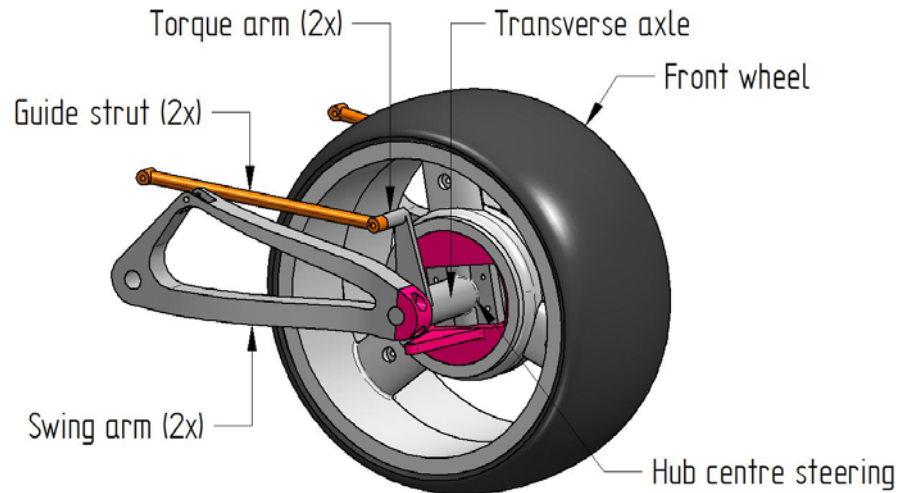


Figure 4.1. The general conceptual design of the front suspension.

Starting with the general concept in the Rhino model a *parametric detailed conceptual design* may be developed with focus on kinematics and vehicle dynamics.

4.2 Vehicle coordinate system

When in land mode, a global coordinate system is established for the analytical and computer models. This facilitates input and output between software as there is no need for coordinate transformations. A right hand Cartesian coordinate system is chosen with origin at the front tire contact patch, the direction of the coordinate system is defined in Figure 4.2.

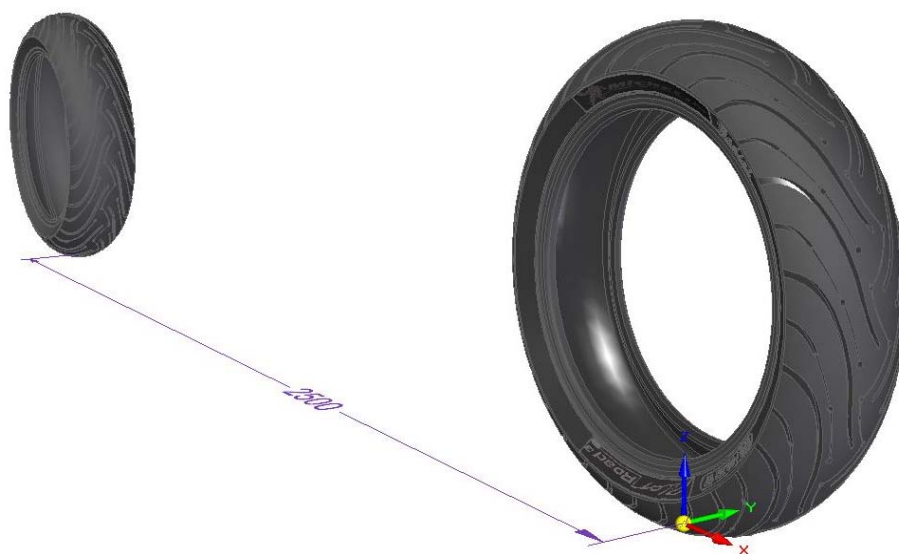


Figure 4.2. The global coordinate system for all models of the vehicle with origin at the front tire contact patch.

4.3 Simple CAD model

4.3.1 CoG position

When deriving the simulation models used for the vehicle's development the initial data for the position of the centre of gravity (CoG) is required. The main components and lengthwise vehicle symmetry is identified in the Rhino model. A symmetrical vehicle about the x-axis means that the CoG y-coordinate coincides with the vehicle centerline, thus equal to zero. The CoG x- and z-coordinate does not equal zero and must somehow be approximated.

When creating a CAD assembly with known mass properties for the inherent parts, the software calculates the position of the CoG for that assembly. By modeling the main contributions to the vehicle's mass and assembling them at estimated locations, the coordinates for Newt's CoG will be obtained.

The main components of the Rhino model are simplified, modeled and assembled in a simple CAD model displayed in Figure 4.3 with the cockpit hidden in order to present the internal components.

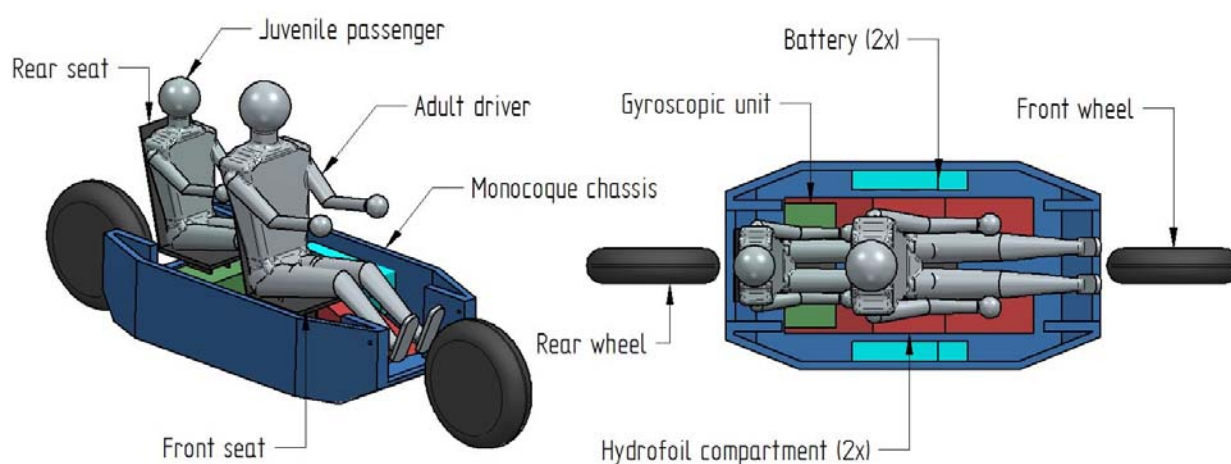


Figure 4.3. The simplified CoG assembly model, the vehicle's roof is removed to better illustrate underlying components. The pod drives together with the hydrofoils are retracted and represented by the hydrofoil compartment

To make proper estimations for the mass, each individual component is compared to a equivalent part from another vehicle that share characteristics such as weight, performance, payload and operating profile.

At the KTH Integrated Transport Research Lab (ITRL), a small four wheeled electric vehicle has been developed in conjunction with different course based student projects and faculty. The vehicle previously called *Smite* feature rear wheel drive with two direct drive 4 kW hub motors, a lithium based battery pack and a glass fiber reinforced plastic (GFRP) monocoque chassis sandwiched with divynycell core. Like in Newt, two people are able to ride in the vehicle tough with limited space for the passenger in the rear seat (Lais, et al., 2013). After several redesigns of *Smite* the vehicle is called *Electra*, Figure 4.4 shows a photo of *Electra*.



Figure 4.4. The small two-seated electric vehicle called Electra in the lab hall of ITRL.

To meet the design targets of integrating lightweight design and composites, Newt's chassis will most likely feature a composite sandwich monocoque structure. Assuming that the operating loads dissipated into the chassis of Newt are in the same order of magnitude as in the case of Electra their chassis mass would be approximately equivalent.






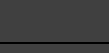
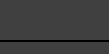
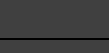

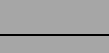
The weight of the battery for Newt is assumed to be slightly higher than for Electra since it will require an extra storage of energy to power the other operation modes and additionally increase the vehicles mileage.

In the simple CAD model the added weight of uniformly distributed parts such as electronics and wiring are added to the mass of the monocoque achieving an evenly distributed effect. The tub of the monocoque is expected to be the most load carrying part and therefore also the heavier. The roof section's function will mainly be to protect driver and passenger from roll over thus obtaining a lower weight.

The mass and size of the driver is estimated based on an assumed average weight and measurements of an 1.84 m tall adult male. The juvenile person representing the passenger is a scaled model of the adult at a weight specified in Table 4.1.

Table 4.1 lists the parts displayed in Figure 4.3 with their assigned mass and corresponding equivalent components from Electra (Lais, et al., 2013). The assigned mass in the CAD software is evenly distributed in each component. The size of the modeled components are approximately equivalent to their representative counterpart in the Rhino model. The properties of the parts unique to Newt, the gyroscopic unit and the hydrofoils have been estimated based on previously conducted work (Sundberg, 2014).

Table 4.1. Mass assignment for the components in the simplified CoG model. The retracted pod drives and hydrofoils are represented by the hydrofoil compartment.

Component	Color	Quantity	Mass, [kg]	Equivalent component	Equivalent mass, [kg]
Battery		2	2×17.5	Electra battery	22
Gyro unit		1	25	-	-
Hydrofoil comp.		2	2×10	-	-
Monocoque, tub		1	40	Electra monocoque	35
Monocoque, roof	-	1	10	-	-
Seat, Front		1	7.5	Electra front seat	10
Seat, Rear		1	4	Electra rear seat	5
Wheel, Front		1	20	Electra drive wheel	22.5
Wheel, Rear		1	20	Electra drive wheel	22.5
Adult Driver		1	80	-	-
Passenger		1	55	-	-
Aggregated mass, with wheels			316.5		
Aggregated mass, without wheels			276.5		

The CAD software calculated coordinates for the centre of gravity are presented in Table 4.2.

Table 4.2. Resulting CoG coordinates with and without wheels.

Coordinate, [mm]	x	y	z
With wheels	-1409	0	560
Without wheels	-1432	0	595

The CoG is also displayed in the assembly, see Figure 4.5.

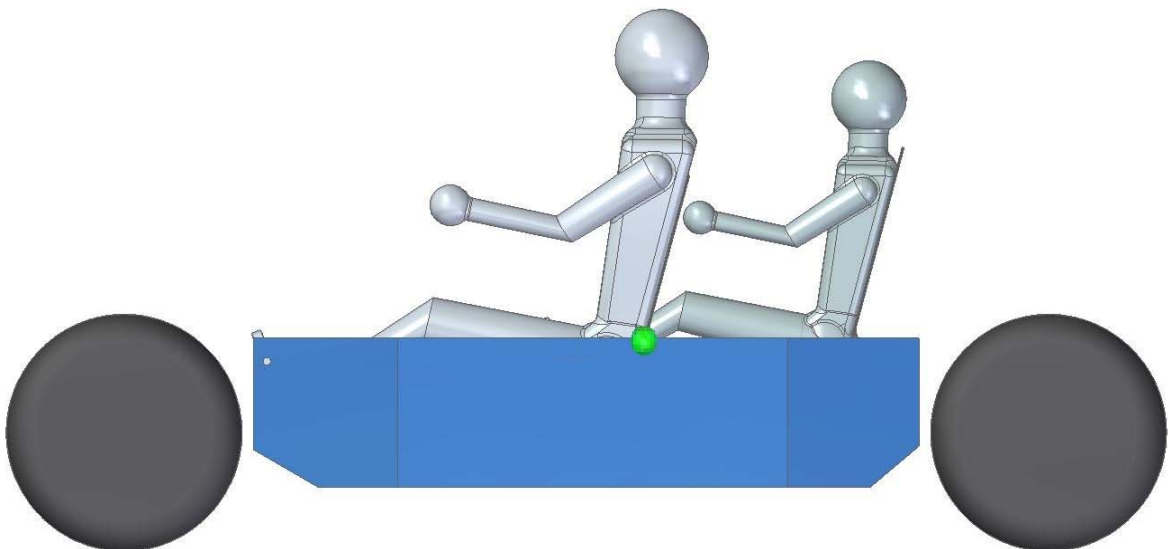


Figure 4.5. The simple CAD model viewed from the side with the CoG displayed as a green sphere.

4.3.2 Frontal area estimation

Besides the position of the CoG, the frontal area is also required in the simulation models for the vehicle, it is used when calculating aerodynamic drag forces. With the Rhino cockpit as a reference, a representative body of the vehicle is created in the CoG model. The frontal area is 1.17 m², also found in Table 5.1. It is measured in the yz-plane by projecting the geometry onto the plane, see Figure 4.6.

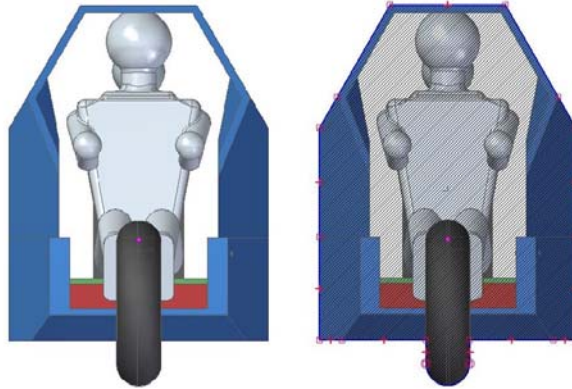


Figure 4.6. Measuring the frontal area of Newt utilizing the simple CAD model.

4.3.3 Tire rolling radius

When the tires are subjected to the weight of the vehicle the contact patch is formed and the effective tire radius decreases, this radius is called the rolling radius. At standstill, the percentage of the total weight going into a wheel is given by the ratio of the horizontal position of the CoG and the wheelbase. The percentage of total load at the front wheel is calculated with

$$\% \text{ weight in the front} = \frac{2500 - 1409}{2500} \approx 44\% \quad (4.1)$$

With m representing the total weight of the vehicle may the equivalent front wheel mass be calculated with

$$0.44m = 139 \text{ kg}. \quad (4.2)$$

The front tire rolling radius is then derived by placing a wheel in ADAMS with tire properties of the chosen Michelin tire and assigning it the equivalent mass. The influence of gravity is achieved by running an equilibrium simulation and the rolling radius is acquired from the default wheel output parameters seen in the graph in Figure 4.7.

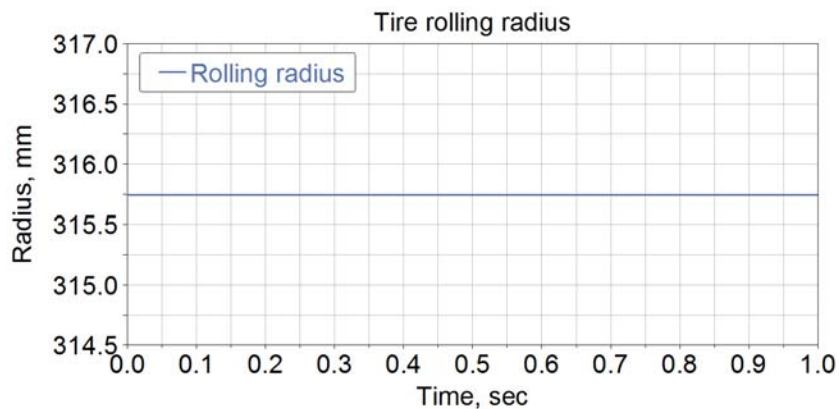


Figure 4.7. A single wheel with equivalent front wheel weight is simulated in ADAMS when deriving the tire rolling radius.

5 ANALYTICAL MODELS

This chapter presents the theory behind and the derivation of a number of analytical models used in the front suspension design development.

The analytical models covered in this section are used to derive both performance specifications for the vehicle and also design parameters for the front suspension. The outcome of the analytical models are very much dependent on the CoG input. When the iterative development of the vehicle progresses the CoG position will change and be recalculated with more detailed CAD models. Because of this two-way iterative dependence of the development models it is essential that they are parameterized to facilitate revisions.

5.1 Rigid vehicle model

Based on desired vehicle performance in terms of speed, deceleration and acceleration can the primary specifications for Newt, e.g. power, tractive and braking torque, be established with a general two dimensional rigid vehicle model. This model can be used to simulate sequences of acceleration, deceleration, constant velocity and standstill equilibrium. Being a two dimensional model there are no considerations of out of plane events.

A rigid model neglects the rotational inertial effects and components elasticity, meaning that their influence on energy consumption are considered so small it can be ignored (Cossalter, et al., 2004). This model is later complemented with an analysis for the ideal brake ratio giving the ratio of braking torque for the front and rear.

5.1.1 Vehicle equilibrium

In order for the 2D vehicle equations to be valid for a general case the vehicle is placed on an inclined road with all acting forces plotted, see Figure 5.1.

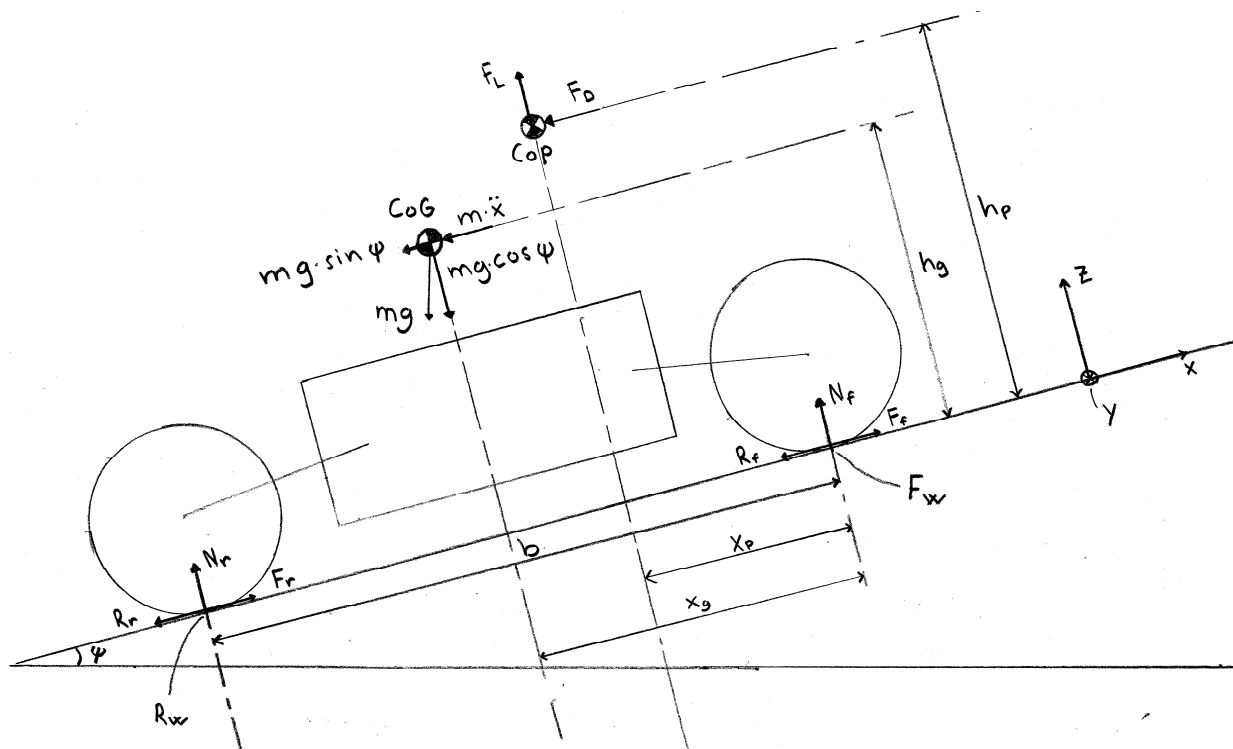


Figure 5.1. The 2D vehicle equilibrium free body diagram which is the basis for the rigid vehicle model.

The defined forces and general vehicle parameters are presented in Table 5.1.

Table 5.1. Acting forces and general vehicle parameters.

Name	Designation	Value
Centre of gravity	CoG	-
Centre of pressure	CoP	-
Aerodynamic drag force	F_D	Equation
Aerodynamic lift force	F_L	Equation
Tractive/braking force	F_f and F_r	Equation
Wheel normal load	N_f and N_r	Equation
Rolling resistance force	R_f and R_r	Equation
Inertial force	$m\ddot{x}$	Equation
Gravitational force	mg , $mg\cos(\psi)$ and $mg\sin(\psi)$	Equation
Gravitational constant	g	9.81 m/s ²
Vehicle mass	m	316.5 kg
Frontal area	A	1.169 m ²
Tire rolling resistance coefficient	C_R	0.02
Tire unloaded radius	r	318 mm
Tire rolling radius	r_t	315.7 mm
Horizontal distance to CoG	x_g	1409 mm
Horizontal distance to CoP	x_p	Equation
Vertical distance to CoG	h_g	560 mm
Vertical distance to CoP	h_p	Equation
Vehicle speed	v	Case dependent
Wheelbase	b	2500 mm
Road inclination angle	ψ	15°
Coefficient of drag	C_D	0.26
Coefficient of lift	C_L	-
Air density	ρ	1.275 kg/m ³

The known forces in this model are the aerodynamic loads for drag and lift, F_D and F_L , defined as

$$F_D = \frac{1}{2} \rho v^2 A C_D \quad (5.1)$$

$$F_L = \frac{1}{2} \rho v^2 A C_L \quad (5.2)$$

where ρ is the density of the ambient air, v is the relative velocity of the vehicle and the flowing air (if there is no wind v equals the speed of the vehicle), A is the frontal area of the vehicle and C_D/C_L is the coefficient of drag/lift.

With the rolling resistance coefficient C_R known and equal for both tires, the rolling resistance forces R_r and R_f are

$$R_r = C_R N_r \quad (5.3)$$

$$R_f = C_R N_f \quad (5.4)$$

Applying Newtonian mechanics the unknown normal forces N_r and N_f and tractive/braking forces F_r and F_f are derived. Moment equilibrium gives the normal forces,

$$\sum_{\odot_+} M_{F_w} = 0: N_r b - h_g mg \sin \psi - x_g mg \cos \psi - m\ddot{x} h_g - F_D h_p + F_L x_p = 0 \quad (5.5)$$

solving for N_r

$$N_r = \frac{mg(h_g \sin \psi + x_g \cos \psi) + F_D h_p - F_L x_p}{b} + m\ddot{x} \frac{h_g}{b} \quad (5.6)$$

Similarly N_f is obtained with

$$\sum_{\odot_+} M_{R_w} = 0: -N_f b - F_D h_p - F_L (b - x_p) - m\ddot{x} h_g + (b - x_g) mg \cos \psi - h_g mg \sin \psi = 0 \quad (5.7)$$

and

$$N_f = \frac{mg((b - x_g) \cos \psi - h_g \sin \psi) - F_D h_p - F_L (b - x_p)}{b} - m\ddot{x} \frac{h_g}{b} \quad (5.8)$$

Force equilibrium in x-direction gives the tractive/braking forces F_r and F_f ,

$$\sum F_x = 0: -R_r + F_r - mg \sin \psi - m\ddot{x} - F_D - R_f + F_f = 0 \quad (5.9)$$

With equation (5.3) and (5.4), equation (5.9) is elaborated into

$$F_{tot} = F_r + F_f = C_R (N_r + N_f) + mg \sin \psi + m\ddot{x} + F_D \quad (5.10)$$

where F_{tot} is the total tractive/braking force. If this force is coupled with the tire rolling radius r_t , the total tractive/braking torque T_{tot} , is acquired

$$T_{tot} = F_{tot} r_t \quad (5.11)$$

5.1.2 Dynamic load transfer

The second term in equation (5.6) and (5.8) is called the dynamic load transfer ΔN ,

$$\Delta N = m\ddot{x} \frac{h_g}{b} \quad (5.12)$$

Load transfer originates from the inertial effects taking place during acceleration or deceleration sequences and causes the front and rear wheel to experience a varying vertical load (Cossalter, et al., 2004).

The physical effect of load transfer is clearly exemplified by an decelerating motorcycle. During deceleration load is transferred to the front and the motorcycle normally nose-dive due to deflection of the suspension springs when subjected to the additional dynamic load. (Foale, 1997-A). While pitching forward and lowering the nose is called dive, the opposite is termed squat, when the nose rise during acceleration and the vehicle pitches backwards.

To provide a comfortable driving experience in Newt such deceleration diving behavior should be restricted. As load transfer occurs through inertial effects it is unavoidable and an anti-dive system must be implemented to counteract the tendency for pitching.

5.1.3 Initial assumptions and input data

The aerodynamic lift force is assigned a zero value since the contributions of lift are assumed so small they can be neglected. The contribution of drag may however be quite substantial when the vehicle is traveling at highway speeds. This is because the force is dependent of the squared velocity and the coefficient of drag, C_D , is sufficiently large that the force cannot be neglected. Coefficient of drag have been estimated by the project commissioner Ivan Stenius.

The aerodynamic forces are acting at the centre of pressure (CoP) as indicated by Figure 5.1. The location of the centre of pressure will be dependent on the vehicles aerodynamic properties. For the analytical models the CoP is assumed to coincide with the CoG.

The tire rolling resistance coefficient, C_R , is a tire dependent property. The coefficient used in the equations are derived from the Michelin Pilot Road 3 tires chosen in the preliminary design stage.

5.1.4 Input and output

Four different maneuvers are simulated with the rigid vehicle model, *standstill*, *steady state at highway speed*, *steady state at inclined ramp* and *constant acceleration*. The input data for each case is presented in Table 5.2.

A fifth maneuver, when the vehicle has a *constant deceleration from highway speed at the verge of skidding* is also simulated, however it requires the rigid vehicle model to be coupled with the ideal braking model derived in section 5.4. The ideal braking model is utilized to establish a rate of deceleration and the braking torque ratio between the front and rear wheel.

Table 5.2. Input data for the different simulations in the rigid vehicle model.

Case		Speed, [m/s]	Acceleration, [m/s ²]	Incline, [°]
Standstill	0 kph	0	0	0
Steady speed	100 kph	27.8	0	0
Inclined ramp	5 kph	1.4	0	15
Constant acc.	0-100 kph in 5 s	0 - 27.8	5.56	0

The rigid vehicle model uses the input data and the general vehicle parameters to calculate the normal load in the tires, the tractive torques acting on the wheels and the required power, presented in Table 5.3.

Table 5.3. Output from the rigid vehicle model

Case		Normal load, [N]		Wheel torque, [Nm]		Power, [kW]	
		Front	Rear	Front	Rear	Front	Rear
Standstill	0 kph	1355.0	1749.9	-	-	-	-
Steady speed	100 kph	1321.5	1783.4	26.7	40.1	2.4	3.5
Inclined ramp	5 kph	1128.7	1870.4	272.8	-	1.2	-
Constant acc.	0 - 100 kph in 5 s	927.6	2177.3	248.8	373.2	21.9	32.8

The acceleration sequence is simplified in the sense that only the maximum power is presented, the power required to travel at a speed of 100 kph and maintain the acceleration.

The resulting dimensioning values of the vehicle's motors are the tractive torque and power based on the *acceleration* and *inclined ramp* maneuvers. Looking to the acceleration maneuver, Newt is supposed to reach 100 kph from standstill in 5 seconds. This acceleration is similar to that of a high performance sports vehicle. If such a severe acceleration is unnecessary for Newt the torque requirement may be reduced.

The required front motor torque when going up the *inclined ramp* is also quite extensive. This maneuver have been extremely simplified in the rigid vehicle model by assuming that the entire weight of the vehicle is driven up the ramp. In a real life scenario much of Newt's weight would be displaced in water giving buoyancy thus reducing the effecting inclination angle. Some sort of support propulsion system would also be needed to propel the displaced vehicle the final distance to the ramp when the hydrofoils are retracted. This system will also keep the vehicle from bouncing away from the ramp when rocking in the water. The reduced inclination angle and the support propulsion system will assist when ascending the ramp thus reducing the required front motor torque.

In spite of these considerations the values displayed in Table 5.3 are the chosen performance characteristics for the conceptual design developed in this thesis. With the models the parameters are however easily updated when a suitable acceleration is chosen and the inclined ramp maneuver is more thoroughly analyzed.

5.2 Kinematic analysis model

The kinematic analysis model is used to simulate two dimensional wheel travel of the front suspension linkage. The model calculates the position and orientation of the links and corresponding joint coordinates in a local coordinate system. At standstill the vehicle is supposed to be at ride height meaning that the tire, springs and suspension has deflected until stationary equilibrium is reached. The neutral position in the kinematic analysis model is this ride height position why the coordinates for the suspension joints, also known as hardpoints (HP) calculated by the model are valid when the vehicle is at ride height.

5.2.1 Deriving geometry

Zooming in on the front wheel and defining a local coordinate system for the kinematic analysis makes the equations of motion less complicated. Figure 5.2 shows the front wheel suspension four bar linkage with local coordinate system, parameters and variables.

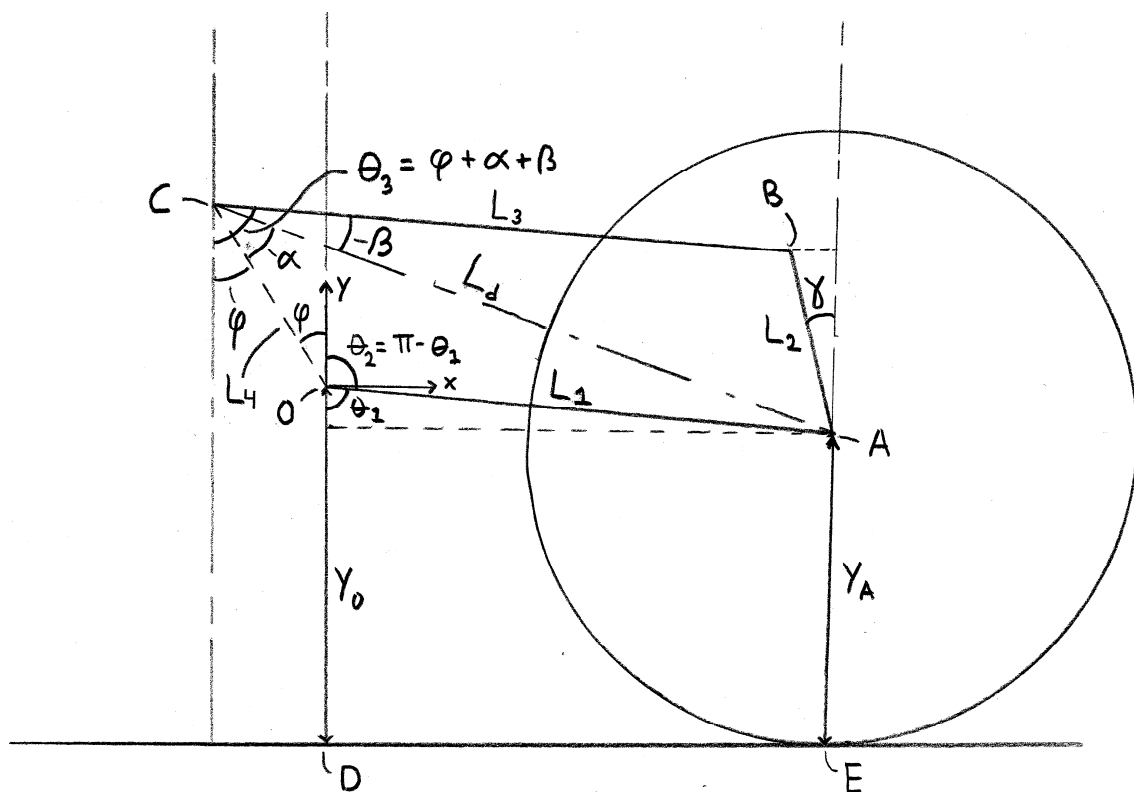


Figure 5.2. A general front suspension linkage modeled at ride height.

When considering the inner swing arm pivot point stationary as displayed in Figure 5.2, the ground is displaced vertically to simulate wheel displacement. The parameter y_0 is divided into a stationary component, y_{0s} (ride height) and the displacement vector Δy_0 ,

$$\Delta \mathbf{y}_0 = [-y_n \quad -y_{n-1} \quad \cdots \quad -y_1 \quad 0 \quad y_1 \quad \cdots \quad y_{n-1} \quad y_n] \quad (5.13)$$

where $y_n = 50 \text{ mm}$. Scalar annotation is used when deriving the equations of motion while the vectorized calculations are solved with Matlab which facilitates array mathematics.

The expression for the angle θ_1 is acquired with a geometric loop in y direction through $ODEA$

$$\begin{aligned}
y &: -y_0 + y_A + L_1 \cos \theta_1 = 0 \\
\Rightarrow \cos \theta_1 &= \frac{y_0 - y_A}{L_1}
\end{aligned} \tag{5.14}$$

The angles θ_2 and θ_3 are given by

$$\theta_2 = \pi - \theta_1 \tag{5.15}$$

and

$$\theta_3 = \varphi + \alpha + \beta \tag{5.16}$$

A combination of the cosine and sine rule together with the virtual diagonal link called L_d provides the expressions for α and β . L_d is calculated using the cosine rule in the triangle OAC

$$\begin{aligned}
L_d^2 &= L_4^2 + L_1^2 - 2L_4L_1 \cos(\theta_2 + \varphi) \\
\Rightarrow L_d &= \sqrt{L_4^2 + L_1^2 - 2L_4L_1 \cos(\theta_2 + \varphi)}
\end{aligned} \tag{5.17}$$

When L_d is known, the sine rule in the same triangle, OAC , gives a way to calculate α

$$\begin{aligned}
\frac{\sin \alpha}{L_1} &= \frac{\sin(\theta_2 + \varphi)}{L_d} \\
\Rightarrow \sin \alpha &= \frac{L_1}{L_d} \sin(\theta_2 + \varphi)
\end{aligned} \tag{5.18}$$

Calculating the angle α from equation (5.18) require using the arcsine function. Arcsine is limited to only handle angle outputs ranging from 90° to -90° ($\pi/2$ to $-\pi/2$) but when inspecting Figure 5.2 it is concluded that α may reach angles greater than this limit. With point O and C being fixed in the model α will always increase during positive wheel travel. Above the limit of 90° the arcsine function will instead give decreasing values and an error is introduced. Implementing a logical statement in the Matlab code that corrects the arcsine computation is needed to bypass the problem. The code checks if the angle starts to decrease when it actually should increase. If that happens the angular value is corrected with

$$\alpha_{correct} = \pi - \alpha_{wrong} \tag{5.19}$$

By applying the cosine rule once more, tough in the triangle ABC , yields the final expression for β

$$\begin{aligned}
L_2^2 &= L_3^2 + L_d^2 - 2L_3L_d \cos \beta \\
\Rightarrow \cos \beta &= \frac{L_3^2 + L_d^2 - L_2^2}{2L_3L_d}
\end{aligned} \tag{5.20}$$

The arccosine function handles output angles from 0° to 180° (0 to π). Since the angles θ_1 and β are confined in this span for the specified wheel displacement there is no need to correct the output of equation (5.14) and (5.20).

The equations above are sufficient to define the entire kinematic motion of the linkage system, though in order to derive the suspension HP the coordinates for the joints in the system need to be calculated. The x-coordinates are

$$A_x = L_1 \sin \theta_1 \tag{5.21}$$

$$C_x = -L_4 \sin \varphi \quad (5.22)$$

$$B_x = C_x + L_3 \sin \theta_3 \quad (5.23)$$

And the y-coordinates

$$A_y = -L_1 \cos \theta_1 \quad (5.24)$$

$$C_y = L_4 \cos \varphi \quad (5.25)$$

$$B_y = C_y - L_3 \cos \theta_3 \quad (5.26)$$

The coordinates for the inner swing arm joint positioned in local origin is naturally (0,0). These coordinates facilitates the derivation of the torque arm angle γ ,

$$\tan \gamma = \frac{A_x - B_x}{B_y - A_y} \quad (5.27)$$

Using the trigonometric tangent function means that angle direction information is preserved in the equation since the inverse of tangent, arctangent, covers negative angles. If instead cosine is used the direction information would be lost since the output of arccosine can only be a positive value.

5.2.2 Input, output and code validation

The parameters for the kinematic analysis are the lengths of the different links, the distance y_0 from the local origin to the ground and the angle φ . Initial guesses for the parameter values are assigned to be able to execute a wheel travel simulation and generate a temporary suspension linkage. The parameter values and the simulation constants are presented in Table 5.4.

Table 5.4. Input data for the kinematic analysis model.

Type	Name	Designation	Value	Unit
Constant	Wheel radius	y_A	0.3157	m
Parameter	Distance to local origin	y_0	0.318	m
Parameter	Swing arm length	L1	0.42	m
Parameter	Torque arm length	L2	0.15	m
Parameter	Torque strut length	L3	0.45	m
Parameter	Pivot points distance	L4	0.12	m
Parameter	Pivot points angle	φ	10	deg

Executing the wheel travel simulation with the temporary input data generates a result set used to validate the code and prepare it for the optimization routine. Among the output data, two central result graphs are extracted, the horizontal wheel displacement and the torque arm angle, see Figure 5.3. As the motion of the torque arms are stationary in relation to the steering axis the angular change is the same for both parts.

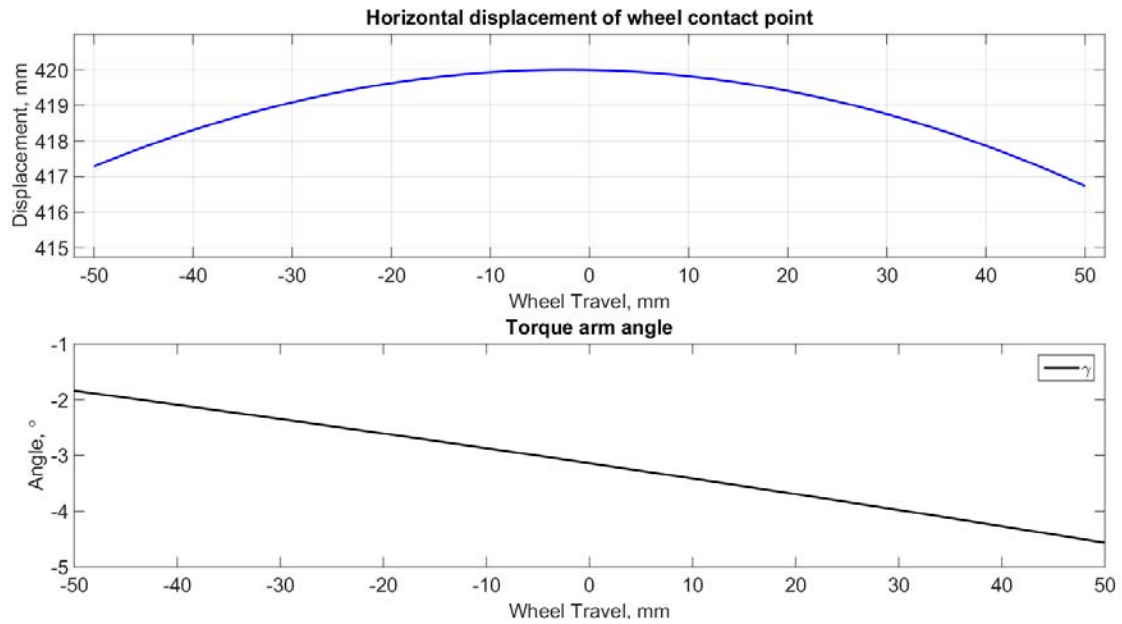


Figure 5.3. Graph output from the kinematic analysis, the horizontal wheel displacement (top) and the torque arm angle (bottom).

Possible simulation errors are identified by animating the wheel and suspension links during the entire wheel travel and inspecting the motion displayed by the plot. Figure 5.4 displays screen shots of the animation at four different time steps.

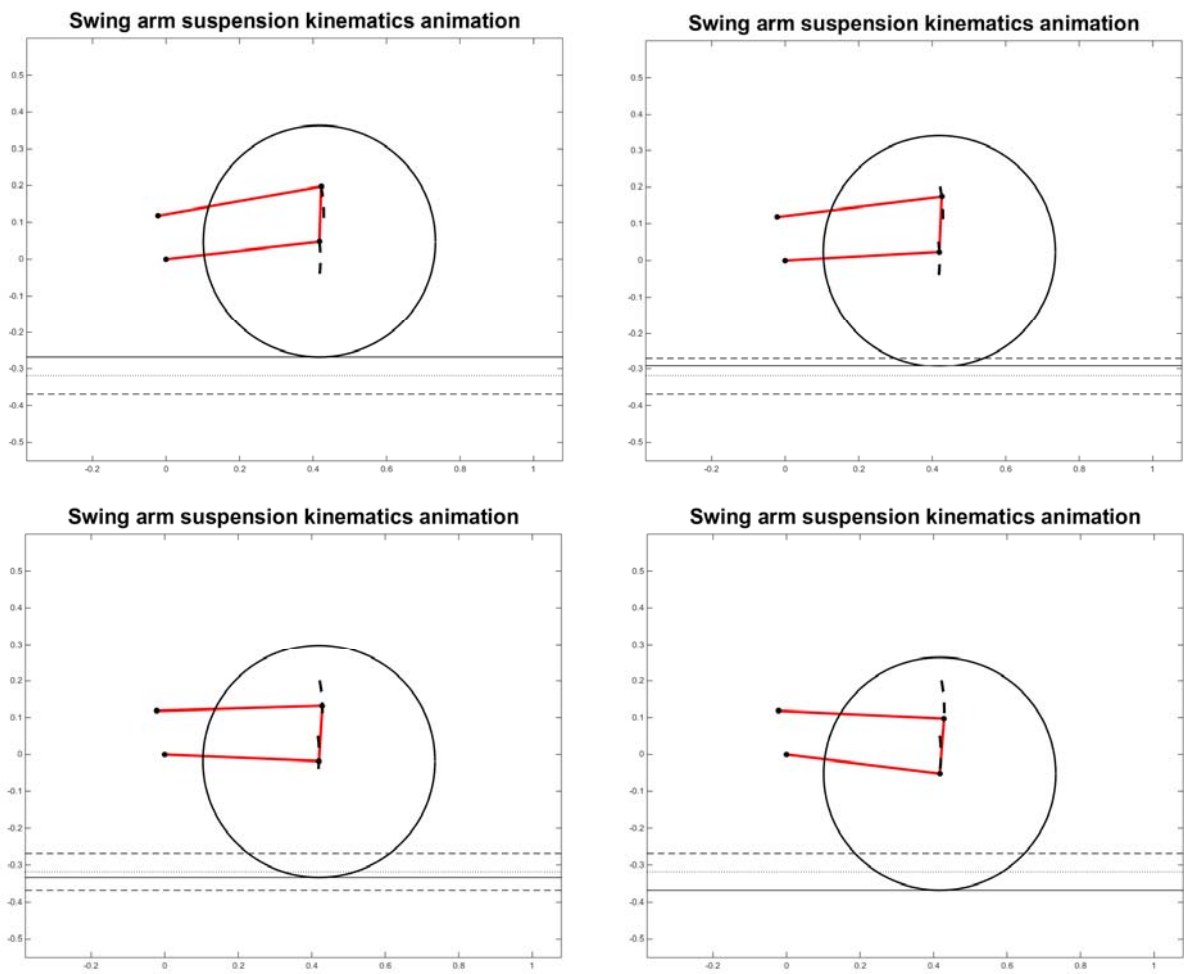


Figure 5.4. Four screen shots of the animation of the temporary front suspension linkage during wheel travel.

5.3 Anti-dive model

In the motorcycle industry different solutions have been developed to counteract dive, though mainly for telescopic suspensions. A link arm suspension can however be designed with a *natural anti-dive* (Foale, 1997-A). The fundamental property is that the hardpoints (HP) are designed in such a way that the link arms carry the additional dynamic load instead of the spring. When the dynamic load is rerouted in this way there is no compression of the spring, thus there is no dive or pitch. The presence of an anti-dive geometry does however not change the dynamic load increase at the tire contact patch (Milliken & Milliken, 1995).

The amount of anti-dive is quantified using an anti-dive ratio calculated with

$$ADR = BR_{front} \cdot \tan(\zeta_F) \cdot \left(\frac{b}{h_g}\right) \quad (5.28)$$

Where *ADR* and *BR* are the acronyms for *anti-dive ratio* and *brake ratio*, *b* is the wheelbase, *h_g* the height from ground to the CoG and the angle ζ_F defined as in Figure 5.5 (Milliken & Milliken, 1995).

At $ADR = 1$ (100% anti-dive), all dynamic load transfer passes through the suspension arms and zero dive would be achieved. Consequently, at 0% anti-dive all the dynamic load is routed through the spring with a result of excessive dive (Foale, 1997-A).

For an arbitrary suspension geometry the anti-dive ratio will not be constant throughout the range of wheel travel. This because the position of the instant center (IC), the virtual pivot point of the suspension linkage, is changing during jounce and rebound and with it the angle ζ_F also changes. To compute the anti-dive ratio the equations from the kinematic analysis are used in this additional anti-dive model where an expression for the angle ζ_F is derived.

Assuming that the contact patch of the front wheel is in vertical alignment with the wheel center the horizontal distance from the contact point to the position of IC may be called IC_x . In order to simplify the equations, the vertical distance, IC_y , only extend from the wheel center to IC, see Figure 5.5 for the anti-dive model geometry.

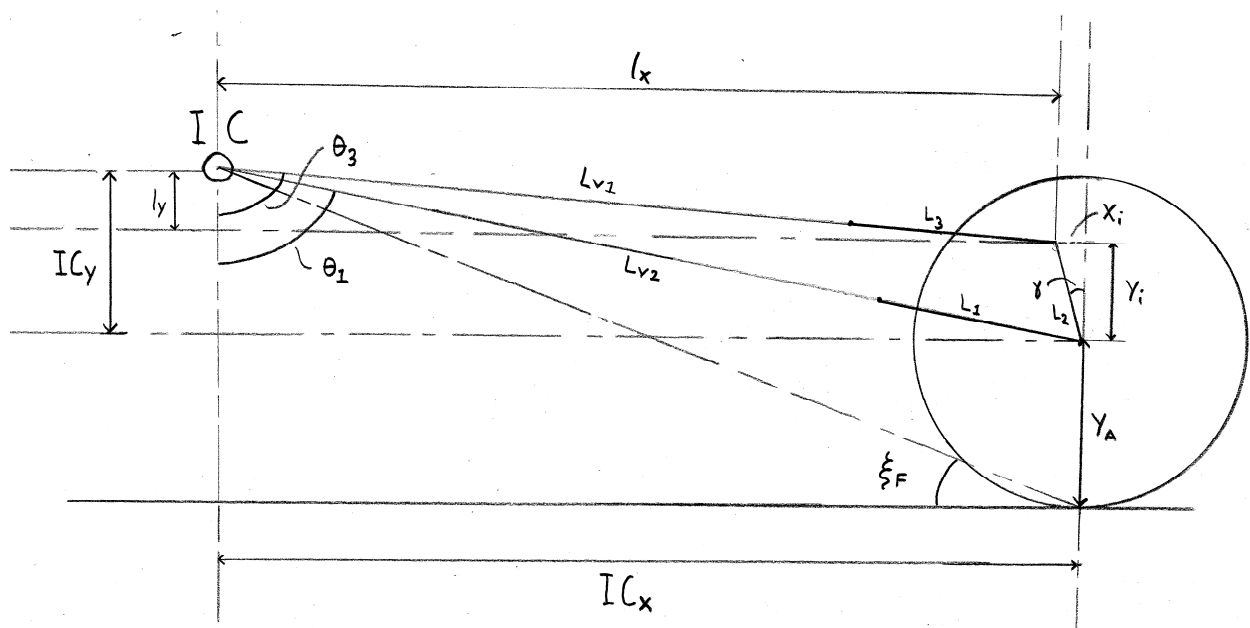


Figure 5.5. The anti-dive model geometry, used to derive an expression for the angle ζ_F .

With these distances ξ_F is calculated with

$$\tan \xi_F = \frac{IC_y + y_A}{IC_x} \quad (5.29)$$

As displayed in Figure 5.5 two virtual link arms with designation L_{V1} and L_{V2} are introduced. These arms are an extension of the existing linkages to IC. The supplementary distances l_x , l_y , x_i and y_i are calculated with

$$l_x = L_{V1} \sin \theta_3 \quad (5.30)$$

$$l_y = L_{V1} \cos \theta_3 \quad (5.31)$$

$$x_i = L_2 \sin \gamma \quad (5.32)$$

$$y_i = L_2 \cos \gamma \quad (5.33)$$

The horizontal distance IC_x is calculated with two possible equations

$$IC_x = L_{V2} \sin \theta_1 \quad (5.34)$$

$$IC_x = l_x + x_i \quad (5.35)$$

where both contain the unknowns L_{V1} and L_{V2} . Combining equation (5.34) and (5.35) together with (5.30) and (5.32) gives an equation for the lower virtual link arm, L_{V2}

$$L_{V2} = \frac{L_{V1} \sin \theta_3 + L_2 \sin \gamma}{\sin \theta_1} \quad (5.36)$$

The vertical distance IC_y is calculated in the same way with two possible equations

$$IC_y = L_{V2} \cos \theta_1 \quad (5.37)$$

$$IC_y = l_y + y_i \quad (5.38)$$

Combining equation (5.37) and (5.38) with (5.31) and (5.33), the second equation with only L_{V1} and L_{V2} as unknowns is acquired

$$L_{V2} = \frac{L_{V1} \cos \theta_3 + L_2 \cos \gamma}{\cos \theta_1} \quad (5.39)$$

The two equations (5.36) and (5.39) are used to calculate the length of the upper virtual link arm L_{V1} ,

$$L_{V1} = \frac{L_2 \cos \gamma - \frac{L_2 \sin \gamma}{\sin \theta_1} \cos \theta_1}{\frac{\sin \theta_3}{\sin \theta_1} \cos \theta_1 - \cos \theta_3} \quad (5.40)$$

and when L_{V1} is known, so is also L_{V2} by equation (5.39).

Calculating L_{V1} and L_{V2} enables IC_x and IC_y to be computed and ζ_F being obtained with equation (5.29). With ζ_F calculated, all terms in equation (5.28) are known except the value for the brake ratio.

5.3.1 Output and validation

Simulating wheel travel using the same temporary suspension linkage from the kinematic analysis, though complemented with the anti-dive model, gives the result graph for anti-dive ratio displayed in Figure 5.6. In this simulation it is assumed that all brake torque is generated at the front wheel, representing a *front brake ratio* equal to one.

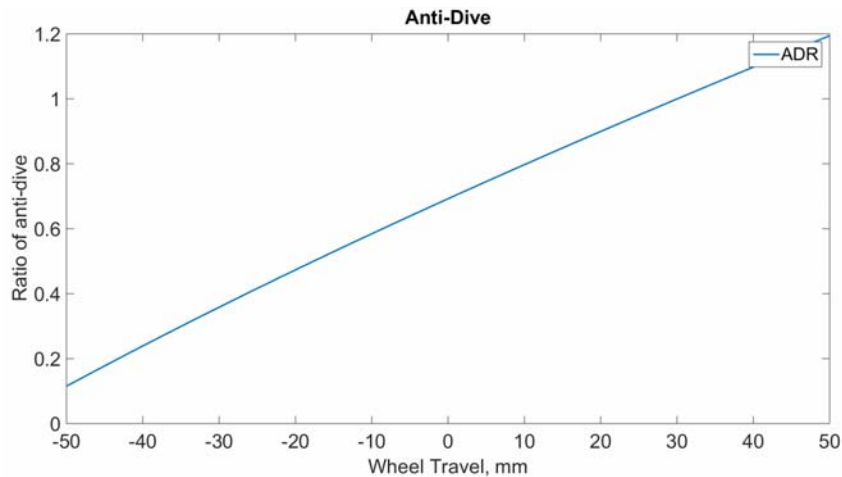


Figure 5.6. Anti-dive ratio for the temporary suspension linkage with a front brake ratio equal to one.

The virtual links in the anti-dive model are added to the animation which is utilized a second time around to validate the Matlab code. Screenshots of the extended animation are presented in Figure 5.7.

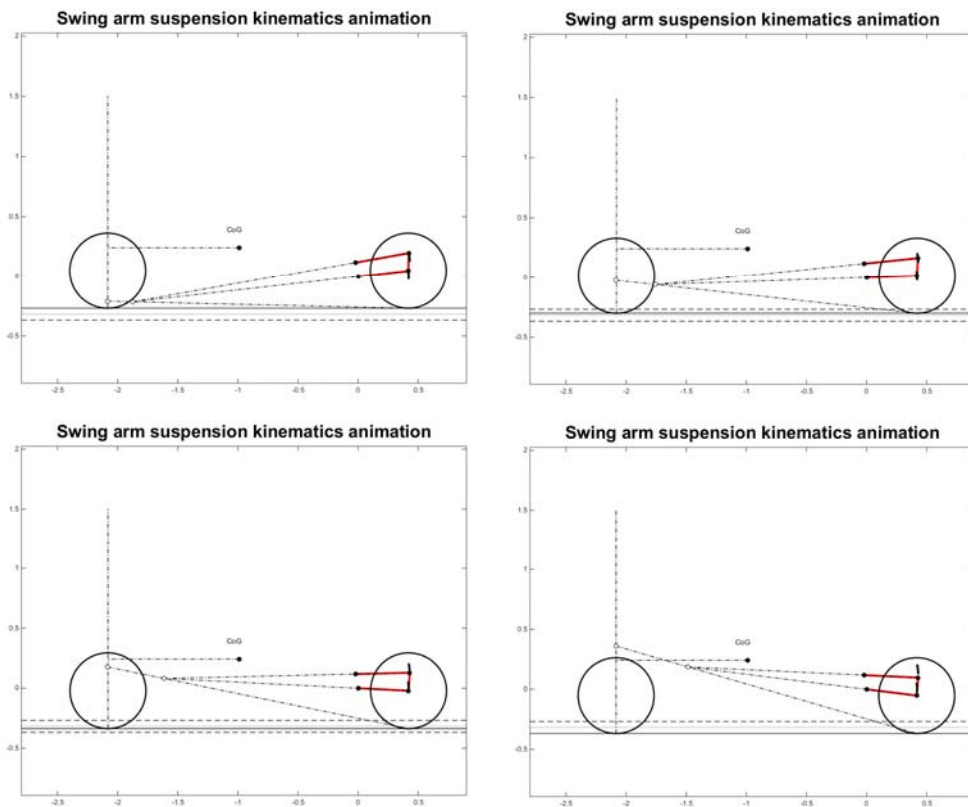


Figure 5.7. Screen shots of the animation complemented with result from the anti-dive model.

5.4 Ideal braking model

In a car the brake force applied onto the brake pedal is decoupled between the front and rear wheel pairs with the *brake ratio*. The brake ratio is generally a static value during operation and adjusted when the car is stationary (Milliken & Milliken, 1995).

Conventional two wheeled vehicles, especially motorcycles possess a configuration of mass, power, wheelbase length and CoG height that gives a possibility to reach load transfer that exceeds the static wheel loads. This range of load transfer also requires a large span in brake ratio values where the extreme case is when the rear wheel loses contact to the ground. With a vertical load on the rear wheel reaching zero there is no point of distributing driver brake force to the rear as the wheel is unable to produce braking force. All brake force should instead be fed to the front wheel, corresponding to a brake ratio equal to one. In a motorcycle, a fixed brake ratio value would therefore be ineffective, why the front and rear brake inputs are generally completely decoupled in two separate levers controlled by the rider (Cossalter, et al., 2004).

Equation (5.28) clarifies that the amount of anti-dive is dependent on the vehicle's distribution of brake force. A brake ratio must be derived in order to design an anti-dive suspension.

5.4.1 Deriving ideal brake ratio

By analytically analyzing a simplified deceleration sequence a relatively accurate prediction for the ideal brake ratio can be made (Cossalter, et al., 2004). By assuming a flat road and neglecting the contribution from rolling resistance and aerodynamic forces the normal loads calculated with equation (5.6) and (5.8) are reduced to

$$N_r = mg \frac{x_g}{b} + m\ddot{x} \frac{h_g}{b} \quad (5.41)$$

$$N_f = mg \frac{b - x_g}{b} - m\ddot{x} \frac{h_g}{b} \quad (5.42)$$

and the tractive/braking force in equation (5.10) is

$$F_{tot} = F_r + F_f = m\ddot{x} \quad (5.43)$$

The direction of the inertial force, $m\ddot{x}$, in the rigid vehicle model implies that the vehicle is in a state of acceleration, consequently when decelerating the acceleration \ddot{x} is negative. If infinite tire adhesion is possible, equation (5.41) may be used to derive the maximum deceleration before rear wheel lift, $N_r = 0$,

$$\ddot{x} = -g \frac{x_g}{h_g} \quad (5.44)$$

where the negative sign indicates a deceleration.

Denominate the brake ratio with ε , it is defined by the ratio of the *rear* over the *total* braking force,

$$\varepsilon = \frac{F_r}{F_{tot}} \quad (5.45)$$

Infinite tire adhesion is however not possible and for efficient braking tire adherence must be sustained throughout the entire maneuver, otherwise tire skidding occurs. The maximum adherence of the tires are given by the tire friction coefficients $\mu_{t,f}$ and $\mu_{t,r}$. Skidding is analyzed

with a normalized braking load μ_f and μ_r defined as the ratio between braking force and normal load,

$$\mu_f = \frac{F_f}{N_f}, \quad \mu_r = \frac{F_r}{N_r} \quad (5.46)$$

If the normalized load fulfills the adhesion limit criteria,

$$\begin{aligned} \mu_f &< \mu_{t,f} \\ \mu_r &< \mu_{t,r} \end{aligned} \quad (5.47)$$

skidding is avoided (Cossalter, et al., 2004).

Depending on the brake ratio and the load transfer, one of the wheels will reach the adhesion criteria before the other and launch the vehicle into a skid. The *ideal braking condition* for any vehicle is when the tires are stressed equally, meaning that all brake force generating tires should approach their adhesion limit simultaneously. The ideal braking condition is expressed mathematically as

$$\frac{\mu_f}{\mu_r} = \frac{\mu_{t,f}}{\mu_{t,r}} \quad (5.48)$$

If equation (5.48) is enforced, the maximum deceleration without skidding can be achieved. Another positive aspect of the ideal braking scenario is more predictable handling as the tire behavior will stay approximately identical. If the front and rear tires have the same adhesion limit then the right hand side of equation (5.48) equals to one. Combining equation (5.48) and (5.46) together with the simplified equations of motion and the definition of the brake ratio, equation (5.45), an ideal brake ratio is derived as

$$\varepsilon_{id} = \frac{x_g + \ddot{x} \frac{h_g}{g}}{b} \quad (5.49)$$

(Cossalter, et al., 2004).

Calculating the ideal brake ratio over the entire range of deceleration is made possible with equation (5.49). However, in order to find the brake ratio at the verge of skidding the actual deceleration at this point must be known. Since the tires have the same coefficient of friction the total braking force at the point of skidding is calculated with

$$F_{skid} = (N_f + N_r) \mu_t = mg \mu_t \quad (5.50)$$

Equation (5.43) also describes the total braking force and how it correlates to the inertial force, by equating these two equations the expression for maximum deceleration is given with

$$F_{skid} = F_{tot} \Rightarrow \ddot{x} = -\mu_t g \quad (5.51)$$

The negative sign is again an indication that the vehicle is in a state of deceleration.

5.4.2 Measuring tire friction coefficient

A wheel comprised of a hub motor, rim, wheel center and the Michelin Pilot Road 3 tire are available at *KTH ITRL* and used for deriving the friction coefficient of the tires. First the entire assembly is weighed using a lift scale, see Figure 5.8.



Figure 5.8. Weighing the wheel assembly used for friction coefficient measurement (resting on ground).

Secondly, a simple measurement of the friction coefficient between the tire and dry asphalt is performed. Wheel rotation is constrained, though still allowing translation, and by pulling the scale parallel to the ground the force required to bring the tire to the point of skidding is measured.



Figure 5.9. The setup for measuring tire friction coefficient, during measuring wheel rotation is constrained.

The friction coefficient is calculated using equation (5.46) with the vertical and horizontal loads recorded in the measurements. Because of the simple testing setup and the low resolution readings the average of two measurements is calculated, see Table 5.5. Integers are used as the level of accuracy when denoting the measured friction force due to measurement noise caused by continuous stick slip of the tire and insufficient restraint of its rotational motion.

Table 5.5. Results from the measurements for the tire friction coefficient on dry asphalt.

Measurement No.	Normal load (weight), N_w [kg]	Friction (pull) force, F_w [kg]
1	30	25
2	30	25
Averaged result	30	25
Friction coeff., $\mu_t = F_w/N_w$	0.83	

The validity of these measurements may be established by comparing the magnitude of the friction coefficient to general coefficient of friction values. With dry conditions and common asphalt used in the measurements the range of general tire friction coefficients are typically around 0.8 - 0.7 depending on the speed (Gillespie, 1992).

5.4.3 Output

Knowing the friction coefficient of the tires, each wheel's maximum brake force is calculated for a range of decelerations according to equation (5.46). The forces are illustrated in Figure 5.10 as the black lines enclosing the grey area to the left in the graph. The intersection of these two lines represents the point when both tires starts skidding simultaneously. The grey area represents all the possible combinations of front and rear braking resulting in a non-skid deceleration.

The ideal braking ratio, also presented in Figure 5.10, passes through the intersection point according to the definition of ideal braking. This curve represents a varying brake ratio for increased decelerations. If tire adherence was to be sustained for all cases the maximum brake force just before rear wheel lift is acquired with all braking on the front wheel. The ideal braking value at the intersection point and at the verge of skidding is

$$\varepsilon_{id} = 0.375 \tag{5.52}$$

meaning that 37.5 % of braking force is routed to the rear wheel. The straight linear curve illustrates the brake force coupling with this fixed ratio during all decelerations up to the point of skidding.

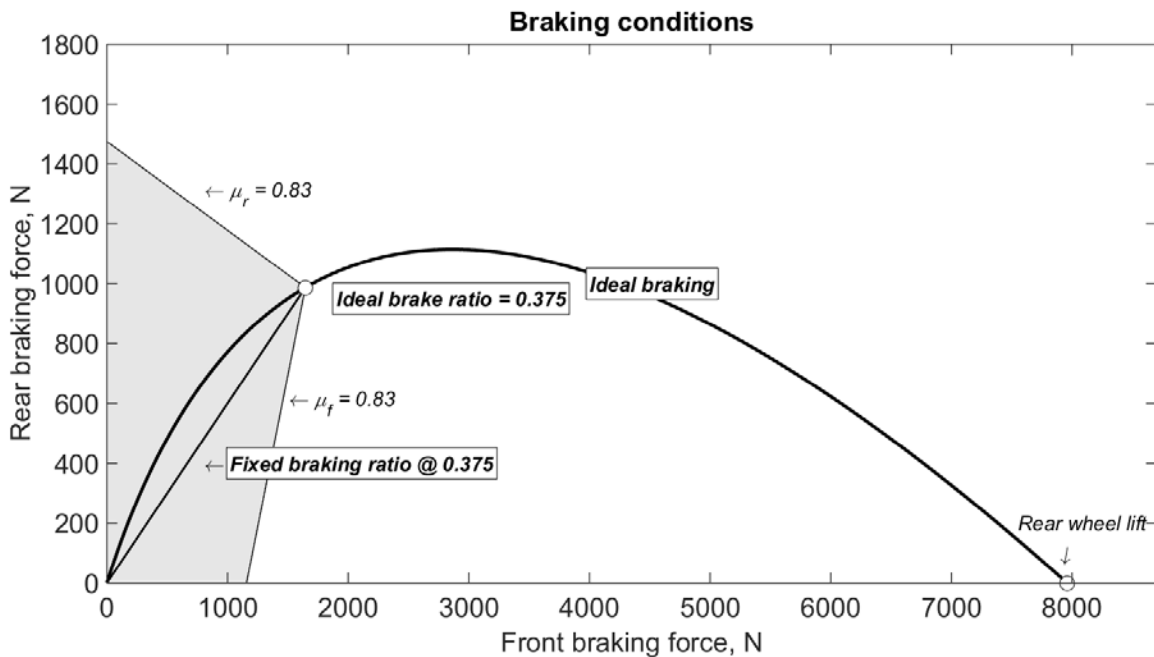


Figure 5.10. Braking curves for front and rear wheel, ideal braking and an ideal fixed brake ratio.

With the rate of deceleration and brake ratio known the final braking torques for the front and rear wheels can be calculated with the rigid vehicle model. The inputs and outputs of the last deceleration case are presented in Table 5.6.

Table 5.6. The last case calculated by the rigid vehicle model.

Case		Speed, [m/s]		Acceleration, [m/s²]	Incline, [°]
Constant decel.	100 - 0 kph in 3.4 s	27.8 - 0		-8.17	0
		Normal load, [N]		Wheel torque, [Nm]	
		Front	Rear	Front	Rear
		1934.5	1170.3	508.9	307.9

5.5 Optimization

5.5.1 Optimization theory

To be able to find the geometrical combination that provides a satisfactory suspension motion an optimization routine is implemented.

In mathematical terms optimization means finding the minimum of a desired function, called the *objective function*. There are different types of routines that can be used to find a solution e.g. *Newtons method* and *Steepest Descent*. One of the simplest forms of optimization is, after computing the derivative of a one variable function, equaling it to zero and solving for the dependent variable which can be referred to as the *design variable*. Only looking at the first derivative is tough not always enough as there is no guarantee for the solution to be a minimum of the function, it could also be a maximum. A second condition must also be fulfilled to ensure that it is in fact a minimum. The other condition is that the second derivative must be equal to or larger than zero. These conditions are called the *first order optimality condition* and *second order necessary optimality condition* and together with the *objective function* makes up the unconstrained optimization (Ringertz 2000).

In mathematical expressions the optimization of an objective function $f(x)$ becomes

$$\min_x f(x) \begin{cases} f'(x^*) = 0 & \text{1st order opt. condition} \\ f''(x^*) \geq 0 & \text{2nd order opt. condition} \end{cases}$$

where x^* is the solution. For optimization of objective functions with several variables the theory is basically the same but the expressions needs some adjustments to apply on multivariable problems.

$$\min_x f(x), x \in \mathbb{R}^n \begin{cases} \nabla f(x^*) = \bar{0} & \text{1st order opt. condition} \\ y^T F(x^*) y \geq 0 \quad \forall y & \text{2nd order opt. condition} \end{cases}$$

The second order optimality condition is fulfilled if the hessian matrix $F(x)$ is positive definite, meaning its eigenvalues $\lambda_i > 0$ (Ringertz, 2000).

Matlab have existing algorithms that can be utilized when an optimization routine is going to be implemented. For instance, the command called `fmincon` can be used to find the minimum of a constrained nonlinear multivariable function. Provided the objective function, design variables and a vector of constraints, `fmincon` computes the combination of design variables that yields the minimum solution based on a predefined algorithm chosen by the user (MathWorks, 2014).

5.5.2 Optimization routine

When combining the analytical models it is possible to calculate the resulting anti-dive properties of any specified geometry during full wheel travel. Secondary outputs, such as the change in steering axis inclination angle and wheel horizontal displacement are also attained from the kinematic analysis.

Evidently the models only require an initial guess of suspension geometry to calculate the anti-dive properties, wheelbase change and steering axis inclination change. A geometry is possibly established by manually iterating HP to a satisfying output, however implementing a Matlab based optimization with the linkage geometry as design variables is considered preferable. With an algorithm based iteration procedure the geometry design process is also parameterized and new constraints can easily be included.

The pre-defined Matlab function `fmincon` is called to execute the optimization, provided with an objective function, initial guess of the design variables and nonlinear constraints.

5.5.3 Objective function

As described in the previous section the output of the objective function is the value that the optimization routine strives to minimize. For the anti-dive properties to remain approximately constant during wheel travel the graph displayed in Figure 5.6 should be as flat as possible. Assuming that the angular change of ζ_F in equation (5.28) is small the anti-dive curve should be more or less linear, illustrated by the anti-dive curve for the temporary suspension in Figure 5.6. With a linear relationship a reasonable objective function striving to flatten the curve would be to minimize the difference between the maximum and minimum value. Thus the objective function for the optimization routine is

$$f(x) = \max(\mathbf{ADR}) - \min(\mathbf{ADR}) \quad (5.53)$$

5.5.4 Design variables

The design variables (DV) are the parameters which are tuned by the optimization algorithm when iterating to a minimum value. Based on the model defined in the kinematic analysis illustrated in Figure 5.2, the DV are

$$\mathbf{DV} = [L_1 \ L_2 \ L_3 \ L_4 \ \varphi \ y_0] \quad (5.54)$$

By establishing the length of these linkages, the angle φ and the vertical distance from the ground to the local coordinate system y_0 , the front suspension HP coordinates are completely determined. To avoid unreasonable and impractical results a first set of constraints are also given to the optimization, the minimum and maximum permissible values for the DV.

5.5.5 Nonlinear constraints

The next set of constraints are the so called nonlinear inequality constraints, which is a set of conditions dependent on the DV that the optimization must take into account when finding a solution. Looking at the objective function there is actually no restrictions on the value of the anti-dive ratio. It is only specified that the difference between the minimum and maximum value should be as small as possible. A suitable condition to place within the nonlinear inequality constraints is therefore the range of allowed anti-dive ratio. Matlab can only enforce one condition at each position of the constraint vector, why such a restraint must be split into two.

$$ADR_{\min} \leq \min(\mathbf{ADR}) \quad (5.55)$$

$$\max(\mathbf{ADR}) \leq ADR_{\max} \quad (5.56)$$

where ADR_{\min} and ADR_{\max} are the chosen limits of the ADR span.

The torque arm has two inherent functions, to guide the wheel during wheel travel and transmit braking induced loads into the chassis. Assuming that the torque strut angle towards the horizontal is small, the effective lever for braking loads of the torque arm decrease with its increased inclination. To constrain the maximum inclination the inequality constraint

$$\max(\gamma) \leq \gamma_{\max} \quad (5.57)$$

is used. Where γ_{\max} is the maximum angle for the torque arm during the whole range of wheel travel.

The horizontal motion of the wheel is constrained by enforcing an inequality constraint for the maximum allowed horizontal wheel travel. The wheel center coordinates during suspension travel is available in vector \mathbf{A}_x , calculated with equation (5.21). The inequality constraint for horizontal wheel travel is

$$\max(\mathbf{A}_x) - \min(\mathbf{A}_x) \leq \Delta WT_x \quad (5.58)$$

where ΔWT_x is the maximum allowed horizontal wheel travel.

The importance of trail and how it contributes to the straight line stability has been mentioned in section 3.2. Steering axis offset is not included in the models why the steering axis inclination angle will be the sole parameter affecting trail. If the angular change of the steering axis during wheel travel is sufficiently small the difference in trail may be negligible and allowed to transpire.

By neglecting solid mechanic elasticity, the steering axis and torque arm are stationary relative each other. Examining the angular change of the torque arm is therefore sufficient to establish the angular motion of the steering axis, hence the final inequality constraint is applied to the torque arm angle vector γ ,

$$\max(\gamma) - \min(\gamma) \leq \Delta \gamma_{\max} \quad (5.59)$$

Where $\Delta \gamma_{\max}$ is the maximum allowed change in steering axis inclination angle.

5.5.6 Input & output

Depending on the optimization constraints the vehicle will show different driving characteristics e.g. the steering axis inclination affects trail which in turn affects the restoring torque. In further development, the ADAMS model created in this thesis should be used to examine the driving behavior more thoroughly and to revise the optimization constraint values if needed. An initial set of constraints are assigned based on assumptions of desired suspension and steering characteristics, see Table 5.7

Table 5.7. Initial guesses and constraints in the optimization routine.

Type	Designation	Unit	Initial guess	Value	
				min	max
Design variables	L1	mm	420	0.35	0.5
	L2	mm	150	0.15	0.2
	L3	mm	430	0.35	0.6
	L4	mm	150	0.1	0.35
	φ	deg	5	-30	20
	y_0	mm	318	0.25	0.38
Nonlinear inequality constraint	ADR	-	-	0.7	1
	γ_{\max}	deg	-	-	10
	ΔWT_x	mm	-	-	20
	$\Delta \gamma_{\max}$	deg	-	-	5

The solver is able to find a local minimum with the specified input, a full review of the optimization output, e.g. number of iterations, optimality conditions etc. is available in

APPENDIX I. The DV, horizontal wheel displacement and angular change of the steering axis found through the optimization routine are presented in Table 5.8.

Table 5.8. Resulting suspension geometry from the optimization scheme.

Output	Designation	Resulting value	Unit
Swing arm length	L1	467.7	mm
Torque arm length	L2	192.2	mm
Torque strut length	L3	361.2	mm
Pivot points distance	L4	158.1	mm
Pivot points angle	ϕ	-29.6	deg
Distance to local origin	y_0	370.5	mm
Total angular change of steering axis	-	3.4	deg
Total horizontal wheel displacement	-	11.9	mm

With the objective function striving to flatten the anti-dive curve while still enforcing the inequality constraints an anti-dive ratio ranging from approximately 0.75 to 1 is obtained, see Figure 5.11.

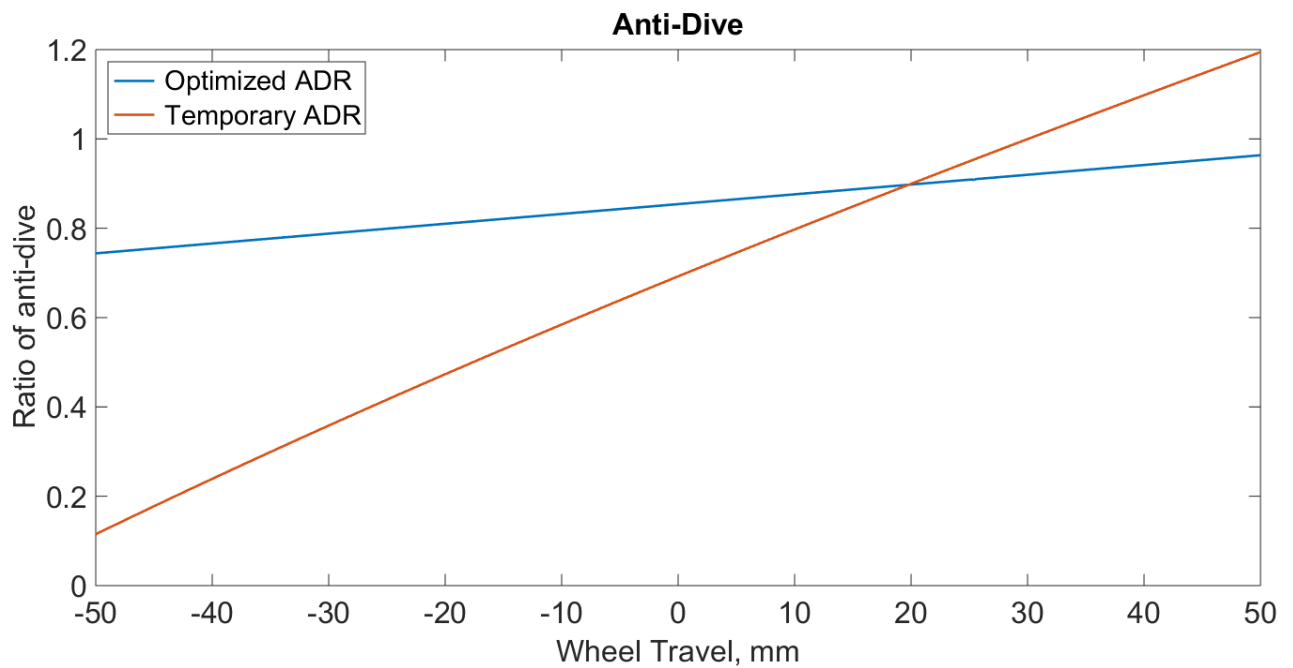


Figure 5.11. The temporary and optimized ADR for the suspension linkage.

The suspension HP coordinates in the two dimensional local coordinate system are presented in Table 5.9 together with their representative coordinates in the xz-plane in the global coordinate system.

Table 5.9. Suspension HP in the local and global coordinate system.

Hardpoint		Local coordinate, mm		Global coordinate, mm	
Local name	Global name	x	y	x	z
0	Front_swing_rear	0.00	0.00	-464.5	370.5
A	Wheel_center_front	464.5	-54.8	0.0	315.7
B	Front_strut_front	438.5	135.8	-25.9	506.3
C	Front_strut_rear	78.2	137.4	-386.3	507.8

5.6 Transient half vehicle model

The half vehicle model is a tool used to model and simulate the transient dynamic behavior of a suspended mass connected to an elastic wheel by a spring and shock absorber. For this system the spring and shock absorber are modeled as equivalent representations to the real life components and their properties effective at the wheel center. The equivalent spring stiffness is generally termed *wheel center rate* to distinguish it from the actual spring rate specified by the coil mounted to the vehicle. The half vehicle system is modeled as in Figure 5.12, where m_v represents half of the sprung vehicle mass and m_u the unsprung mass in one wheel.

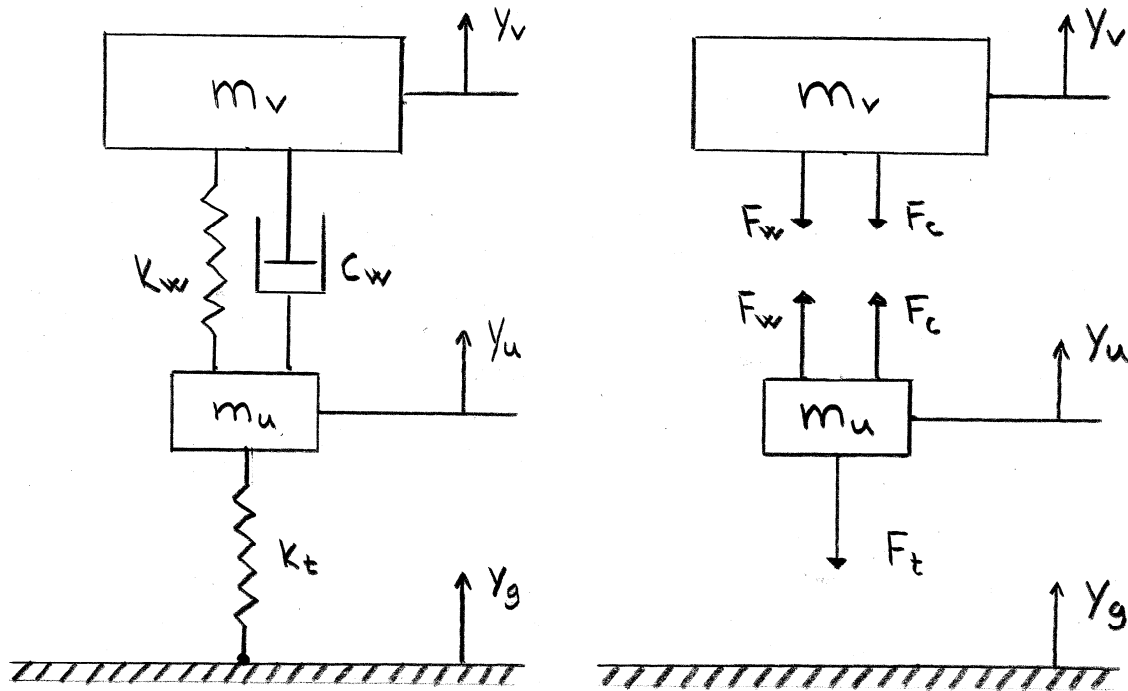


Figure 5.12. The layout and representative free body diagram of the transient half vehicle model. The inertial force generated by acceleration when oscillating has been excluded from the figure.

The static gravitational force acting on the masses can be ignored if it is assumed that the system start oscillating from equilibrium. The gravitational force is cancelled out by an equivalent static load in the springs caused by initial compression. When constructing the free body diagram, the direction of the forces are initially defined as if the springs were compressed. The compressed springs exerts a push force onto the masses and the bodies' reaction forces are consequently in the direction displayed in Figure 5.12.

This model is also used when analyzing cars, though referred to as the *quarter car model* (Milliken & Milliken, 1995). The half vehicle model gives the possibility to test a range of spring and damper coefficients and examine the resulting natural frequencies and accelerations.

The real life spring and damper fitted to Newt will not be positioned as in the half vehicle model, and the concept of installation ratio (IR) must be introduced. The IR is used to translate the wheel center rate, and also the equivalent damping ratio, into the actual spring and damping rates. This is possible since the IR is a gauge over the amount of spring deflection given by a finite vertical wheel center displacement. The effect of the IR is not only limited to displacements, the force fed into the spring and damper is also proportionally dependent on the IR. This coupling of force and displacement means that the wheel center rate and spring rate are proportional to the *IR* squared,

$$k_w = k_s (IR)^2 \quad (5.60)$$

where k_w is the wheel center rate and k_s is the real life spring rate. Equation (5.60) is only valid if the IR is constant during wheel travel, which is rarely the case however it may serve as a rough approximation. The full expression also takes into account the change of IR during wheel displacement

$$k_w = F_s \left(\frac{\Delta IR}{\Delta \delta} \right) + k_s (IR)^2 \quad (5.61)$$

where F_s is the spring force and $\Delta IR/\Delta \delta$ is the change of IR with wheel displacement (Milliken & Milliken, 1995).

5.6.1 Deriving the model

In the coordinate systems defined in Figure 5.12, the spring forces F_w and F_t are derived using Hooke's law

$$F_w = k_w (y_v - y_u), \quad F_t = k_t (y_u - y_g) \quad (5.62)$$

where k_w is wheel center rate and k_t the stiffness of the tire. The damper force F_c is

$$F_c = c_w (\dot{y}_v - \dot{y}_u) \quad (5.63)$$

where c_w is the equivalent damping rate coefficient. With these definitions for the spring and damper forces, the equilibrium equations for the free body diagram in Figure 5.12 are

$$\begin{cases} m_v \ddot{y}_v = -k_w (y_v - y_u) - c_w (\dot{y}_v - \dot{y}_u) \\ m_u \ddot{y}_u = k_w (y_v - y_u) + c_w (\dot{y}_v - \dot{y}_u) - k_t (y_u - y_g) \end{cases} \quad (5.64)$$

The equations in (5.64) comprise a familiar system of 2nd order differential equations describing the dynamics of two bodies connected via springs and a damper. Matlab has a number of predefined tools for dealing with differential equations. These methods are suited for systems of 1st order equations. The 2nd order differential equations are however easily transformed into a system of 1st order equations with a variable substitution

$$\begin{cases} \dot{y}_v = z_v; \quad \dot{y}_u = z_u \\ m_v \dot{z}_v + c_w (z_v - z_u) + k_w (y_v - y_u) = 0 \\ m_u \dot{z}_u + c_w (z_u - z_v) + (k_t + k_w) y_u - k_w y_v = k_t y_g \end{cases} \quad (5.65)$$

This system of equations can be solved with various differential equation solvers in Matlab, here the solver ode45 is chosen.

5.6.2 Road input

The excitation input that causes motion to occur in the system originates from the irregularities in the road, more specifically the ground coordinate, y_g . To analyze the response given from the half vehicle model, road profiles with different excitation geometry are used as input to the differential equation solver.

Depending on the case the geometry of the road varies, it can be a single bump, a washboard road or a real life representative road profile. The input to the transient model is however the same for all roads. The y_g coordinate is calculated along all positions of the ground according to

$$y_g = y_g(x) \quad (5.66)$$

and then passed to the ode45 function.

The equivalent stiffness of the entire half vehicle model is called the *ride rate* (RR) and is calculated with

$$RR = \frac{k_w k_t}{k_w + k_t} \quad (5.67)$$

The RR may then be utilized when calculating the undamped natural frequency of the system

$$\omega_n = \sqrt{\frac{RR}{m_v}} \text{ rad/s} \Rightarrow f_n = \frac{1}{2\pi} \sqrt{\frac{RR}{m_v}} \text{ Hz} \quad (5.68)$$

where m_v equals the weight of the sprung mass in the model.

Using the damping ratio,

$$\zeta_w = \frac{c_w}{\sqrt{4k_w m_v}} \quad (5.69)$$

the damped natural frequency is also calculated

$$\omega_d = \omega_n \sqrt{1 - \zeta_s^2} \quad (5.70)$$

(Gillespie, 1992).

5.6.3 Output and code validation

To resemble the driving experience of a car, automotive target values for natural frequency and damping ratio are used together with their corresponding equations to derive suitable suspension coefficients.

For a normal passenger car the damping ratio, ζ_s should be in the range of 0.2 - 0.4 and the natural frequency ranging from 1 - 1.5 Hz. For a sports car the natural frequency is approximately 1 Hz higher, around 2 - 2.5 Hz (Gillespie, 1992).

The stiffness ratio between tire and wheel center rate is defined as

$$r_k = \frac{k_t}{k_w} \quad (5.71)$$

A stiffness ratio equal to 5 is representative for a racing car while $r_k = 20$ is found in the softest luxury cars utilizing air springs (Gillespie, 1992). Table 5.10 presents the calculated coefficients in the transient half vehicle model.

Table 5.10. Properties for the transient half vehicle model.

k_w [N/m]	c_s [Ns/m]	Natural freq, f_n [Hz]	Damping ratio, ζ_s [-]	Stiffness ratio, r_k [-]
25000	1500	2.043	0.401	12.0

Providing the transient model with a road profile of a continuous sweep of sine waves with decreasing wave lengths generates a response over a range of excitation frequencies. In Figure 5.13 the magnitude of the sprung mass displacement is plotted over the frequency range, the natural frequency around 2 Hz is clearly visualized with the amplification in response.

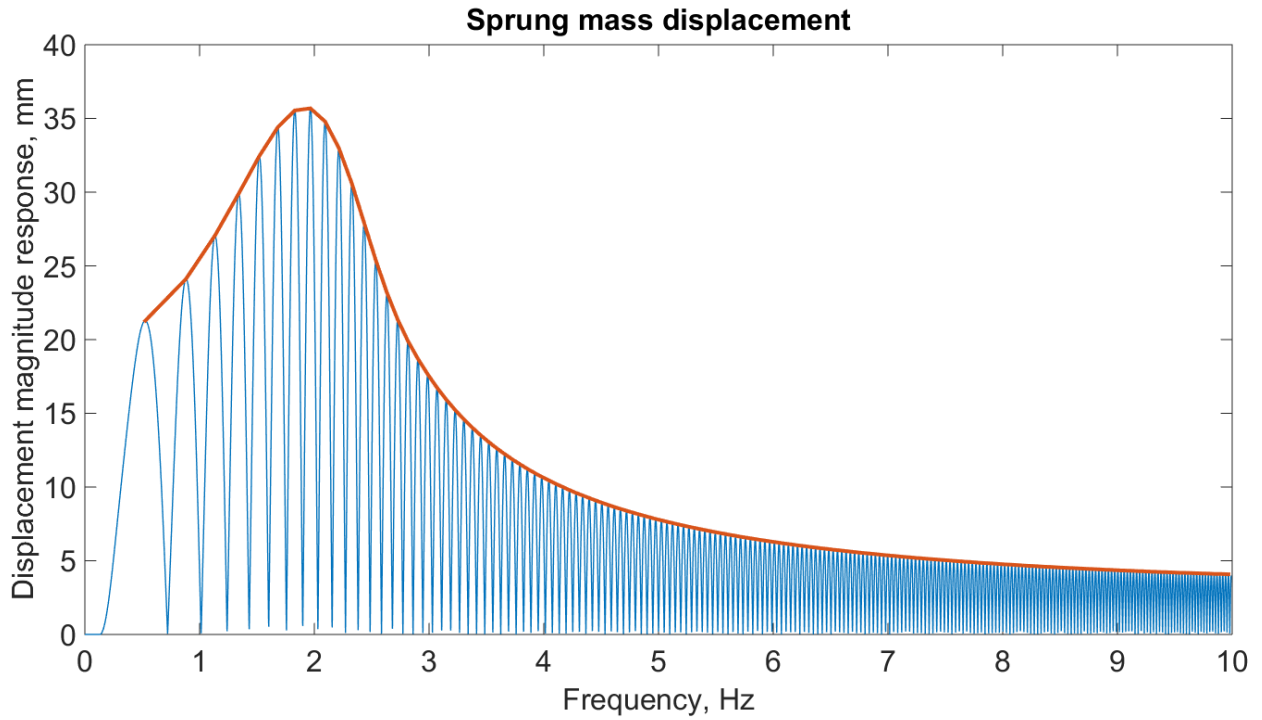


Figure 5.13. Response output from the dynamics model for a range of excitation frequencies.

An animation of the dynamic sequence, shown in screenshots in Figure 5.14, is used once again to validate the code and analyze if there are any discrepancies or discontinuities in the solution.

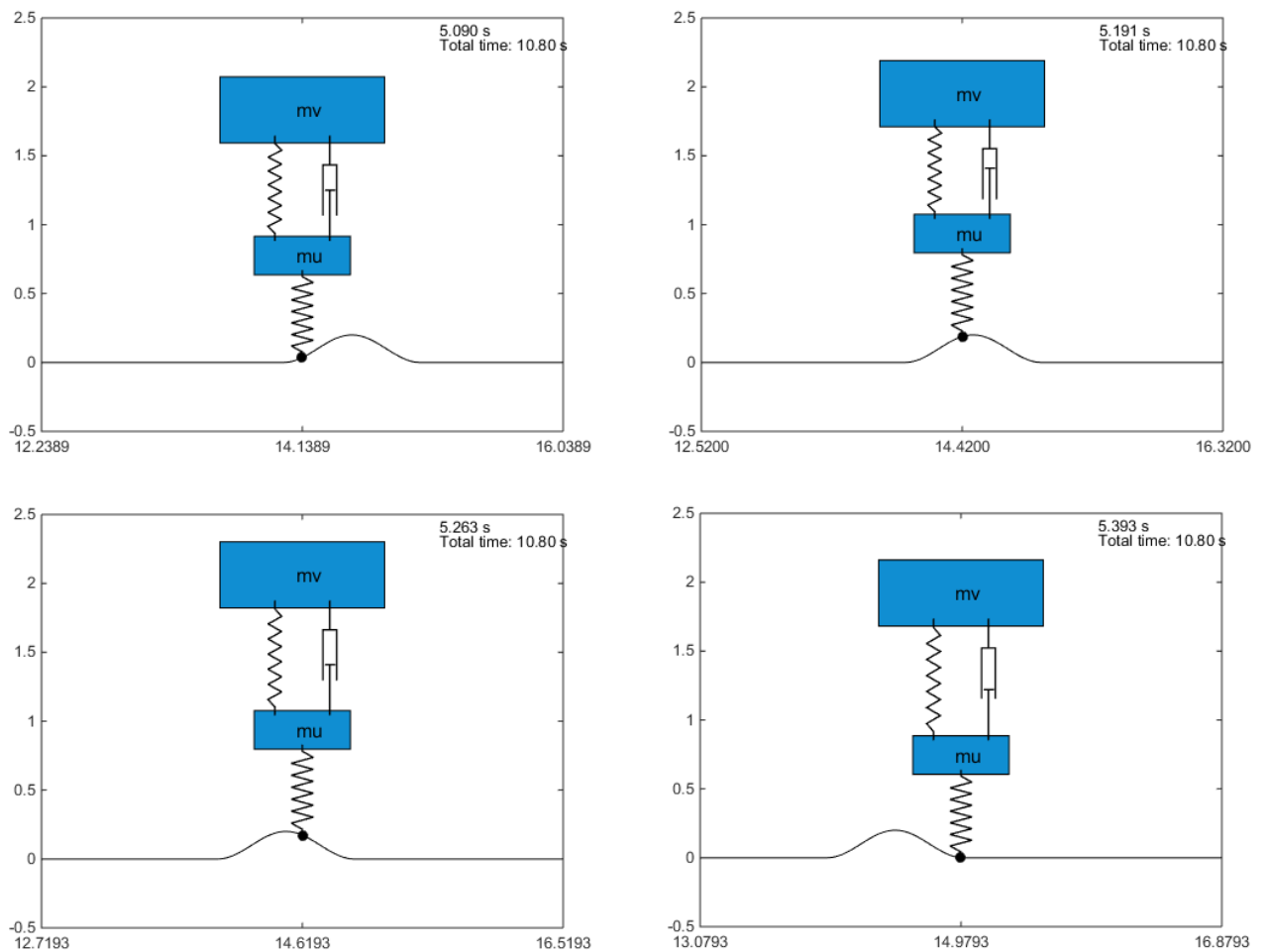


Figure 5.14. Validation of transient sequence by animating the maneuver.

6 ADAMS MODEL

This chapter presents the approach when building the ADAMS model and how it is tuned to ensure that it is a reliable dynamic representation of the vehicle.

Using the suspension geometry acquired through the analytical models the vehicle is modeled in ADAMS View. The multibody simulation software is used for validating the analytical models but also serves as a thesis deliverable. The iterative design process may later require modifications of the simulation models why the ADAMS model is also parameterized.

The delimitation to only focus on the front suspension system will be reflected in the ADAMS model. This part of the vehicle is modeled in detail with consideration to suspension HP and steering. In order to run dynamic full vehicle simulations a rear end is however required and a rear suspension featuring a simple single swing arm is included.

6.1 Building the model

6.1.1 HP, parts and joints

The ADAMS graphical user interface is used for creating the objects of the vehicle e.g. bodies such as links, cylinders and boxes, but also joints, forces and motions. When a body is created the software automatically generates a geometry defined by markers which controls the shape, position and orientation of the particular part. The Cartesian based markers use an x-,y- and z-axis to position and orient them in the global space. Instead of simply generating a body in the blank space *design points* can be utilized.

Design points are similar to markers though not necessarily affiliated with any part. Their location is only defined by x-,y- and z-coordinates as their orientation coincide with the global coordinate system. The design points created represent the suspension HP calculated in the analytical anti-dive model. Bodies which are defined by design points are automatically parameterized.

Wheels are a pre-defined entity in ADAMS and when imported they are coupled to a road specified by an input file. The input file contains information for the road and with a number of pre-defined roads available in the ADAMS default library different scenarios may be simulated, for instance a flat, pot-hole or washboard road. A tire property file is also required to be provided which contains the comprehensive information concerning tire parameters. Several pre-defined tire property files are also available through the ADAMS default library and a motorcycle type tire is chosen for the model. The tire property file is slightly modified so that the tires are of the correct size and have the vertical stiffness used in the analytical models. The wheels are also given the mass and inertia taken from the simple CAD model.

Several links are generated to create the suspension linkage and revolute joints are added to connect the links. The transverse axis and the torque arms are modeled as one solid part which is also fitted with a steering axle at a 20° inclination angle. The steering axle is connected to a wheel hub with a revolute joint to allow steering displacements. The ADAMS front suspension is displayed in Figure 6.1.

To reduce the influence of the links masses to the vehicle CoG the parts are assigned a low density. The decrease in inertia due to this simplification is negligible since the wheel has been assigned a mass and inertia accounting for the suspension mass.

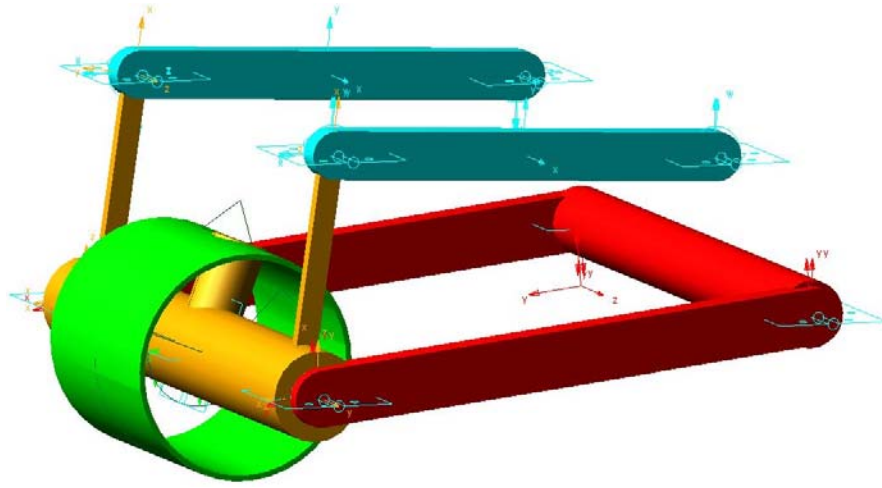


Figure 6.1. The front suspension linkages created in ADAMS. The red swing arm is modeled as a single part, so is the yellow transverse axis with torque arms and steering axis, the green cylinder is the wheel hub.

All parts except tires, springs and dampeners generated in this model are considered rigid meaning that there is no deflection or energy dissipation in those parts.

In order to run full vehicle simulations a rear suspension is created and since the rear wheel also experiences load transfer during accelerations/decelerations the swing arm geometry cannot be completely arbitrary. To avoid contribution to the pitching of the vehicle during braking an anti-lift suspension is required for the rear end. The anti-lift feature is the rear suspension equivalent to anti-dive, hence equation (5.28) describing the percentage anti-dive manifests as

$$ALR = BR_{rear} \cdot \tan(\xi_R) \cdot \left(\frac{b}{h_g}\right) \quad (6.1)$$

where ALR is the anti-lift ratio and naturally the rear brake ratio is used. The definition of $\tan(\xi_R)$ resembles that of the front. It is the angle from ground to a virtual line from the tire contact point through IC. The use of a single swing arm greatly reduces the complexity for the rear anti-lift calculation as the IC actually is the suspension HP. With a much greater length of the swing arm compared to the vertical displacement of the wheel and a stationary IC, the change in angle ξ_R is assumed negligible and the ALR considered constant.

Besides the anti-lift properties, the HP coordinates for the rear swing arm are established taking into account the vehicle ride height. The resulting coordinates and anti-lift percentage are presented in Table 6.1.

Table 6.1. Coordinates for the rear swing arm HP and the resulting ALR .

HP coordinate	x, [mm]	y, [mm]	z, [mm]
Rear swing, front	1834	±160	200
Rear wheel center	2500	0	318
Anti-lift ratio	0.87		

With the wheels and suspensions in place, the rest of the vehicle may be modeled. All the remaining parts that comprises the vehicle are represented by a box located between the wheels. The box is modeled so that its bottom plane is located at ride height, representing the undercarriage of Newt. From the simple CAD model the mass and CoG position is obtained for the vehicle without wheels and assigned to the properties of the box in ADAMS. Revolute joints are then placed between the suspension links and the box connecting them in the HP.

Being a two wheeled vehicle, a lateral disturbance will cause the model in ADAMS to capsize. Since there is no algorithm implemented to mimic the effects of the gyroscopic stabilization unit a primitive joint is applied to the center box which prevents the vehicle from rolling.

The last elements to include in the ADAMS model are the suspension springs and dampeners. The locations of these components in ADAMS are especially important since any effects due to IR are undesirable. To eliminate the IR the ADAMS spring-damper is connected to the wheel center and aligned vertically. The position enables the spring and damping rates from the transient half vehicle model to be directly implemented. The full vehicle model is displayed in Figure 6.2.

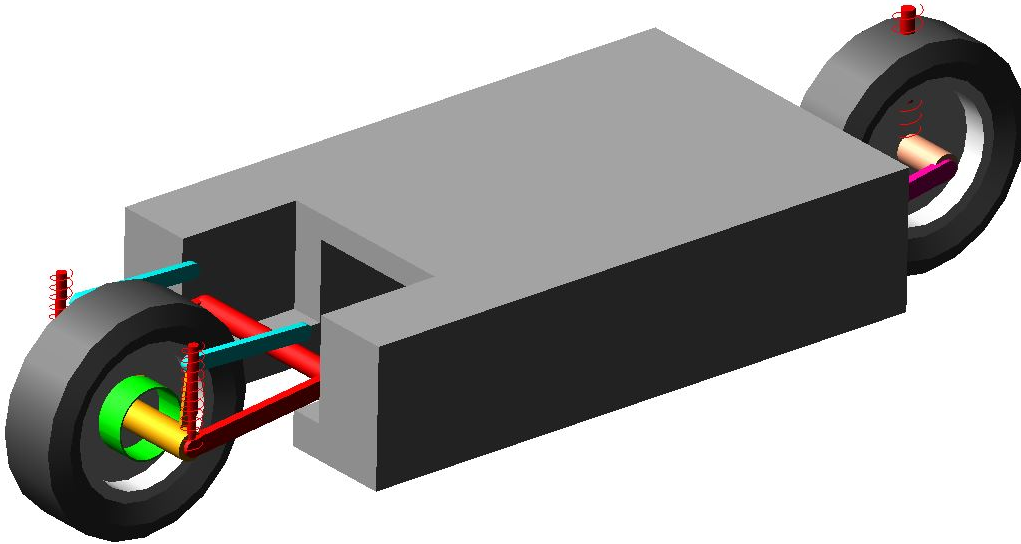


Figure 6.2. The full ADAMS model of the vehicle Newt.

6.1.2 Preload, external loads and steering motion

When specifying suspension HP in the modeling mode the vehicle is in its unloaded state meaning static equilibrium at standstill is not fulfilled. If an equilibrium simulation is performed the weight of the vehicle causes initial compression in the springs and tires. An effect of reaching the equilibrium state is that the location of the suspension HP changes slightly, most noticeable is the change in z-coordinate. To cope with this misalignment the suspension springs are preloaded which raises the vehicle back to proper ride height.

The adequate preload is found by measuring the height to two markers located on the bottom plane of the center box and tuning the preload iteratively. When the undercarriage reaches ride height the correct pre-load is established, plots showing this procedure is found in APPENDIX II. To ensure that the bottom plane is parallel to the ground and to eliminate initial preload pitching the two measurement markers are positioned on same height at the front and rear end of the box. When preload is applied and their z-coordinates on the same height, the vehicle is leveled.

Figure 6.3 displays the plot for the z-coordinate of the front and rear marker on the center box for the final preload. The plot shows the vehicle being dropped from its unloaded state and initially compresses the suspension, at around 0.75 seconds static equilibrium is reached. The plot also shows that the bottom plane returns to a ride height of approximately 170 mm.

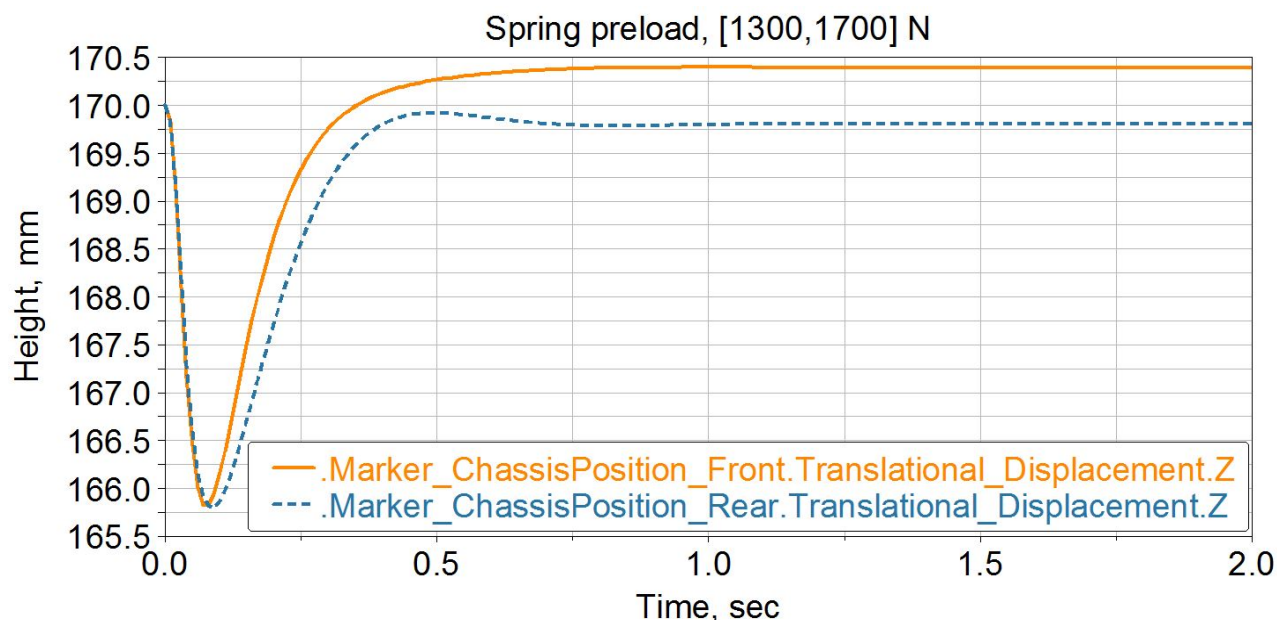


Figure 6.3. The final spring preload of 1300 N in the front and 1700 N in the rear. The height difference between the front and rear markers is approximately 0.6 mm, which is negligible.

The last inputs to the model are the external loads acting on the vehicle. The tractive and braking torques are applied on the wheels with the magnitude and operating time derived in the rigid vehicle model. The torques are managed with step functions to be able to fully control the motion of the vehicle e.g. accelerate to a certain value, run at constant speed and finally decelerate to full stop.

The last external load is the drag force caused by aerodynamic effects. It is applied to the CoG as in the rigid vehicle model, with a direction that counteracts the motion of the vehicle. The drag is coupled to a marker measuring the speed, thus the correct magnitude of the force is calculated with the definition of the drag force, equation (5.1).

The steering revolute joint is fixed to be able to run straight line simulations however if steering is required, motion can easily be imposed on the joint. For instance specifying a function for displacement e.g. a sine curve for oscillating the front wheel.

6.2 Load case for structural analysis

At the current level of detail the ADAMS model's main purpose is to simulate dynamic behavior. When modified to take into account the lateral coordinates and the individual part's mass and inertia, simulations aiming to extract dimensioning loads may commence. The dimensioning loads will then be used in detailed structural analyses for the parts. Simplified structural analysis will however be implemented in the conceptual design proposals to ascertain that the design is feasible in terms of strength.

The load case chosen for the simplified analysis is a combination of braking torque and vertical load. The torque is acquired from the rigid vehicle model but the vertical load is derived through a pot-hole simulation in ADAMS. Reverse braking is assumed to occur at such low speeds which means that such a load case may be neglected.

The vehicle is simulated to hit a pot hole at a speed of 100 kph, the hole is half a meter long and 50 mm deep. The resulting vertical load in the front tire is approximately 2800 N, see Figure 6.4. The flat valley/elevation represents the load transfer when accelerating up to 100 kph and then decelerating to standstill.

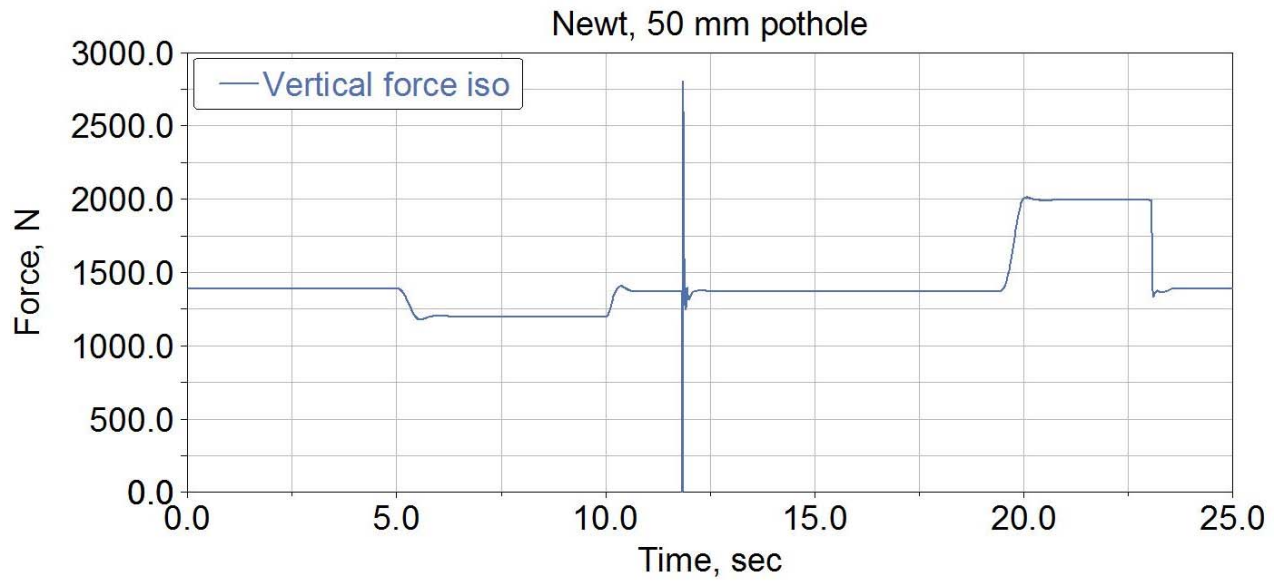


Figure 6.4. Pothole simulation, the graph displays the front wheel vertical force as the vehicle travels along the road. The sharp spike represents when the wheel hits the pothole at 100 kph.

7 VALIDATING THE MODELS

The different validation methods of the analytical results and the ADAMS model are presented here.

When validating the models the results from the dynamic simulations performed in ADAMS are compared to the results acquired from the Matlab calculations.

Since a delimitation is to disregard detailed tire modeling the ideal brake model is not validated in ADAMS. The methodology of the ideal brake model have however been validated by comparison to a detailed multi-body simulation model developed at the department of Mechanical Engineering at the University of Padova (Cossalter, et al., 2004).

7.1 Longitudinal dynamics

The rigid vehicle model and the anti-dive analysis are directly correlated to the longitudinal dynamics of the vehicle. They are validated with a straight line simulation featuring a velocity profile including acceleration, constant speed and deceleration.

7.1.1 Rigid vehicle model

Three cases calculated from the rigid vehicle model, acceleration, constant speed and deceleration from that speed are compared to ADAMS results. By driving at constant speed for approximately 10 s, the velocity profile displayed in Figure 7.1 is acquired with Matlab.

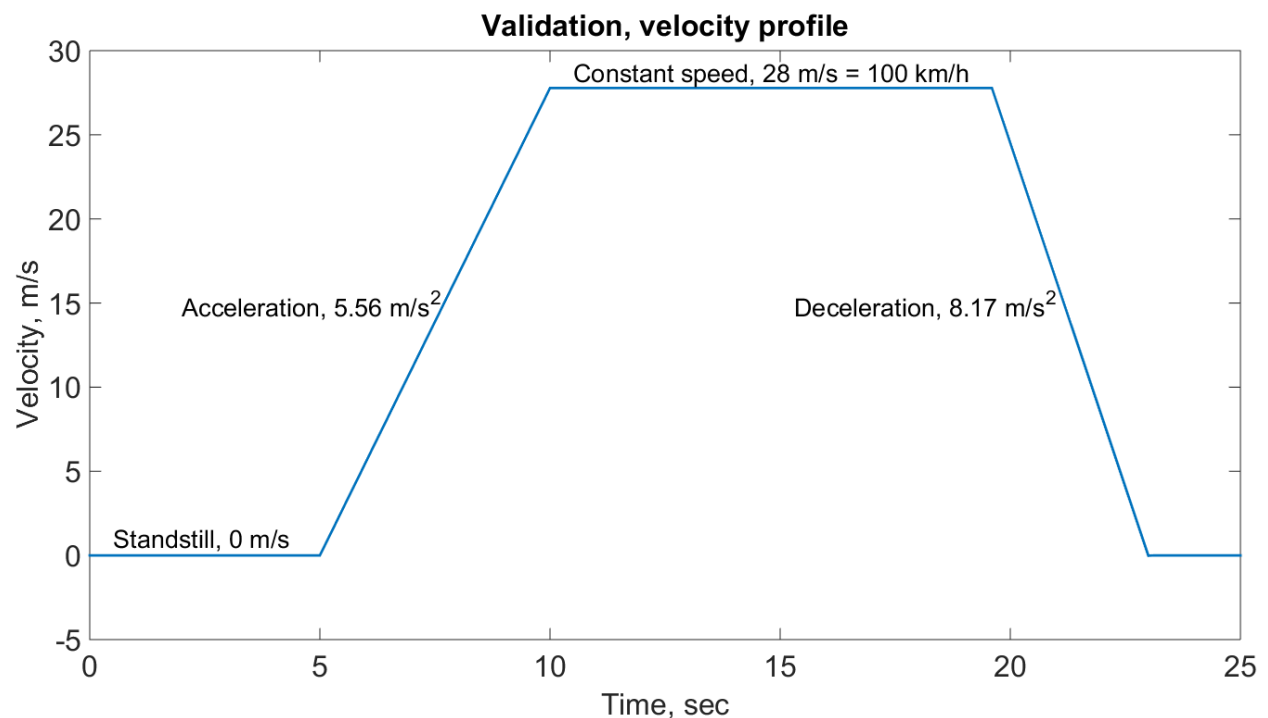


Figure 7.1. The velocity profile for the straight line simulation calculated in Matlab with the rigid vehicle model.

The wheel torques calculated by the rigid vehicle model are applied to the wheels in the ADAMS model. To avoid unwanted transient effects due to discontinuities in the time steps the torques are ramped when turned on/off at the specified time intervals. The resulting velocity profile generated by the ADAMS simulation is shown in Figure 7.2.

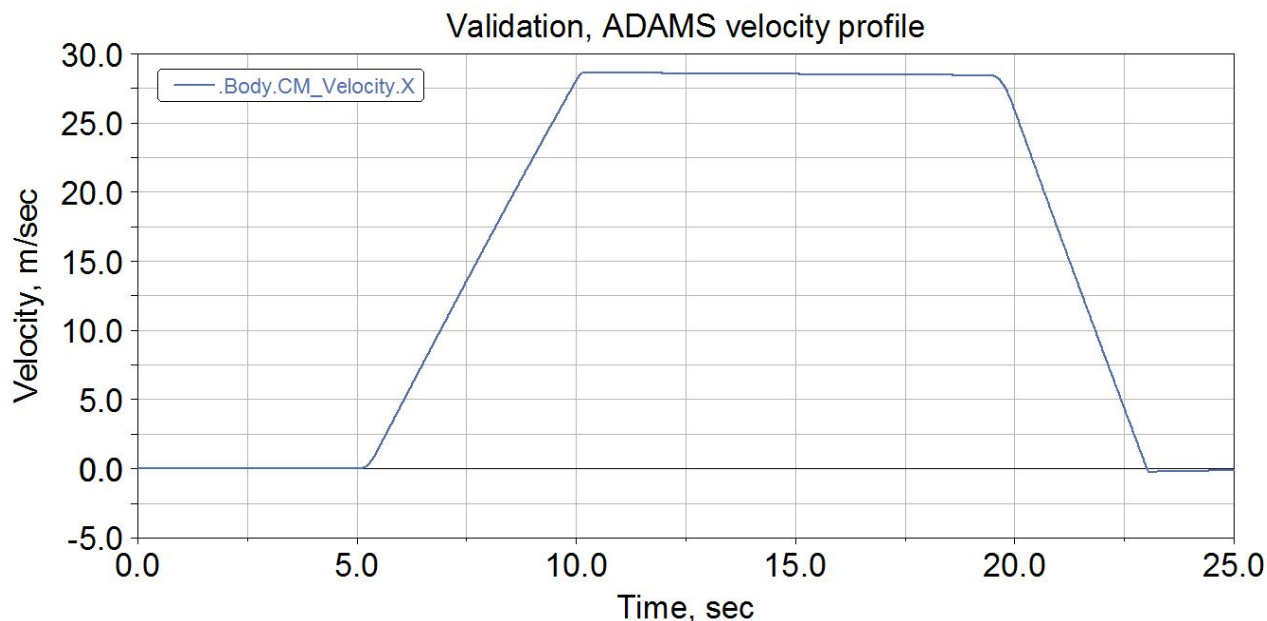


Figure 7.2. The ADAMS simulated straight line velocity profile.

The maximum speed the vehicle reaches in the ADAMS model is approximately 28 m/s , the same as in Matlab. Besides the maximum speed the two velocity profiles are close to identical meaning that the analytical results conforms with the ADAMS simulation.

The second output to review and compare are the vertical loads in the front and rear tire. The plot in Figure 7.3 presents how the loads change during the full maneuver due to load transfer.

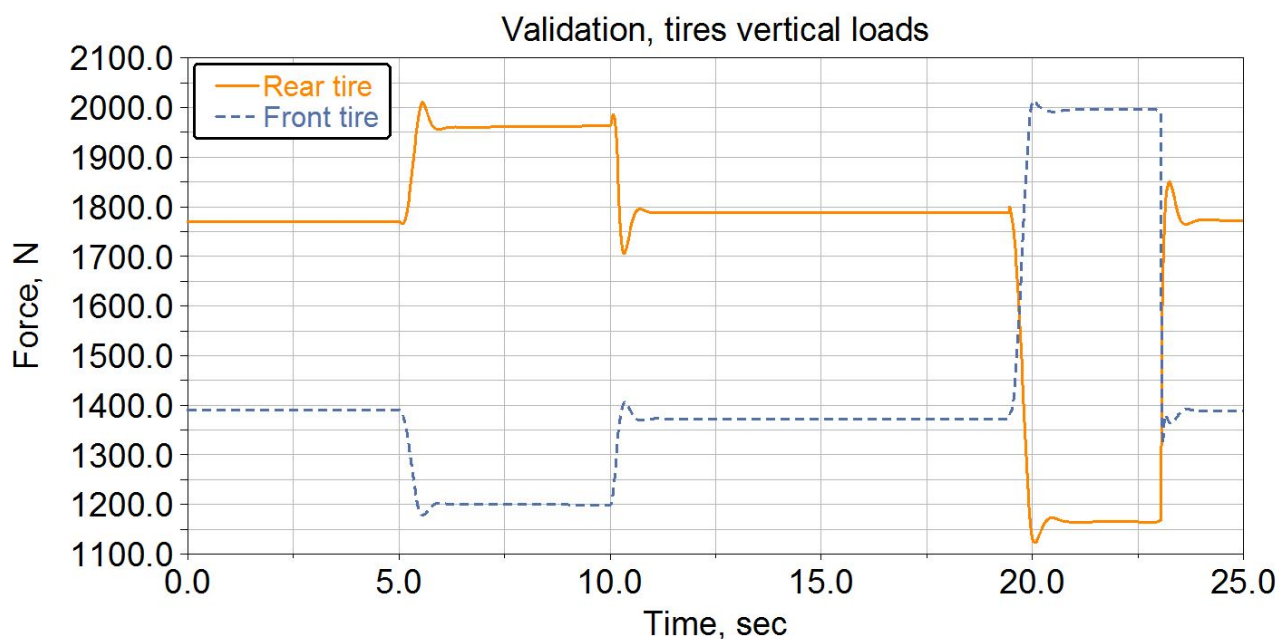


Figure 7.3. Vertical loads in the front and rear tire during the straight line simulation.

The small peaks in the graph are ignored and the constant force values at the flat section in the elevations or valleys are considered the dynamic load in the tires. The loads are extracted from the curves and compiled in Table 7.1.

Table 7.1. The resulting vertical loads in the tires from both models.

Case	Tire	Analytical, N_{w1} [N]	ADAMS, N_{w2} [N]	Diff., $ N_{w1}-N_{w2} $ [N]
Standstill	Front	1389	1389	0
	Rear	1770	1770	
Acceleration	Front	958	1198	240
	Rear	2201	1961	
Constant speed	Front	1355	1372	17
	Rear	1804	1787	
Deceleration	Front	1974	1995	21
	Rear	1185	1164	

Although the ADAMS model differs from the analytical output in the acceleration phase the nearly identical values and velocity profile endorse that the models are validated.

7.1.2 Anti-dive analysis

With the near constant high percentage anti-dive ratio the load transfer is rerouted to bypass the springs keeping them from compressing and pitching the vehicle. To evaluate the effects of the anti-dive geometry in the ADAMS model the force in the suspension springs are analyzed. Why the force is analyzed instead of spring compression is because with extremely stiff springs there would be a very small spring deformation though the force stays the same. Looking at the graph of the total front spring force over time in Figure 7.4 it can be established that a small change in force do take place.

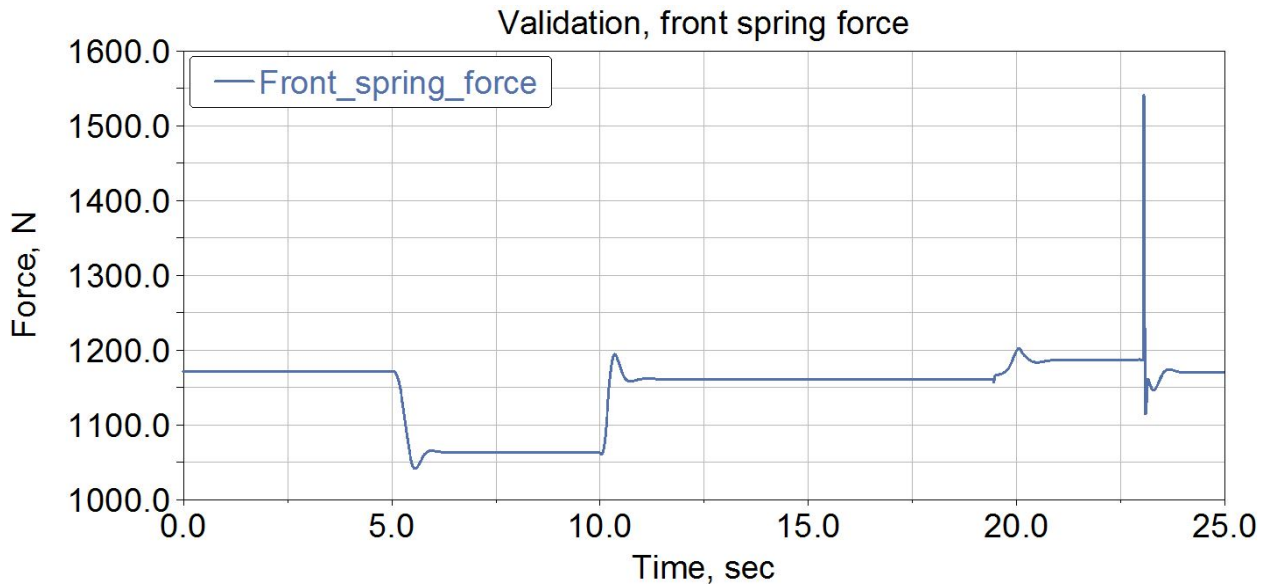


Figure 7.4. Front spring force during the straight line simulation, the sharp peak at around 23 sec is assumed to be a mathematical anomaly and is therefore neglected.

Since a small portion of the dynamic load passes through the springs during the entire maneuver it is expected that the spring force graph resembles the appearance of the front tire vertical load graph, though scaled down. Since the model takes the drag force into consideration there is some aerodynamic load transfer which reaches maximum at top speed. However when comparing the flat standstill part (0-5 sec) of the curve to the flat constant speed part (approx. 11-19.5 sec) it is concluded that this load transfer is relatively small.

If the small peaks are neglected the first flat valley of the curve reveal a drop to a constant force during acceleration. By also neglecting the sharp discrepancy at the end of the elevation portion of the curve, a constant force is once more extracted when decelerating.

Subtracting the equilibrium spring force from the dynamic values acquired from the curve a spring force deviation, F_d , is calculated. In Table 7.2 the magnitude of this deviation is presented together with its total fraction of the load transfer giving a measure of dynamic load that pass through the front springs.

Table 7.2. Comparison of resulting spring force in relation to load transfer.

Case	Deviation from equilibrium, $ F_d $ [N]	ADAMS Load transfer, ΔN_{w2} [N]	Fraction of load transfer, $F_d / \Delta N_{w2}$
Acceleration	109	191	57 %
Deceleration	16	606	2.6 %

To investigate the actual pitching behavior of the vehicle a measure that provides the pitch angle of the vehicle is created in ADAMS. Figure 7.5 shows this angle plotted during the straight line simulation.

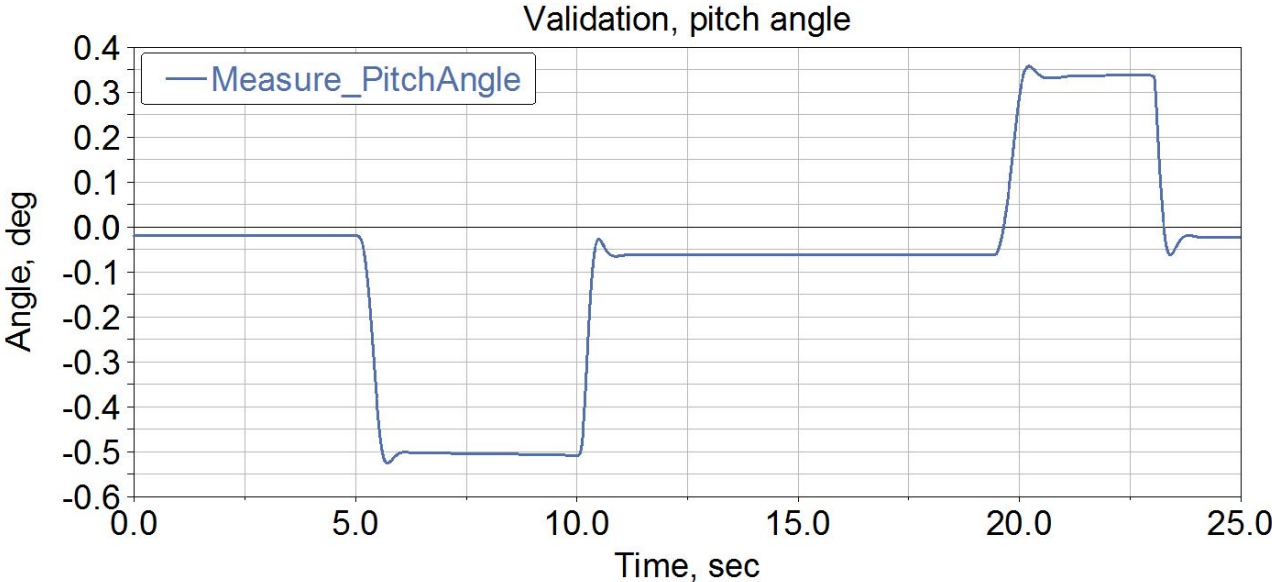


Figure 7.5. The pitch angle of the vehicle spans from approximately -0.5° to 0.35° .

The measure shows that the actual pitching of the vehicle is so small that the total range of response is below 1° , which would probably not even be noticeable to the driver.

7.2 Transient suspension

The transient behavior in the suspension cannot be validated by comparing the results from the half vehicle model to the ADAMS MBS model. The modeling level of detail differs immensely for these two models. For instance, the transient half vehicle model neglects the effect of the rear suspension and it assumes a vertical contact in the tire contact patch.

The pre-defined two dimensional road profile in ADAMS called *sine_sweep* is used to simulate a sinusoidal road. The *sine_sweep* road features a range of decreasing wavelengths specified by the road property file. The mathematical expression describing the profile has also been implemented in Matlab to provide the same excitation input for both models. The output from the transient half vehicle model during the *sine_sweep* simulation is displayed in Figure 7.6.

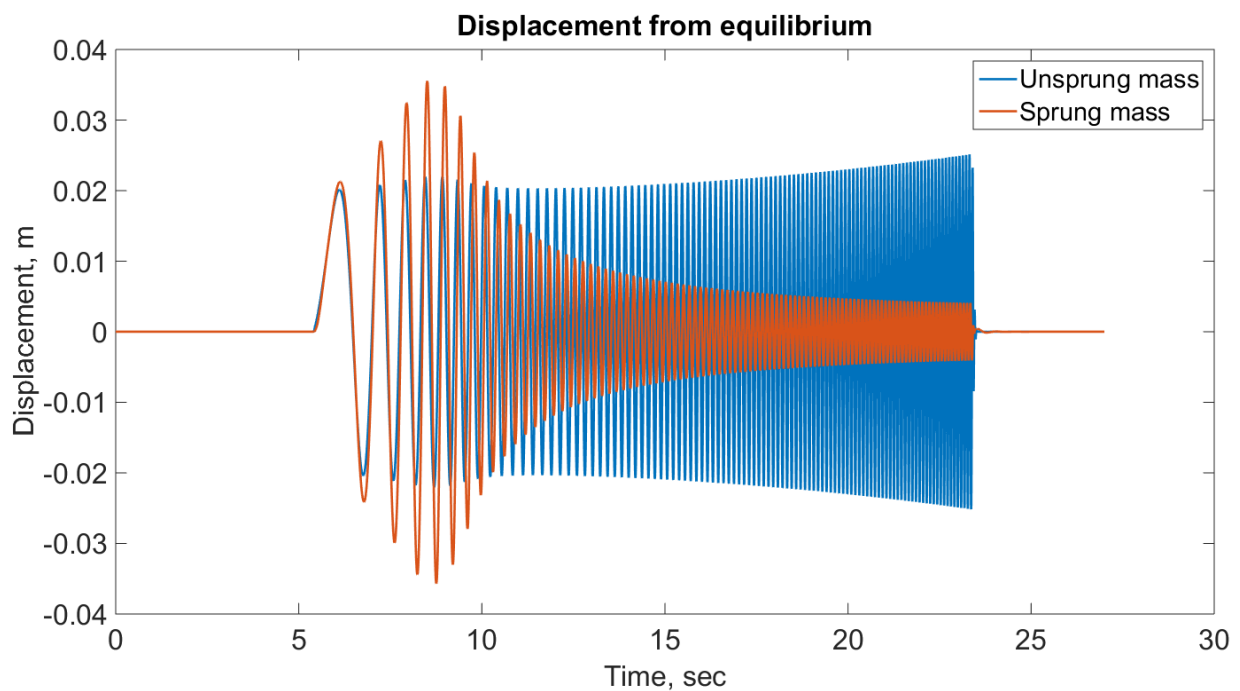


Figure 7.6. The sprung and unsprung mass displacement from equilibrium in the *sine_sweep* simulation from the transient Matlab model.

When comparing the result to the ADAMS simulation, seen in Figure 7.7, it is established that the curves share a minor resemblance. The differences are however too extensive for any validation. In an effort to try and couple these models to each other the transient vehicle model could possibly be refined by implementing a second unsprung system connected to the sprung mass. Such addition would better take into account the effect of the rear wheel.

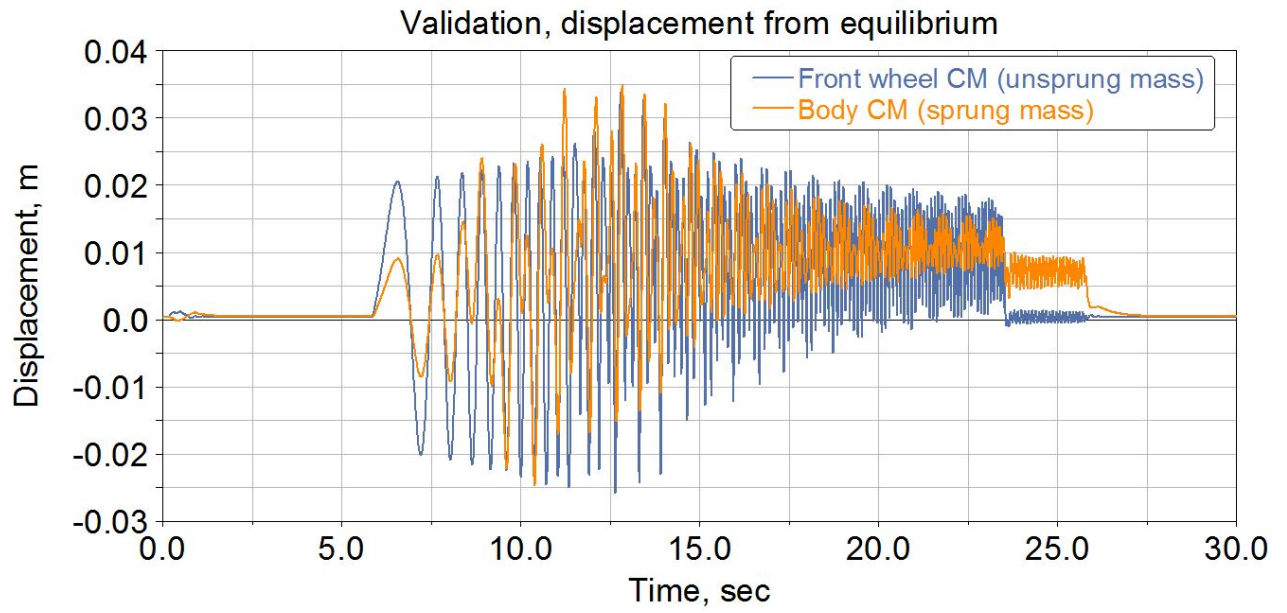


Figure 7.7. Sine_sweep simulation performed in ADAMS with the sprung and front unsprung centre of mass markers vertical displacement plotted.

8 DETAILED CONCEPT DESIGN

The detailed conceptual design is comprised by a Solid Edge CAD model, the different parts and subsystems are presented here together with the result from their structural analysis.

When examining the different frameless brushless motors from ThinGap, Applimotion and AlliedMotion there are models at an acceptable weight which are able to meet the continuous torque requirements at constant speed. Even though an electric motor has the ability to be overloaded for short periods of time the extensive torque needed for the *acceleration* and *inclined ramp* sequences are close to the demagnetization torque of the motors (Allied Motion, 2015). Not only will demagnetization completely destroy the motors but the generated heat in the motor may melt the wire isolation film and cause short circuit.

When in contact with BEVI, (Nyström, 2014) they approximated an electric motor weight of 60 kg, if it were to cope with these specifications. One of the targets for Newt is lightweight design and such a motor is therefore not acceptable. By incorporating a gearbox the torque requirements could however be met while still maintaining a low weight.

With the uncertainty in available peak torque, this being a conceptual design and the influence of surrounding components in terms of design and space no specific motor model is chosen. Instead a representative motor is modeled in the CAD software based on dimensions of suitable motors. When going into further iterations of the design a particular motor should be chosen and effected components revised to conform with the design.

Structural integrity is assured using finite element method (FEM) in Ansys Workbench. The structural finite element analysis (FEA) is however completely disregarded for some parts where the design uncertainties will have too much impact on the loading conditions.

The high strength aluminum alloy called Alumecc 89 is the proposed material selection for the metal parts. The mechanical properties for the material is retrieved in datasheets from Uddeholm material supplier. The yield limit of the material varies slightly depending on the type of billet, why the values used in the structural analysis conforms to the required billet of the part (Uddeholm, 2011). The factor of safety (FOS) is calculated with the ratio of the resulting stress to yield stress for that particular part.

8.1 Main assembly

The conceptual design of the front suspension is presented in Figure 8.1 and Figure 8.2. The springs and shock absorbers which are visible in the assembly are arbitrary placed for display purposes. Their positioning is going to be dependent on the obtainable springs and installation ratio, interface to the vehicle chassis and the deployment mechanism which is still to be developed.

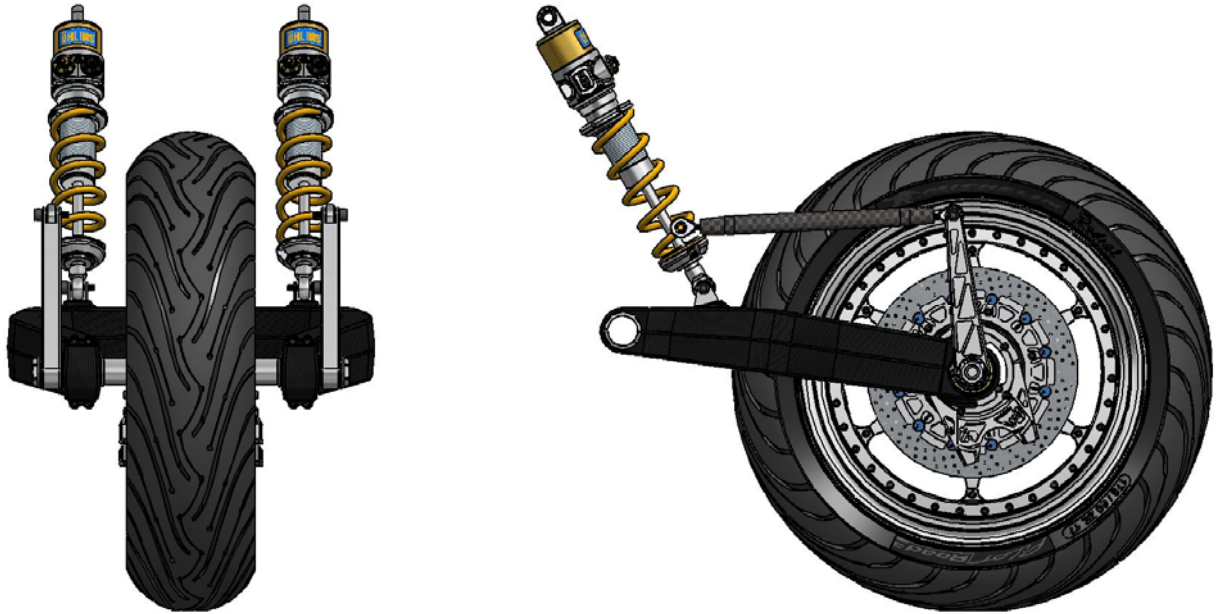


Figure 8.1. The front view (left) and side view (right) of the front suspension conceptual design, the springs and dampeners are arbitrary placed to serve as functional demonstrators.

The analytical models calculated the suspension HP for a two dimensional linkage in the global coordinate system xz -plane. The y -coordinates that are featured in the following models are derived based on the required space for steering angles and assumptions for chassis attachments. For instance, to avoid an unnecessary long transverse axis the swing arm is curved in order to allow wheel steering motion, see the top view in Figure 8.2. With design iterations a further developed chassis interface may determine revised y -coordinates for the suspension.

According to the thesis delimitations the steering mechanism for the front wheel is not modeled and therefore not included in the main assembly.

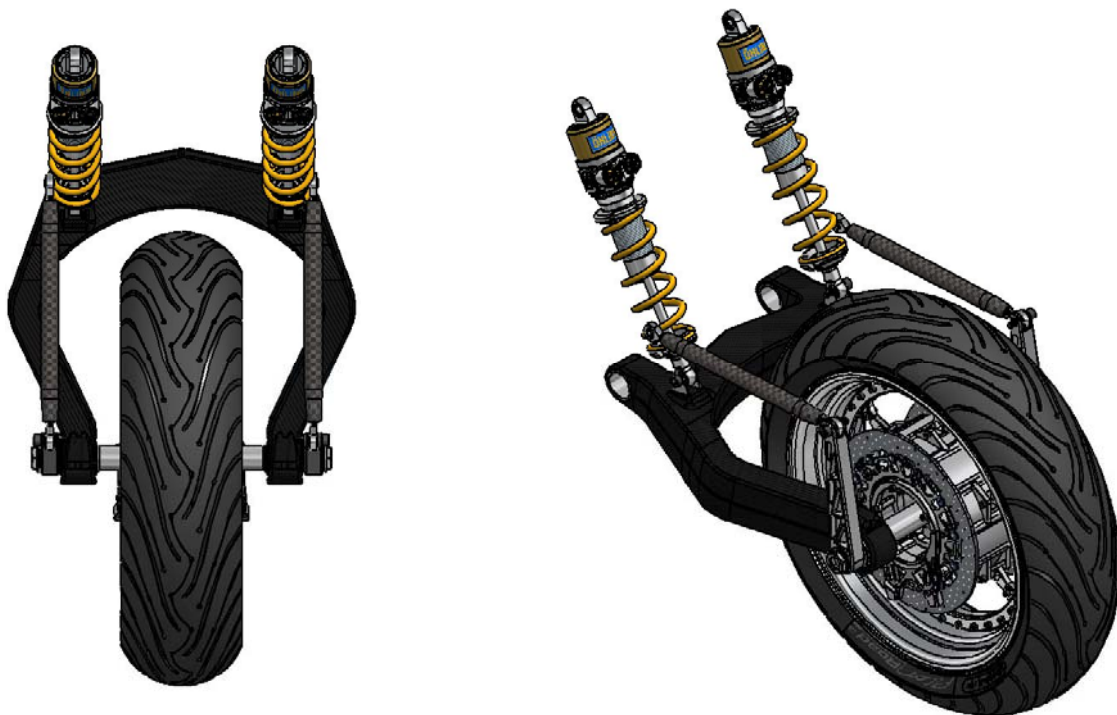


Figure 8.2. The top view (left) and isometric view (right).

8.2 Front wheel

The majority of parts in the conceptual design are located in the front unsprung assembly, see Figure 8.3. To better facilitate manufacturing and assembly some components in the front wheel have been split into multiple parts and reassembled with fasteners. More detailed illustrations and descriptions of the separate sub-assemblies and individual parts are presented in the sections below.

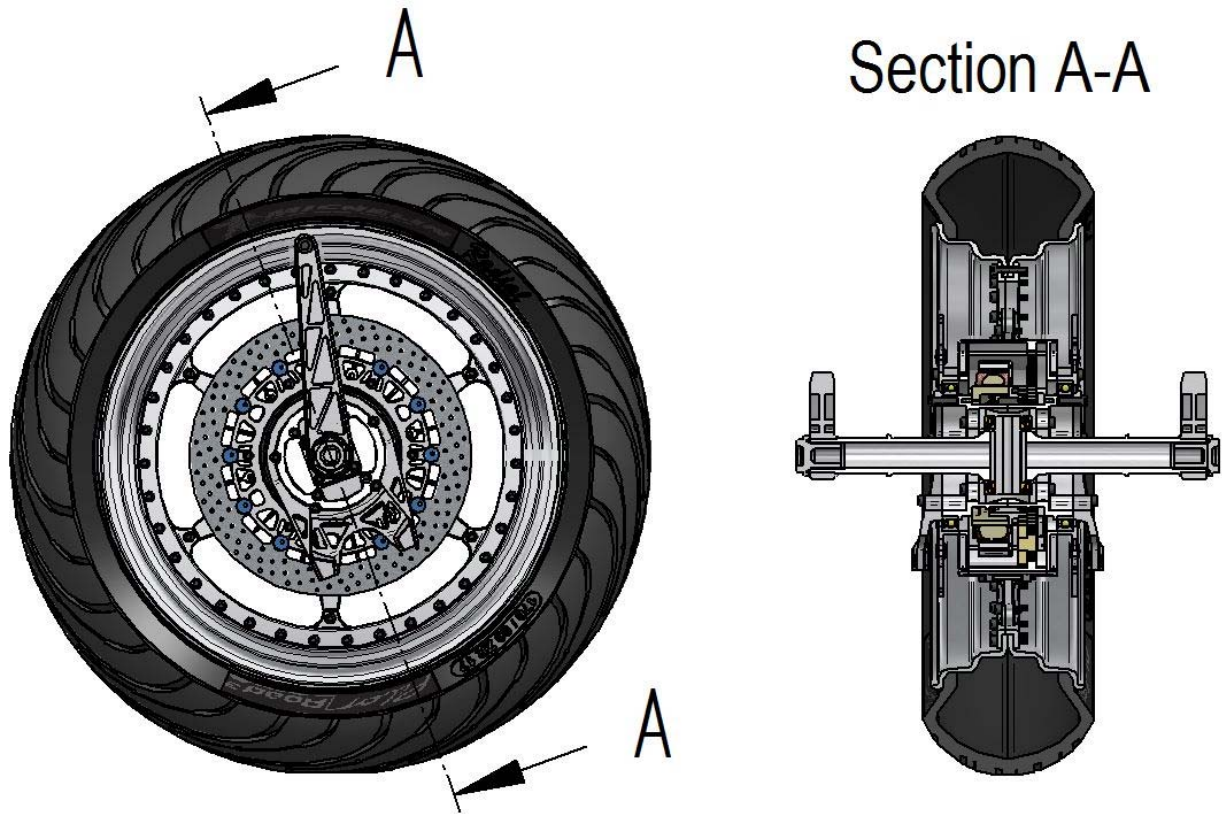


Figure 8.3. The front wheel assembled with the axle-hub, front motor and tire and rim sub-assemblies.

Being a conceptual design, the bearings and bearing arrangements in the assembly model are chosen based on assumptions of the loading conditions and the available space. With more extensive development of the electric motor and dimensioning loads from the ADAMS model the design of the bearing arrangements can be finalized.

8.2.1 Axle-Hub

The main functionality of the axle-hub sub-assembly is to position the various bearing arrangements and braking components while coping with the stresses generated by operating loads.

8.2.1.1 General design

A closer look at the design and arrangement of the axle-hub sub-assembly is visible in the section view in Figure 8.4, the motor cover and torque arms have also been included. The section view is perpendicular to the steering axis inclination angle as illustrated in Figure 8.3 which is why the torque arms are cropped in the figure.

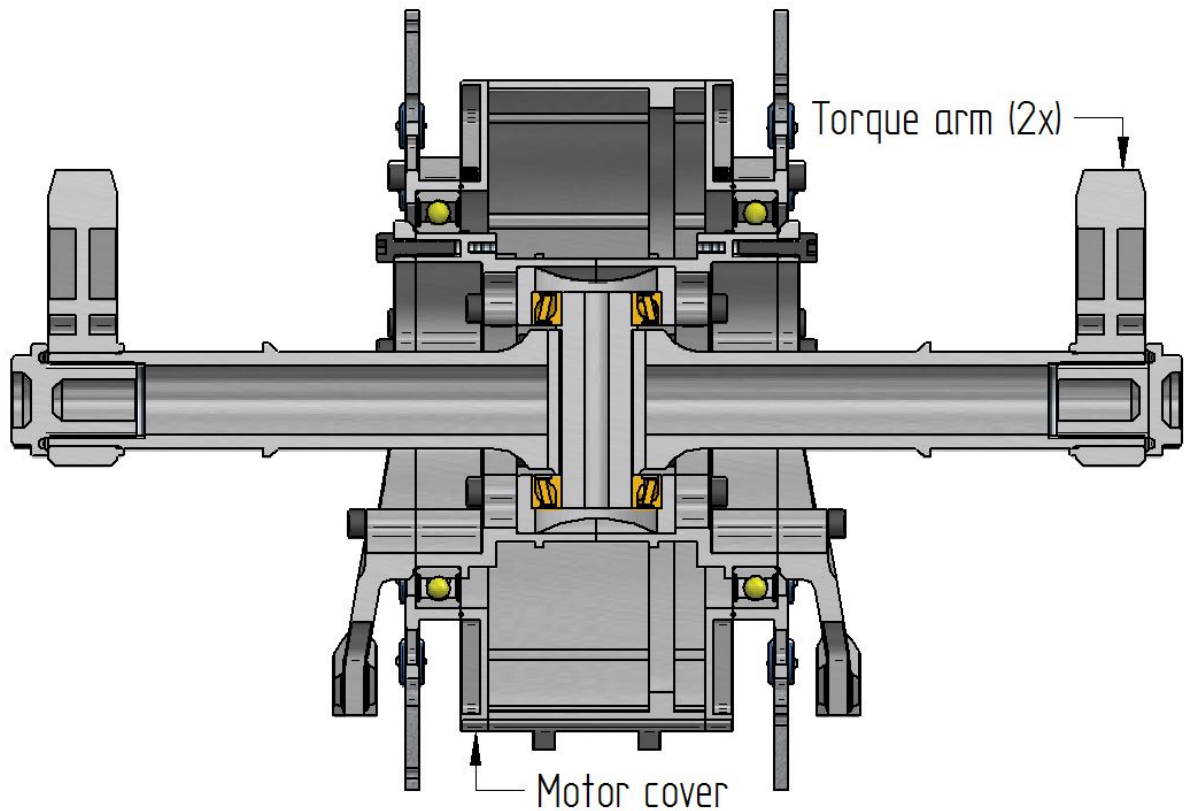


Figure 8.4. The axle-hub assembly supplemented with the torque arms, motor cover and swing arm bearings.

Figure 8.5 illustrates the axle components of the axle-hub assembly, with the transverse wheel axle as the main component that connect the front wheel to the swing arm. The axle is divided into two parts to better facilitate assembly/disassembly and the two identical pieces are connected to the axle center hub by bolts. Splines are added to the ends of the transverse axle to provide tangential locking for the torque arms. Two custom bolts named transverse axle bolt in Figure 8.5 are used to position the torque arms axially.

Figure 8.5 also displays the steering axle modeled as a standalone part from the axle center hub. Rotation of the steering axle inside the center hub is constrained either with splines or a key. The reason for separating the parts is mainly to simplify manufacturing of the axle as it will require stricter tolerances due to the bearing raceways.

The bearings mounted to the steering axle must be able to transmit both axial and radial loads as both lateral and vertical forces will stress the bearings in these directions. Visible in Figure 8.4, the space around the steering axle is somewhat confined, why angular contact ball bearings are chosen due to their lesser width than for instance tapered roller bearings. A common property for both tapered roller and angular contact bearings is that they require initial preloading. Preloading of the steering axis bearings is however not included in this assembly but may easily be incorporated either with spring washers or adjustment nuts.

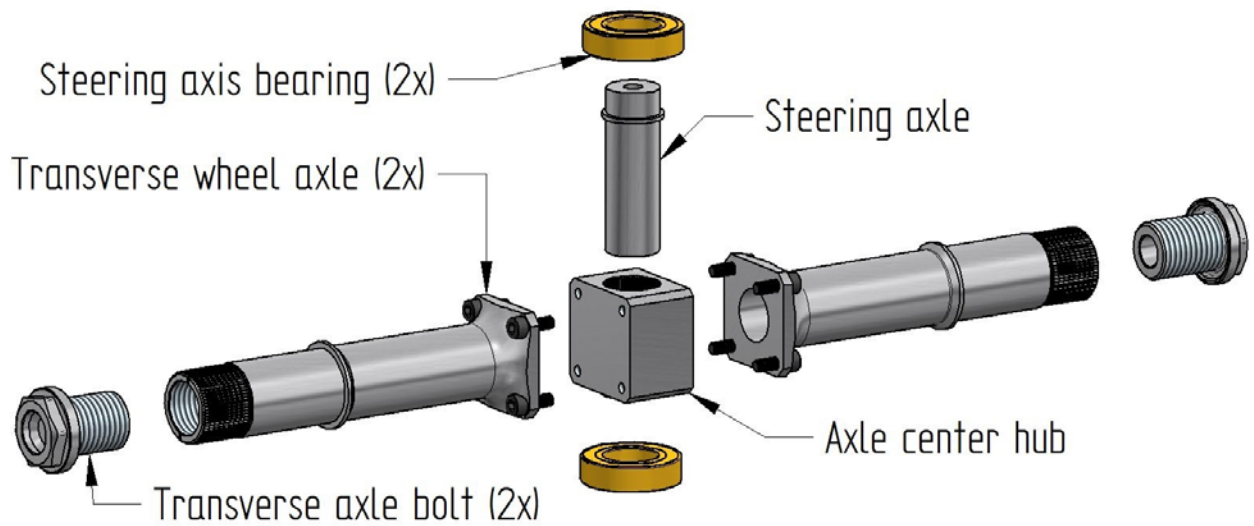


Figure 8.5. Exploded view of the axle assembly

The hub and brake components of the axle-hub sub-assembly are presented in the exploded view in Figure 8.6. To allow both assembly and manufacture the wheel hub is also required to be split into two parts. The two pieces of the wheel hub are then joined with bolts into the steering axle hub. The raceways for the deep groove ball wheel bearings are located at each end of the assembled wheel hub.

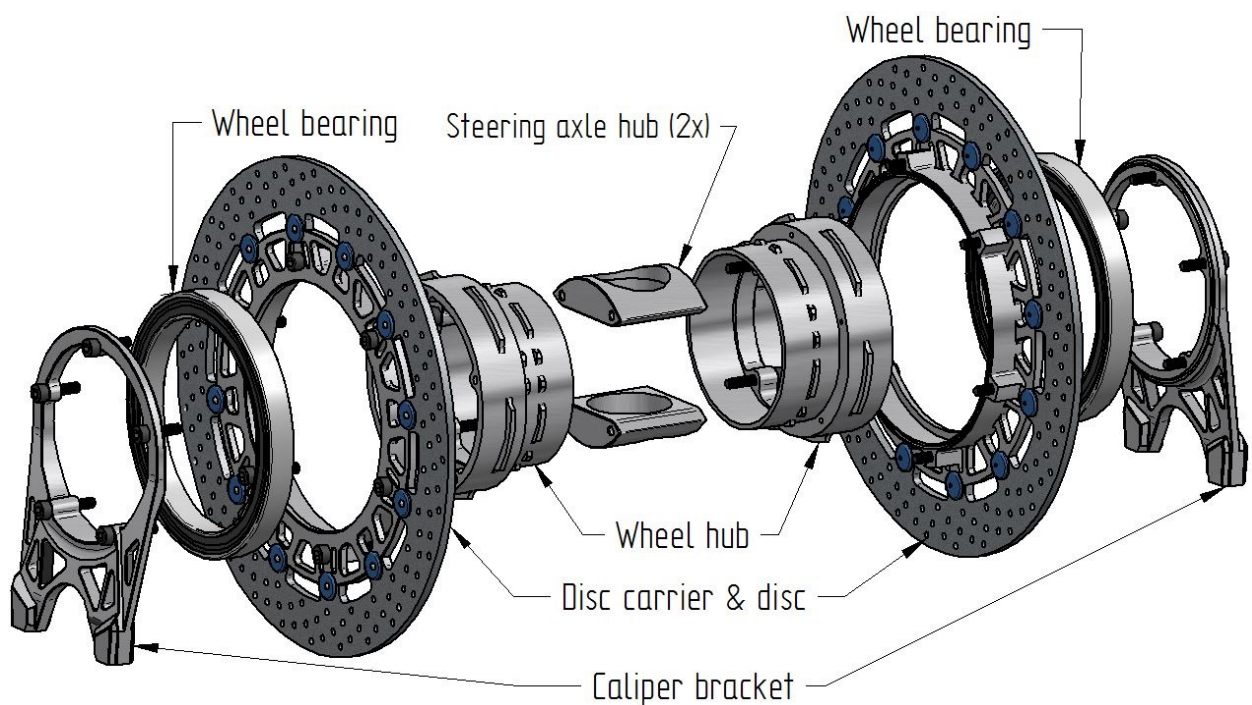


Figure 8.6. Exploded view of the hub assembly.

The disc carriers are designed to fulfill two functions, carrying the brake discs and withstand the high torque load. They are also used to provide the housing bore for the wheel bearings as displayed in Figure 8.6. The caliper brackets feature a bolted connection to the ends of the wheel hub.

The brake caliper (excluded from the model) and brake disc will most likely be ordered from a retailer, hence a design revision of the disc carriers and caliper brackets is needed when those components are selected.

8.2.1.2 Structural analysis

The structural analyses are performed on the individual parts in Ansys Workbench. In some cases the geometry has been simplified by removing topology e.g. splines. The complete setup and resulting stress and deformation fields for all the different models are presented in APPENDIX III.

When utilizing the FEM for strength analysis, mathematical stress concentrations are a frequently encountered problem found typically at the edges of boundary conditions or places where the model has been meshed poorly. As these concentrated stresses are generated by modeling deficiency they may be neglected if it is ensured that the stress field has converged in the rest of the model. Stress convergence analysis is applied in all FEA with the limit for convergence set to 10 %. When stress concentrations emerge that causes the solution to diverge the stress in that particular area is neglected. The result from the structural analysis are presented in Table 8.1.

Table 8.1. Results from the structural analysis

Part	Material	Yield strength	Max stress	Max deformation	FOS
Unit	-	MPa	MPa	mm	-
Steering axle	Alumec 89	630	120	0.02	5.3
Transverse axle	Alumec 89	630	152	0.6	4.1
Wheel hub	Alumec 89	620	68.5	0.02	9
Disc carrier	Alumec 89	610	27	0.006	23
Caliper bracket	Alumec 89	610	239	0.5	2.6

8.2.2 Front motor

Of all the sub-assemblies the front motor assembly is considered as the most conceptual and the inherent components are modeled more abstract than the rest. The reason is that the entire sub-assembly is highly dependent on the design of the electric motor. Since the actual size and performance of the motor is undetermined the parts are sufficiently modeled to an extent where the functionality can be ensured.

The motor used as a reference for the modeled representative motor is manufactured by AlliedMotion with model number MF02100025 with properties presented in Table 8.2

Table 8.2. Mechanical properties for the MF02100025 AlliedMotion motor.

Model no.	Inner diameter	Outer diameter, motor	Outer diameter, mounting flange	Continuous torque
MF02100025	150 mm	205 mm	230 mm	21.7 Nm

The AlliedMotion motor has the stator as the outer ring and the rotor as the inner ring, this is more suited for e.g. direct drive on shafts which is these motors primary application (Allied Motion, 2015). As all three motor companies, AlliedMotion, ThinGap and Applimotion states that they provide custom motor solutions together with their customer the modeled representative motor feature a stator as the internal ring to facilitate attachment to the hub (Allied Motion, 2015), (Applimotion, Inc, 2015) and (ThinGap, 2014).

8.2.2.1 General design

The sub-assembly, seen in Figure 8.7, contains the stator, rotor, rotor carrier with rotor bearings, gear set and motor cover. With the rotor powering the planetary gear the motion is eventually transported to the outer ring gear which is fixed to the cover. The motor cover is then bolted to the wheel center thus forcing the wheel to rotate with the speed of the cover.

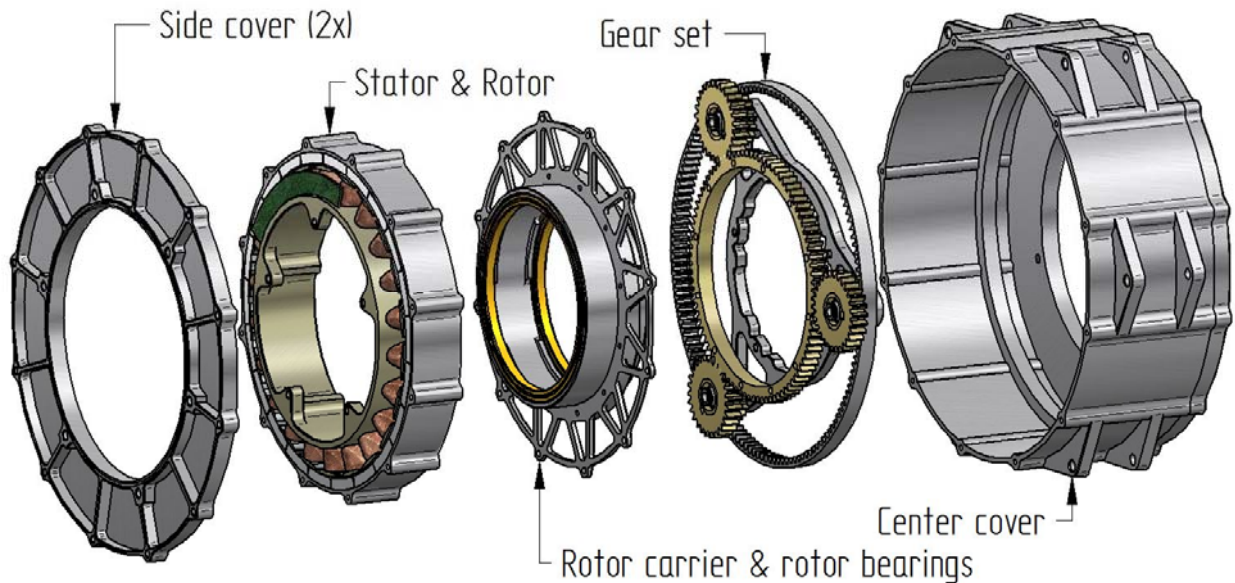


Figure 8.7. The front hub motor sub-assembly.

The rotor bearings will not be subjected to any road induced forces since those loads will be routed through the wheel bearings. If straight cut gears are used there will be approximately no axial load in the rotor carrier. The limited space and the favorable loading conditions allows for thin section deep groove ball bearings to be utilized. The assembled motor is displayed in Figure 8.8.

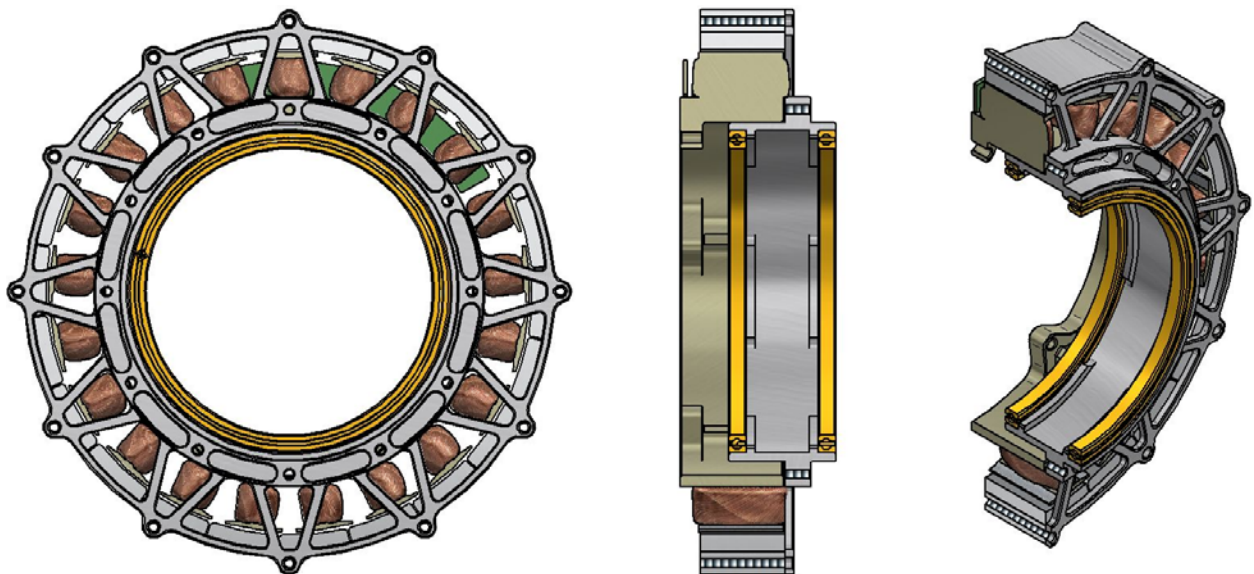


Figure 8.8. Stator, rotor, rotor carrier and rotor bearings.

The stationary component in the planetary gear is the planet carrier, its rotation is constrained through a bolted connection to the wheel hub, hence the planets are idle gears in the assembly. Bolts are also used to attach the sun gear to the rotor carrier making it the input gear, the final

ring gear is consequently the output gear. An outcome of having the planet carrier as the fixed component in the planetary gear is that the output rotation is reversed.

The different gears in the model are chosen entirely arbitrary since a gear ratio cannot be determined until the motor specifications are established. When finally proceeding into more detailed design of the electric motor the planetary gear may also be further developed e.g. determining the size, module and number gear teeth.

The bearing arrangements for the planet gears are excluded from this assembly and the entire planetary gear is shown in Figure 8.9. The large diametrical clearance required for the wheel hub in the center of the motor assembly has an impact on the design of the planetary gear. This free clearance causes the sun gear to be relatively large and as a consequence the gear ratio drops. By implementing a secondary gear stage the ratio may be increased and reach acceptable levels.

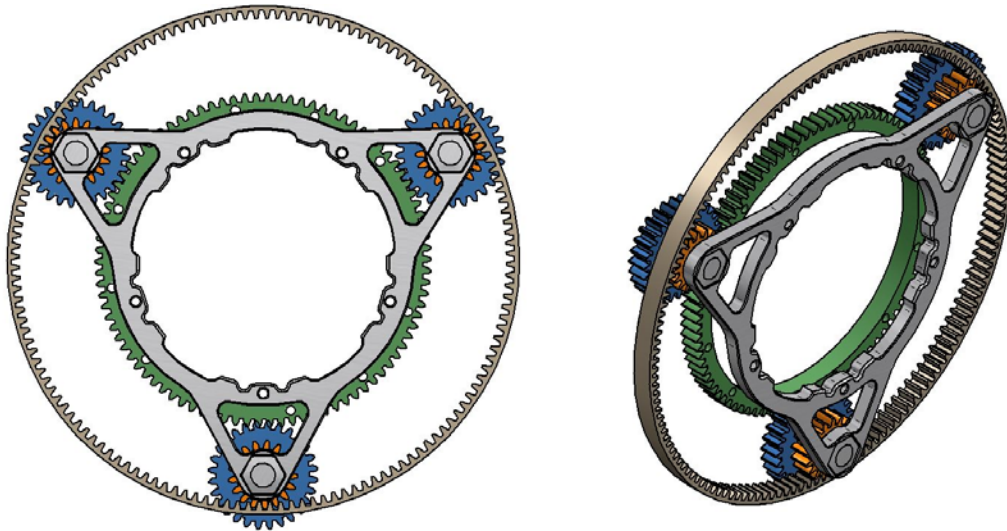


Figure 8.9. Color coded planetary gear. The blue planet gears are the first stage of engagement to the sun gear, they power the orange secondary set of gears which engages the ring gear.

The use of a geared motor will most likely require some sort of lubricant to keep it running smoothly. While not taken into consideration in the modeling of these parts, the rotor carrier is easily redesigned to cover the stator and rotor completely from one side thus shielding the electric motor from grease.

As it is important to shield the motor from internal lubricants it is equally important to keep out external contaminants why the motor must be sealed from dust but especially from water. It could be rain water during land mode operation but also during ascent/descent into displacement mode. In the transitory state from land to water or vice versa the front wheel may be partly or entirely submerged in lake/sea water. When continuing with the detailed design a required ingress protection (IP) rating should be established and an appropriate sealing solution determined. For the conceptual design the motor cover is sealed with rubber o-rings, see Figure 8.10.

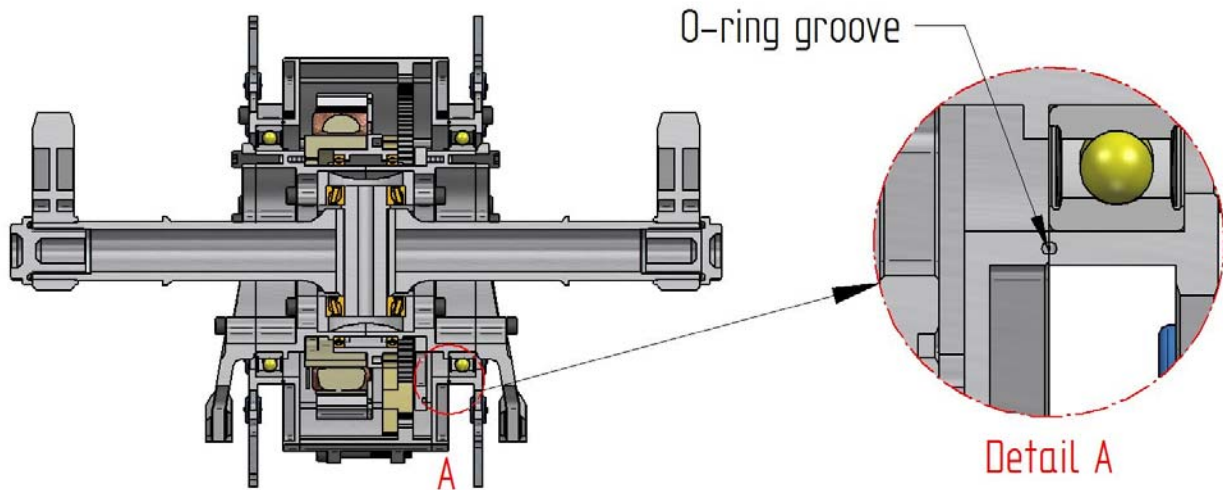


Figure 8.10. O-ring seal groove, one on each side of the motor cover.

8.2.2.2 Structural analysis

The level of abstraction due to the uncertainties in the design of the stator, rotor and planetary gear means that structural analysis for those parts is disregarded. The rotor carrier and motor cover are analyzed in the same manner as the axle-hub components and the results are presented in Table 8.3.

Table 8.3. The results from the structural analysis of the analyzed front motor components.

Part	Material	Yield limit	Max stress	Max deformation	FOS
Unit	-	MPa	MPa	mm	-
Rotor carrier	Alumec 89	610	41.8	0.018	14.6
Motor cover	Alumec 89	610	38.4	0.012	15.9

8.2.3 Tire, rims and wheel center

The intended tires for the vehicle specified in section 3.1 are the Michelin Pilot Road 3 in dimension 170/60 ZR 17 fitted to an aluminum split rim. A wheel center is designed to fit the rim and the interface of the motor cover see Figure 8.11.

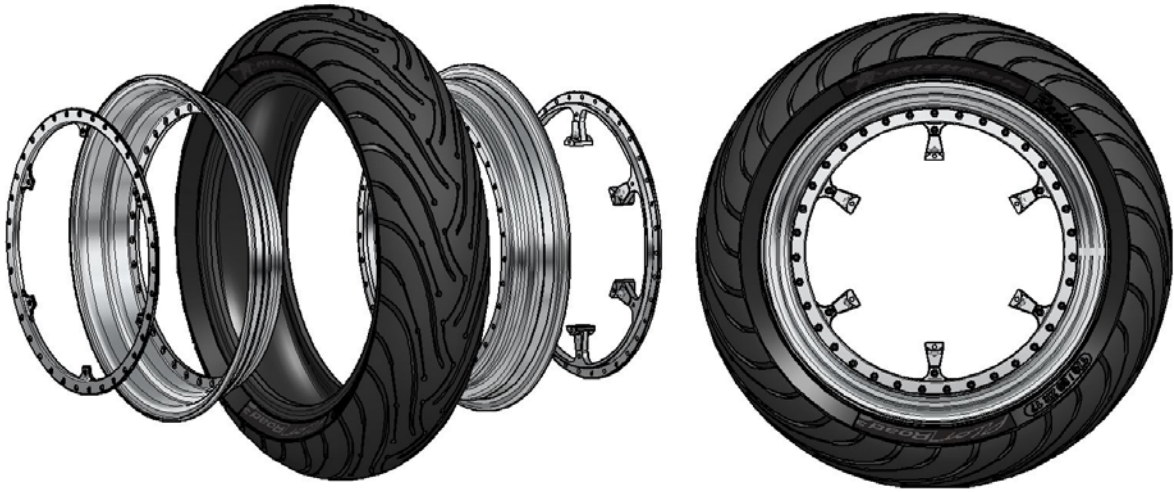


Figure 8.11. The tire, split rim and wheel center with backing plate

With the tire, rim and motor cover interface specified, the design of the wheel center is relatively constrained. By striving for a symmetrical design but still allowing disassembly the conceptual design feature a near symmetrical wheel center with a backing plate at the rim interface, see Figure 8.12.

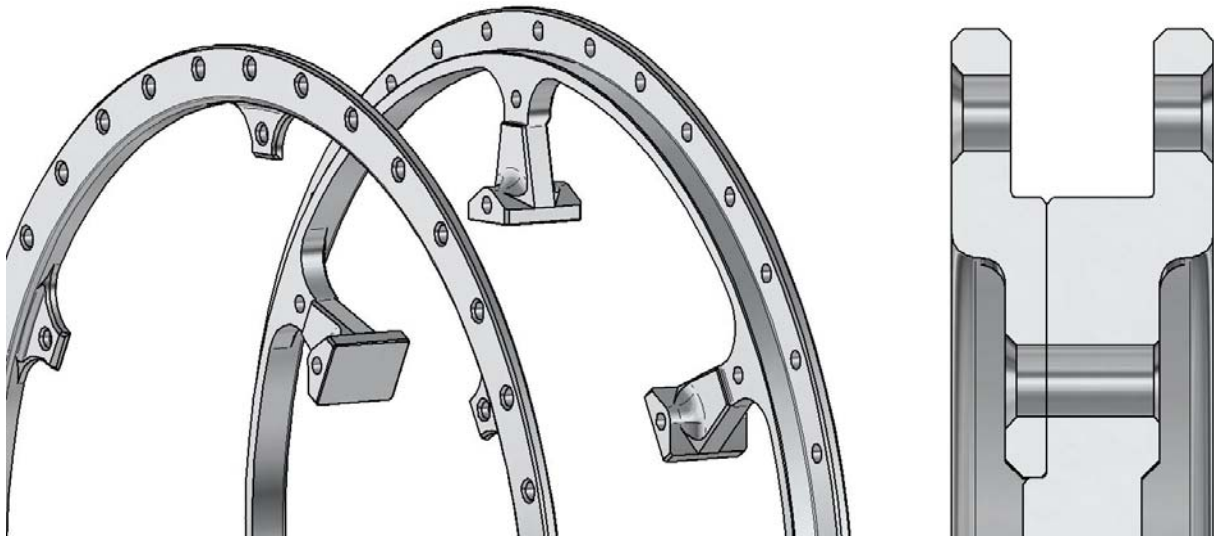


Figure 8.12. The wheel center is divided into two pieces, when bolted together it forms a symmetrical part attached to the rim.

8.2.3.1 Structural analysis

With the tire and rims being standard components purchased from a supplier the only part included in the structural analysis is the custom wheel center, see Table 8.4

Table 8.4. Structural analysis of the wheel center.

Part	Material	Yield limit	Max stress	Max deformation	FOS
Unit	-	MPa	MPa	mm	-
Wheel center	Alumec 89	610	195.7	0.14	3.1

8.3 Swing arm, torque struts and torque arms

With joints located at the suspension HP derived with the analytical models, the swing arm, torque struts and torque arms are the parts that up to this point have been known as the suspension linkages. The links are the parts which carries the wheel in jounce and rebound and transmits the forces from the wheel into the chassis. The conceptual design of the suspension links is displayed in Figure 8.13.



Figure 8.13. The suspension linkage, consisting of a swing arm, torque arms and torque struts. The torque arms are mounted to the transverse axle which is excluded from the figure why they appear to be floating in mid air.

8.3.1 Swing arm

The properties and geometry that the swing arm must fulfill makes it ideal to be manufactured from fiber composites. Using for example carbon fiber reinforced plastics (CFRP) as material for the swing arm may significantly reduce the weight of the component. The design, which is illustrated in Figure 8.14, is derived with this in mind since the shape of composite parts must take into account the restrictions in composite manufacturing.



Figure 8.14. The composite swing arm from different viewing angles.

The part has been modeled with draft angles towards the centerline to represent a composite swing arm molded in two pieces and adhesively bonded together. The bearing seats and shock absorber attachments located in the swing arm are pre-manufactured from aluminum and bonded to the composite piece.

The swing arm is one of the parts where the placement of the suspension shock absorber will have a great impact on the structural analysis of the part. In this model that interface is arbitrarily placed and as a consequence there is no structural analysis conducted. If a single shell composite proves to be insufficiently stiff then composite sandwich construction should be considered. Implementing a sandwich core would be rather straight forward since the design features long and wide surfaces with a small curvature, ideal for sandwich design.

8.3.2 Torque struts

Besides being used as a guide for kinematic motion, the function of the torque strut during operation is to transmit the forces generated by braking from the front suspension into the chassis. During forward braking the brake torque generates pull forces in the torque strut causing tensile stress. Since rotational motion is unconstrained in the joints of the struts the arising forces due to wheel travel e.g. bumps is nearly zero. The uniform loading conditions calls for a rather uncomplicated part, why the design of the torque strut is a tube fitted with rod ends (rose joints) at the ends.

The torque strut is another part very well suited for composite material, e.g. CFRP. The presence of a loading condition where the part is mainly exposed to tensile stress makes it possible to tailor a composite tube with a high ratio of unidirectional fibers and thus reducing weight. In order to fit rod ends to the tube some threaded metal inserts need to be bonded to the composite. With the described loading condition the rod ends want to pull out of the tube, why the tube and inserts are tapered at the ends to better accommodate the pull out force. Figure 8.15 shows the torque strut from the outside and in a section view to display the tapered threaded inserts.



Figure 8.15. The composite torque strut, the threaded inserts are tapered and adhesively bonded to the tube.

Deciding on the specific fiber reinforcement and matrix for the composite is beyond the level of development required for the conceptual design. No structural analysis is therefore conducted for the composite torque struts.

8.3.3 Torque arms

The torque arm is designed, like most of the other components, to be machined out of high strength aluminum, see Figure 8.16. As previously mentioned the two identical parts are fitted to the transverse axle by means of splines and located axially with custom bolts into the axle. To ensure that the torque arm is mounted on the transverse axle in the intended position a small line marking is created on both parts. Thus when the markings line up, the torque arm is at the correct angle.

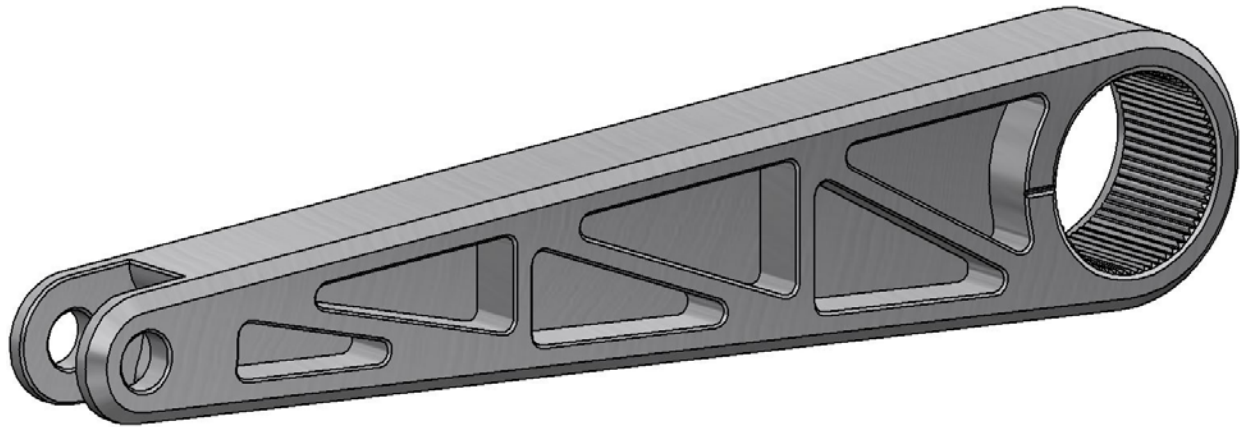


Figure 8.16. The torque arm with triangulated stiffeners, spline interface and line up marking.

With no structural analysis for the composite parts the torque arm is the only part in this sub-assembly which is analyzed in FEM. The resulting stress, deformation and FOS are presented in Table 8.5.

Table 8.5. Structural analysis of the torque arm.

Part	Material	Yield limit	Max stress	Max deformation	FOS
Unit	-	MPa	MPa	mm	-
Torque arm	Alumec 89	610	499.7	1.3	1.2

When comparing the stress in the torque arm to the stress arising in the other components it is quite high and as a consequence the FOS low. This high stress gives a reason to examine the stress field more thoroughly and identify the reason for such a spike.

By looking at the overall stress field it can be concluded that the high stresses are located at the top of the torque arm, see Figure 8.17.

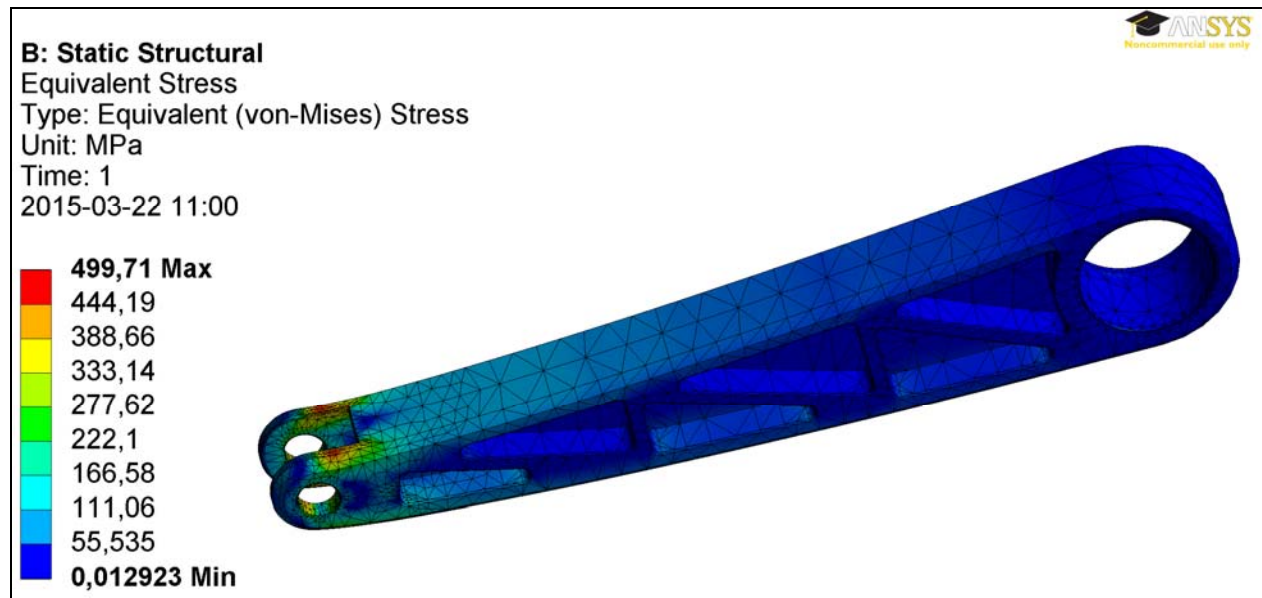


Figure 8.17. The overall stress field of the torque arm with the crucial stresses at the top hole (to the left).

At first glance it seems that the two red hot spots at the edges of the top hole is the area of maximum stress. When refining the mesh in this region and recalculating the results it is however apparent that a stress concentration due to the sharp edge is generated, see Figure 8.18.

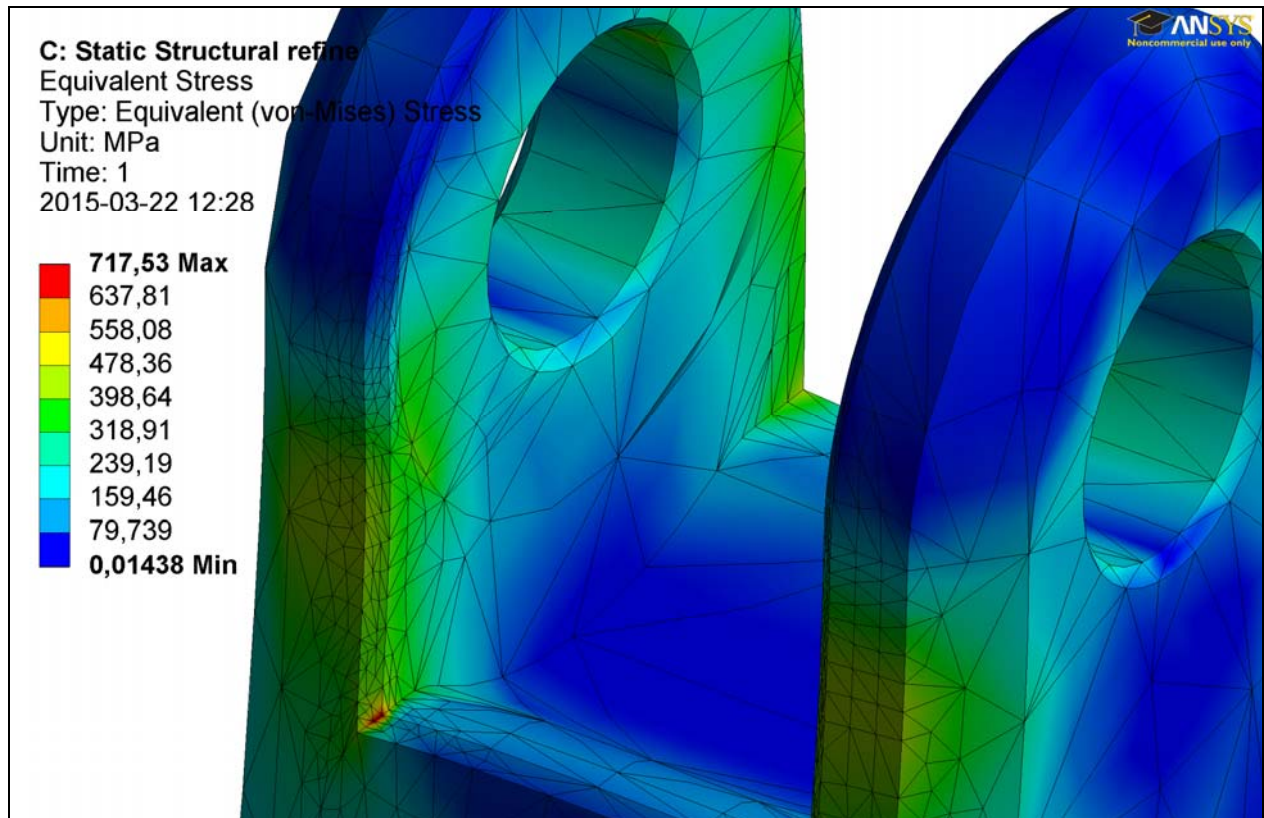


Figure 8.18. Close up of the area of maximum stress, revealing a stress concentration at the edge.

The high stress in this point can thus be ignored as the model neglects small local plasticity and the effect of small edge radii due to manufacturing. When revising the part a design radius would be preferable to incorporate at these edges. The refined mesh also reveals that the edge hot-spots converge at a stress level of approximately 450 MPa giving a FOS of 1.35. This FOS is still high relative the other components why in a revised design it should be studied how this stress could be reduced.

9 DISCUSSION AND CONCLUSIONS

This chapter presents a discussion of the various development models derived in the thesis and the conceptual design as well as conclusions which reconnect to the thesis purpose defined in the first chapter.

9.1 Discussion

In this thesis a number of parametric design models have been produced and utilized to develop a detailed conceptual design of the front suspension and front unsprung system of Newt. A series of assumptions and simplifications have been applied to arrive at the proposed sub-system. With a progressing vehicle design the parallel workflow discussed in Chapter 1 should be applied to revise the design by updating important parameters.

The CoG position is one highly influential parameter to the anti-dive geometry implemented in the front suspension linkage. The CoG position is derived with the simple CAD model and the estimations of weight for the major components. For example, looking at the cockpit roof section which is assigned a relatively low value compared to the monocoque tub. The lesser weight is due to the reduced structural demands of the roof section however when adding a windshield, side windows, door locks etc. it is very likely that the weight increases. A heavier roof raises the centre of gravity and consequently increases the vehicles sensitivity to dive during braking thus influencing the suspension geometry.

When deriving the anti-dive suspension HP with the optimization routine various constraints are enforced to ensure that the resulting kinematic motion is as intended. In section 5.5 it is explained how the ADAMS model should be used to further analyze the vehicle behavior to revise the optimization constraints.

The anti-dive geometry is also dependent on the vehicle's brake ratio. It is derived with the ideal braking model which in turn takes input both from the CoG position but also the measurement of the tire friction coefficient. The simplified testing procedure and rough instrument resolution in these measurements introduces uncertainties concerning the friction coefficient and therefore also in the ideal brake ratio.

It is discussed in section 5.1 that the dimensioning torque and power of the motors acquired with the *acceleration* and *inclined ramp* maneuvers in the rigid vehicle model is likely to be reduced. The reduction in torque is due to that the demands of acceleration performance is lowered and a more detailed inclined ramp scenario is considered. In the detailed ramp scenario the effective inclination angle is smaller due to buoyancy and a water support propulsion system is implemented. If the motor performance requirements are lowered there may not be a need for a geared hub motor solution if it is possible to find a motor which meets the requirements. If gears however proves to be required it would be interesting to investigate if gears of a lightweight material, e.g. aluminum, could be used instead of traditional steel. For instance, basic gear dimensioning calculations for teeth root stress and surface pressure could be compared with aluminum material data. There are also various surface treatments that could be utilized to increase hardness and abrasion resistance for aluminum gears.

In an effort to reduce the weight of the front suspension there are some parts which are highly suited for topology optimization. In a topology optimization, FEA is used to determine stress levels in a part and low-stressed material is removed to save weight. In any optimization routine it is however important to be aware that the output is always highly dependent on the input and possible constraints. This means that the solution obtained is optimal based on the provided model. If the level of detail of the model fails to give an accurate representation of the real life

problem there is no reliability in the output. Calling it an optimal solution is therefore somewhat contradictory since there may likely be another just as optimal solution for a different input.

9.2 Conclusions

- After comparison with equivalent systems of different designs the initial rough conceptual hub centre and swing arm solution featured in the Rhino model is the most suited front suspension for Newt.
- The current level of development for the vehicle confines the major parts and subsystems to *detailed conceptual designs*. As the interfaces between components are iteratively being designed a workflow where component design progresses in parallel is required.
- The unique functional requirements and required custom design promotes for an in-house developed front suspension and front unsprung assembly.
- The position of the CoG has great influence on the design of the front suspension. An initial estimation of the CoG location is however sufficient to produce the thesis conceptual design. For the final design a more detailed full vehicle CAD assembly is required.
- The parametric models facilitate parameter updates and design revisions and with the suspension geometry optimization the generation of suspension HP is automated.
- If acceleration performance is a priority to the vehicle, geared hub motors are required to meet the immense torque requirements while still maintaining an acceptable weight.

10 RECOMMENDATIONS AND FUTURE WORK

This chapter contains the recommendations of more detailed development and proposed future work for the front suspension and overall design of Newt.

10.1 Recommendations

The primitive joint added to the ADAMS model restrains the roll degree of freedom keeping the vehicle leveled and preventing it from capsizing. To simulate the vehicle more accurately, especially when cornering, roll motion need to be implemented and the primitive joint removed. The balancing algorithms developed in the gyroscopic Simulink model may be implemented in ADAMS by utilizing coupled simulations.

The simulation accuracy can possibly be further improved with a more detailed representation of the aerodynamic effects. For example, the current drag force is based on an estimated C_D . With a 3D representation of the vehicle's body, computational fluid dynamics (CFD) could be utilized to derive a more accurate C_D also taking into account the influence of the unshielded rotating wheels.

Since the tire properties used in the ADAMS model are only tuned with respect to the tire dimension and vertical stiffness a valuable update would be to implement actual tire data. Either derived by testing or retrieved from the manufacturer, correct values of for instance tire lateral stiffness is essential when simulating cornering maneuvers.

With more detailed knowledge of the dimensioning loads going into the front suspension and front unsprung assembly the parts should be redesigned with focus on structural integrity. As the FOS indicates, many of the different parts are over-dimensioned and as a consequence also heavier than required. For the metal parts such as the rotor carrier and torque arm where the geometry and loading conditions are a simple topology optimization would be useful.

10.2 Future work

- Revise the rear suspension geometry with consideration to available space and derive a parametric geometry in the same manner as in the front. Implement these changes in the ADAMS model.
- Produce detailed conceptual designs of the remaining major parts of the vehicle to refine the location of the CoG and establish sub-system interfaces. Then perform a second design iteration for the suspension linkage geometry.
- Revise the ADAMS model according to updated geometry and component mass properties, also implement lateral positions of the front and rear suspension HP.
- Decide on, and simulate dimensioning load cases in ADAMS to extract dimensioning loads.
- Choose the required off-the-shelf components and establish their corresponding dimensions and design.
- Finalize the design with respect to surrounding subsystems, off-the-shelf components and detailed structural analysis.

11 REFERENCES

- Allied Motion. (2015). *AlliedMotion, Product solutions, Brushless motors, Frameless brushless torque motors*. Retrieved March 17, 2015, from <http://www.alliedmotion.com/Products/Product.aspx?p=2>
- Applimotion, Inc. (2015). *Applimotion, Product solutions, ULT Brushless Motor kits*. Retrieved March 06, 2015, from <http://www.applimotion.com/ult.php>
- Bikeblolocks. (2011). *Bikeblolocks Blog*. Retrieved October 11, 2014, from http://2.bp.blogspot.com/-Uhyvj1P_IF0/TmPRajLKIKI/AAAAAAAAAFew/nOvtZ39nWIY/s1600/ELF-Honda_3033-Ottoneroblogspot%2B%252805%2529.JPG
- BMW-Motorrad. (2004). *BMW-Motorrad, Technology in detail, Suspension, Duolever*. Retrieved October 11, 2014, from <http://www.bmw-motorrad.com/com/en/index.html>
- Cossalter, V., Lot, R., & Maggio, F. (2004, September 27). On the Braking Behavior of Motorcycles. *SAE International* .
- Cossalter, V., Lot, R., & Massaro, M. (2014). Two-Wheeled Vehicles Modelling and Simulation. In *Modelling, Simulation and Control of Two-Wheeled Vehicles* (pp. 3-40). University of Padova, Italy: John Wiley & Sons, Ltd.
- Difazio, J. (1968). *Patent No. 1274441*. Great Britain.
- Electricbike. (2014). *Electric Bike*. Retrieved January 5, 2015, from <https://www.electricbike.com/wp-content/flagallery/topaccessories/enertrac-electric-hub-motor.jpg>
- Foale, T. (1997-B). *Balancing act*. Retrieved September 28, 2014, from Tony Foale Designs: <http://www.tonyfoale.com/Articles/Balance/BALANCE.htm>
- Foale, T. (2002). *Steer for the future*. Retrieved September 25, 2014, from Tony Foale Designs: <http://www.tonyfoale.com/Articles/Steer/STEER.htm>
- Foale, T. (1997-A). *To dive or...* Retrieved September 17, 2014, from <http://www.tonyfoale.com/Articles/Dive/DIVE.htm>
- Gillespie, T. D. (1992). *Fundamentals of Vehicle Dynamics*. Pennsylvania: Society of Automotive Engineers, Inc.
- Lais, C., Lange, J., Tännidal, J., & Öun, M. (2013). *The Smite Tiger*. Stockholm: KTH Industrial Technology and Management.
- Lit Motors. (2012). *Lit Motors, Press*. Retrieved October 13, 2014, from <http://litmotors.com/press/>
- Lit Motors. (2014). *Lit Motors, Prototype build update*. Retrieved October 13, 2014, from <http://litmotors.com/prototype-build-update-4-autodesk-takeover-recap/>
- MathWorks. (2014). *MathWorks, Optimization Toolbox, Nonlinear Optimization, Constrained Optimization*. Retrieved December 18, 2014, from <http://se.mathworks.com/help/optim/ug/fmincon.html>
- Milliken, W. F., & Milliken, D. L. (1995). Suspension Geometry. In *Race car vehicle dynamics* (pp. 617-620,751-754). Warrendale, PA, U.S.A: Society of Automotive Engineers, Inc.
- Neracher, C. A. (1925). *Patent No. 1535680*. United States.

- Newt. (2013). *Newt technology*. Retrieved September 24, 2014, from NEWT: <http://newt.nu/technology>
- Nyström, Å. (2014, November 25). BEVI Teknik & Service AB. Blomstermåla. Rider Magazine. (2005). *Rider Magazine*. Retrieved October 11, 2014, from http://www.ridermagazine.com/wp-content/uploads/2005/09/2006_BMW_K1200R_frame_11.jpg
- Ringertz, U. T. (2000). *Numerical Optimization With Applications in Structural Analysis and Design*. Stockholm: KTH Department of Lightweight Structures.
- Rising, A. (2010). *ISR Brakes*. Retrieved October 13, 2014, from <http://www.isrbrakes.se/products/ns2/>
- Rothhämel, M. (2014). *Dynamics of Motorcycles*. Stockholm.
- SportbikeRider. (2012). *Sportbike Rider*. Retrieved October 10, 2014, from http://www.sportbikerider.us/CFFileServlet/_cf_image/_cfimg8483535443884505824.jpg
- Sundberg, E. (2014). *Weight Optimization of a Composite Chassis for a Multimodal Lightweight Vehicle*. Engineering Sciences. Stockholm: KTH.
- ThinGap. (2014). *Thin Gap*. Retrieved October 14, 2014, from <http://www.thingap.com/>
- Uddeholm. (2011, January 1). *Uddeholm, Alumec 89*. Retrieved March 6, 2015, from http://www.uddeholm.se/files/Alumec_89-swedish_p_R110126_e4.pdf
- Ulrich, K., & Eppinger, S. (2011). *Product Design and Development*. Columbus, OH: McGraw-Hill Higher Education.
- Wallmark, O. (2014, September 29). Researcher Electrical Conversion. Interview, (J. Lange, Interviewer).

APPENDIX I - OPTIMIZATION PRINT-OUT

This appendix contains the diagnostic print-out from the Matlab optimization routine.

Diagnostic Information

Number of variables: 6

Functions

Objective: objf_adr
Gradient: finite-differencing
Hessian: finite-differencing (or Quasi-Newton)
Nonlinear constraints: nonlcon
Nonlinear constraints gradient: finite-differencing

Constraints

Number of nonlinear inequality constraints: 5
Number of nonlinear equality constraints: 0

Number of linear inequality constraints: 0
Number of linear equality constraints: 0
Number of lower bound constraints: 6
Number of upper bound constraints: 6

Algorithm selected
interior-point

End diagnostic information

Iter	F-count	f(x)	Feasibility	First-order optimality	Norm of step
0	7	6.470440e-01	7.585e-01	1.321e-01	
1	14	4.584873e-01	0.000e+00	4.031e+00	1.047e-01
2	22	4.701103e-01	3.996e-02	1.412e+00	1.235e-02
3	30	4.758934e-01	3.370e-02	1.206e+00	7.490e-03
4	38	4.785240e-01	2.845e-03	4.567e+00	4.100e-02
5	46	4.739312e-01	0.000e+00	5.211e-01	1.229e-02
6	53	4.701436e-01	0.000e+00	5.825e-01	1.855e-02
7	64	4.703415e-01	0.000e+00	4.633e-01	9.647e-02
8	84	4.704653e-01	0.000e+00	1.027e-01	9.986e-03
9	91	4.599790e-01	0.000e+00	1.783e+00	1.146e-01
10	98	4.345313e-01	0.000e+00	4.400e-01	5.535e-01
11	105	4.187387e-01	0.000e+00	5.179e-01	4.831e+00
12	112	3.483337e-01	0.000e+00	5.289e-01	1.295e+01
13	119	2.829885e-01	0.000e+00	1.221e+00	9.510e+00
14	127	2.574269e-01	0.000e+00	1.383e+00	3.418e+00
15	135	2.463297e-01	0.000e+00	1.444e+00	1.396e+00
16	142	2.452518e-01	0.000e+00	1.431e+00	2.659e-01
17	149	2.464559e-01	0.000e+00	1.429e+00	3.545e-02
18	156	2.482174e-01	0.000e+00	1.420e+00	8.406e-02
19	163	2.496759e-01	0.000e+00	1.409e+00	7.268e-02
20	170	2.517975e-01	0.000e+00	1.387e+00	5.634e-02
21	177	2.553632e-01	0.000e+00	8.965e-01	7.826e-03
22	184	2.596018e-01	0.000e+00	3.404e-01	6.530e-02
23	191	2.628791e-01	0.000e+00	1.184e-01	4.331e-02
24	198	2.643837e-01	0.000e+00	3.867e-02	7.219e-03
25	205	2.648770e-01	0.000e+00	2.000e-02	2.696e-03
26	212	2.409632e-01	0.000e+00	3.011e-01	9.470e-01
27	219	2.232607e-01	0.000e+00	2.026e-01	7.503e-01
28	226	2.268434e-01	0.000e+00	1.676e-01	1.773e-01
29	233	2.265772e-01	0.000e+00	1.660e-01	1.375e-03

30	240	2.262913e-01	0.000e+00	1.653e-01	6.068e-03
31	247	2.258486e-01	0.000e+00	1.674e-01	6.539e-03
32	254	2.248811e-01	0.000e+00	1.772e-01	3.022e-03
33	261	2.229697e-01	0.000e+00	1.836e-01	1.341e-02
34	268	2.210331e-01	0.000e+00	1.600e-01	1.683e-02
35	275	2.199726e-01	0.000e+00	1.500e-01	9.597e-03
36	282	2.194797e-01	0.000e+00	1.582e-01	3.772e-03
37	289	2.192471e-01	0.000e+00	1.621e-01	1.497e-03
38	296	2.191342e-01	0.000e+00	1.640e-01	6.473e-04
39	303	2.190780e-01	0.000e+00	1.650e-01	3.026e-04
40	310	2.190492e-01	0.000e+00	1.655e-01	1.471e-04
41	317	2.190339e-01	0.000e+00	1.658e-01	7.605e-05
42	324	2.190254e-01	0.000e+00	1.659e-01	4.163e-05
43	331	2.190205e-01	0.000e+00	1.660e-01	2.504e-05

Local minimum possible. Constraints satisfied.

fmincon stopped because the size of the current step is less than the selected value of the step size tolerance and constraints are satisfied to within the selected value of the constraint tolerance.

<stopping criteria details>

Swing arm: L1 = 0.46768
Torque arm: L2 = 0.19222
Torque strut: L3 = 0.36120
Pivot dist.: L4 = 0.15806
Pivot angle: Phi = -29.63210
Swing mount: y0s = 0.37046

Coordinates at neutral position in local coordinate system:

Ax = 0.46446 Ay = -0.05476
Bx = 0.43851 By = 0.13582
Cx = 0.07815 Cy = 0.13739
Torque arm angle: gamma = 7.50710
Torque strut angle: theta3 = 89.75107

Coordinates at neutral position in global coordinate system:

Ox = -0.46446 Oy = 0.37046
Ax = 0.00000 Ay = 0.31570
Bx = -0.02595 By = 0.50628
Cx = -0.38631 Cy = 0.50784

APPENDIX II - PRELOAD ITERATIONS

This appendix contains the figures showing how the correct pre-load is found by manual iterations.

With no pre-load the chassis markers starts the equilibrium simulation at the correct ride height of 170 mm. When the vehicle puts the weight to the ground the springs compresses thus lowering the vehicle see Figure A-II.1.

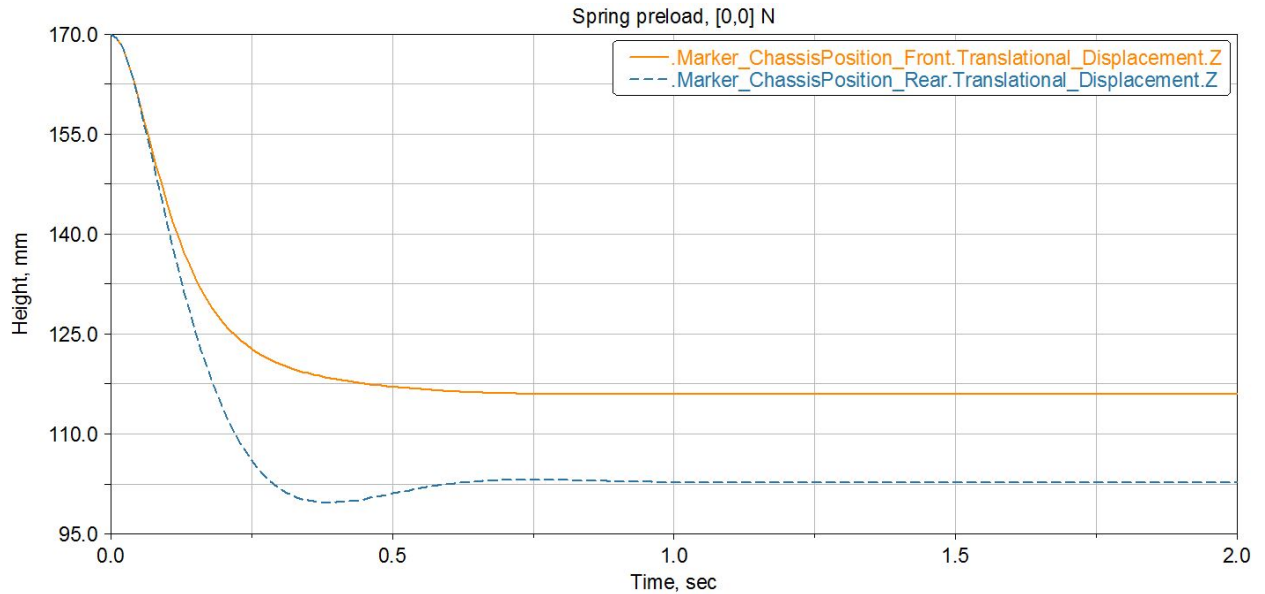


Figure A-II.1. The first setting with no pre-load of the springs.

When increasing the spring pre-load incrementally as displayed by Figure A-II.2, Figure A-II.3 and Figure A-II.4 the markers return to their initial position.

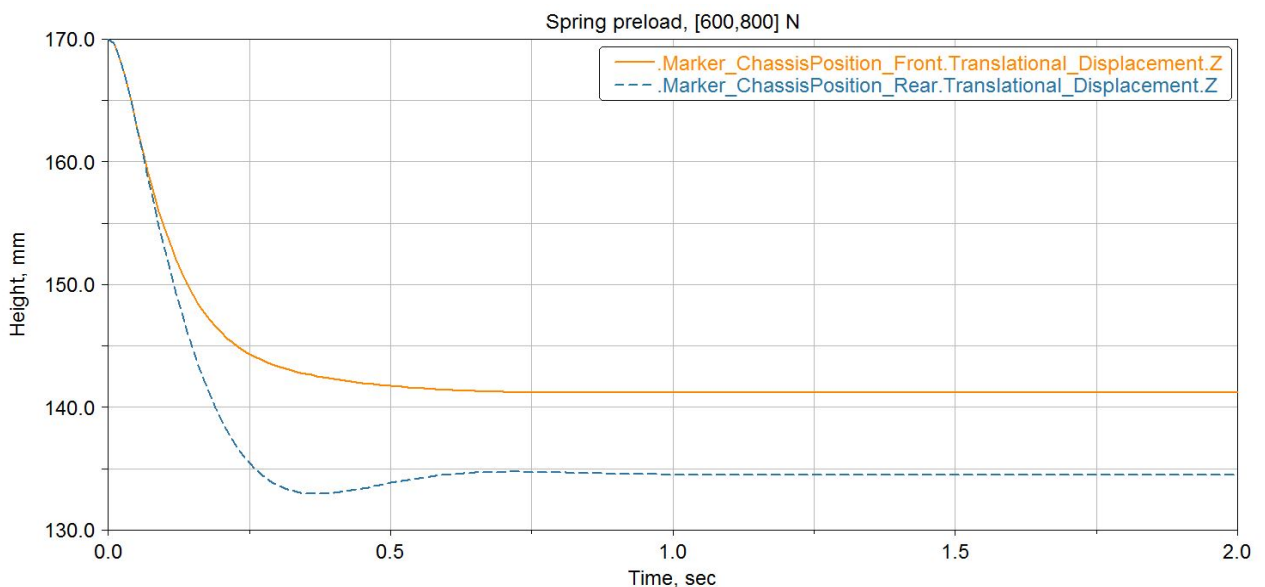


Figure A-II.2. The second setting with a pre-load of 600 N in the front and 800 N in the rear.

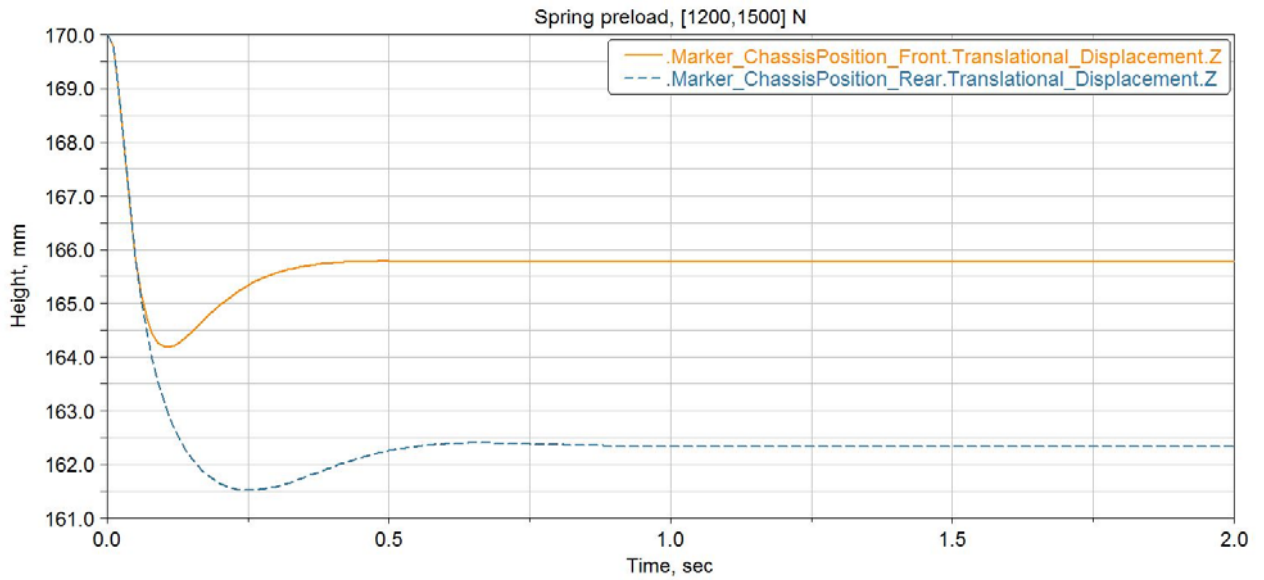


Figure A-II.3. The third setting with a pre-load of 1200 N in the front and 1500 N in the rear.

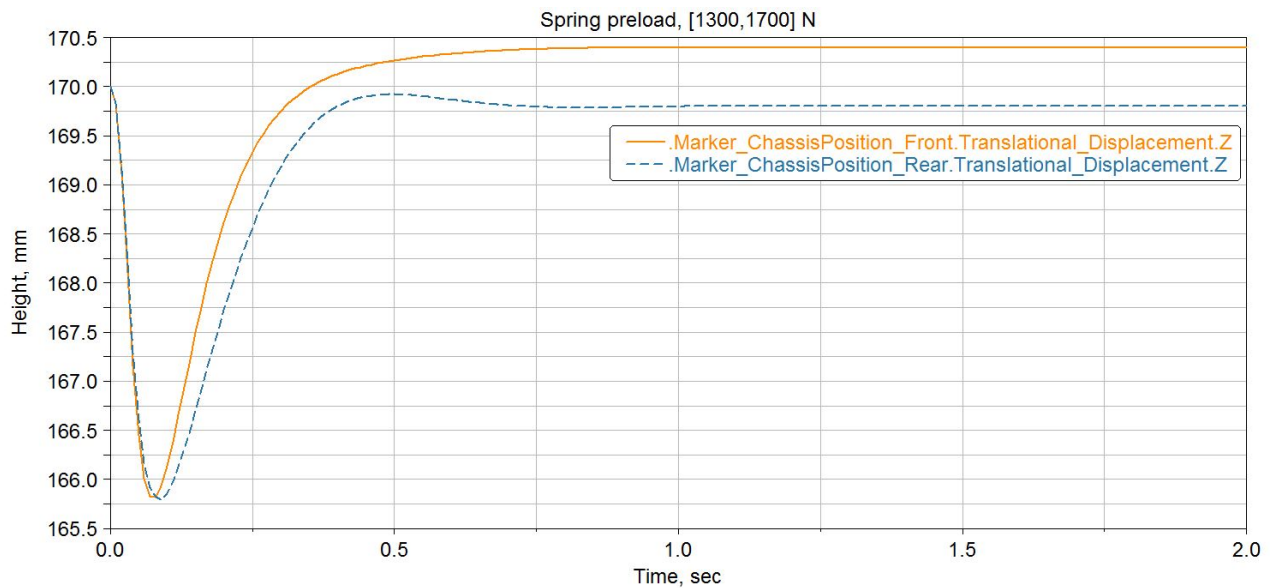


Figure A-II.4. The fourth and final iteration for the spring pre-load, 1300 N in the front and 1700 N in the rear. The small deviation of < 0,5 mm from ride height of 170 mm is negligible and also the difference of 0.6 mm for the front and rear marker.

APPENDIX III - STRUCTURAL ANALYSIS

This appendix contains the resulting stress plots of the simplified structural analysis conducted on the parts.

The load case used for the structural analysis is a combination of braking torque and vertical load from hitting a pot-hole. When the brakes are engaged a reaction moment arise in the axle-hub assembly as it tries to rotate with the wheel. Rotation is constrained with the steering axle, transverse axle, torque arms and ultimately the torque struts.

In the different parts' analysis the vertical load of 2800 N is rounded up to 3000 N and a braking torque of 516 Nm is applied. For parts operating in pairs such as the torque arms, disc carriers and caliper brackets it is assumed that the total braking torque is divided equally among them. This means that half of the total braking force, 258 Nm is applied to the individual part.

Convergence analysis with at threshold value of 10% has been implemented for the parts were convergence could be acquired. The mesh in the parts which experience divergence due to stress concentrations have been manually refined in the areas of interest.

Steering axle

The steering axle is unable to converge using the program controlled adaptive meshing method as the stress concentration seen in Figure A-III.1 spikes and causes divergence. The remaining stress field does however converge when refining the mesh why the stress peak may be ignored.

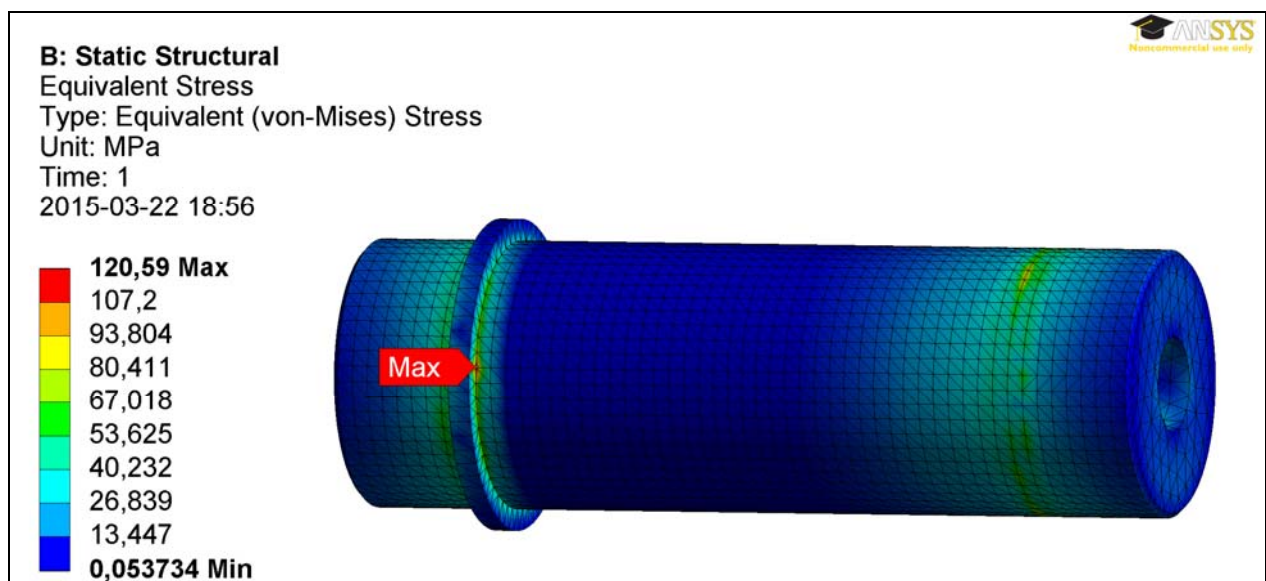


Figure A-III.1. The stress field in the steering axle.

Transverse axle

The transverse axle analysis is comprised of two parts, one piece of the transverse axle and the axle center hub. The bolted connection between the parts is simplified by a bonded contact region and the analysis implements symmetry to reduce the computation time. A relatively uniform and converged stress field arise in the axle. A stress concentration does however occur at the edge of a support region which causes divergence in the convergence analysis see FigureA-III.2.

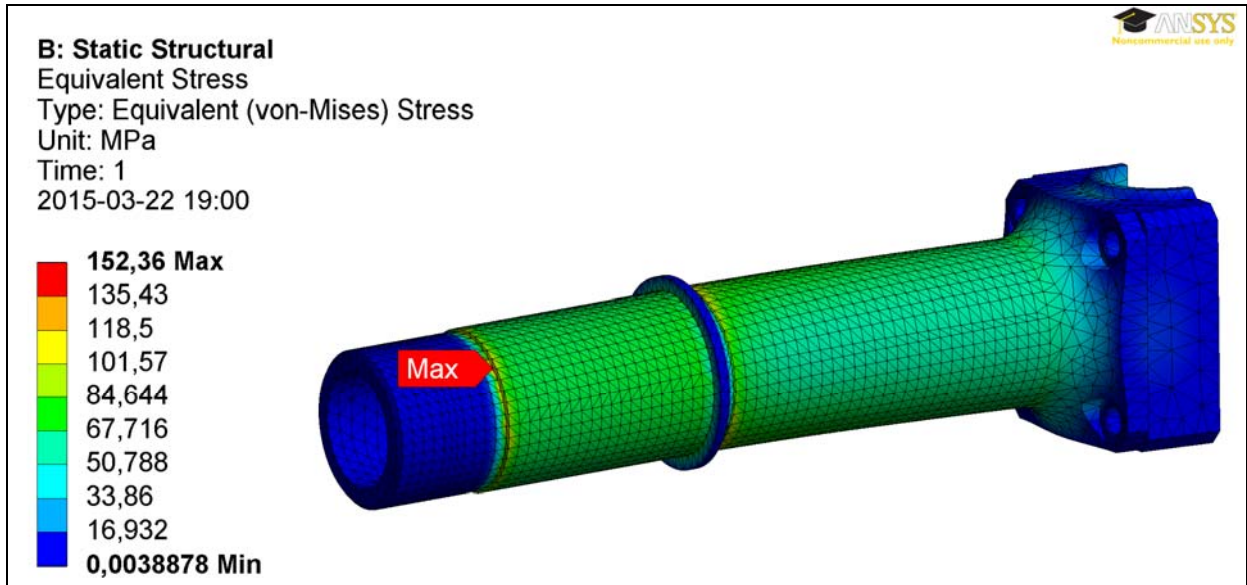


Figure A-III.2. The stress field in the transverse axle.

Disc carrier

The disc carrier feature a rotational symmetric geometry though non-symmetry in terms of applied loads. To be able to apply symmetric conditions all aspects of the model needs symmetry why it cannot be implemented here. Figure A-III.4 only illustrates the stresses in a section of the part as the resulting stress field is approximately uniform. The disc carrier is able to converge with a threshold of 3%.

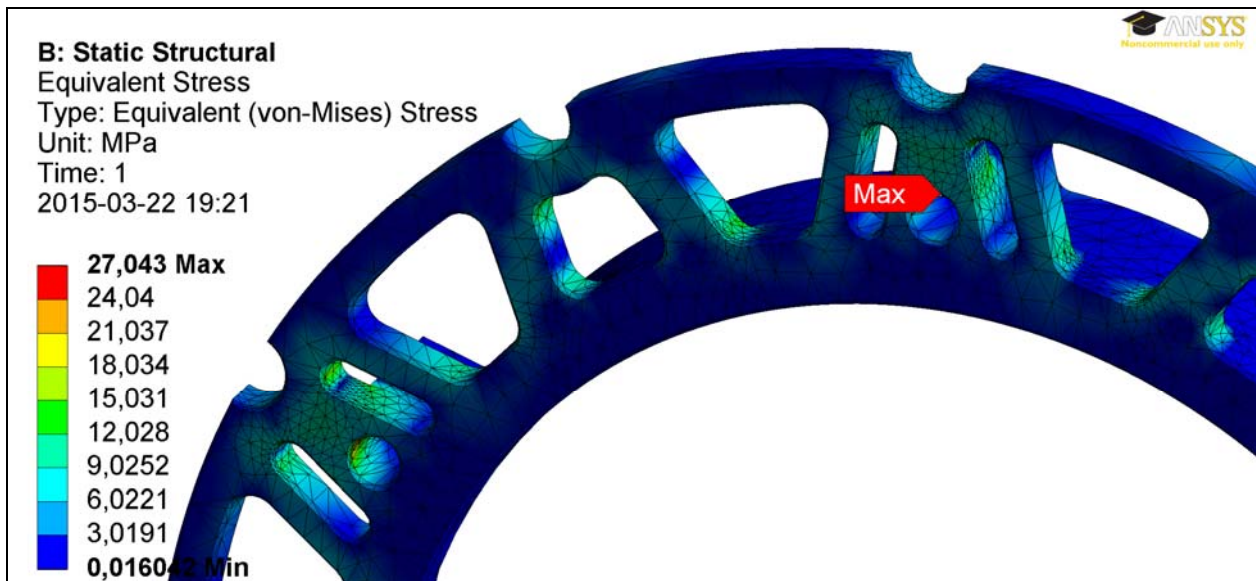


Figure A-III.4. The converged stress field in the disc carrier.

Rotor carrier

Similar to the disc carrier the rotor carrier is rotational symmetric in geometry though non-symmetric in the applied loads. With an almost uniform stress field seen in Figure A-III.6 the model converges within 9%.

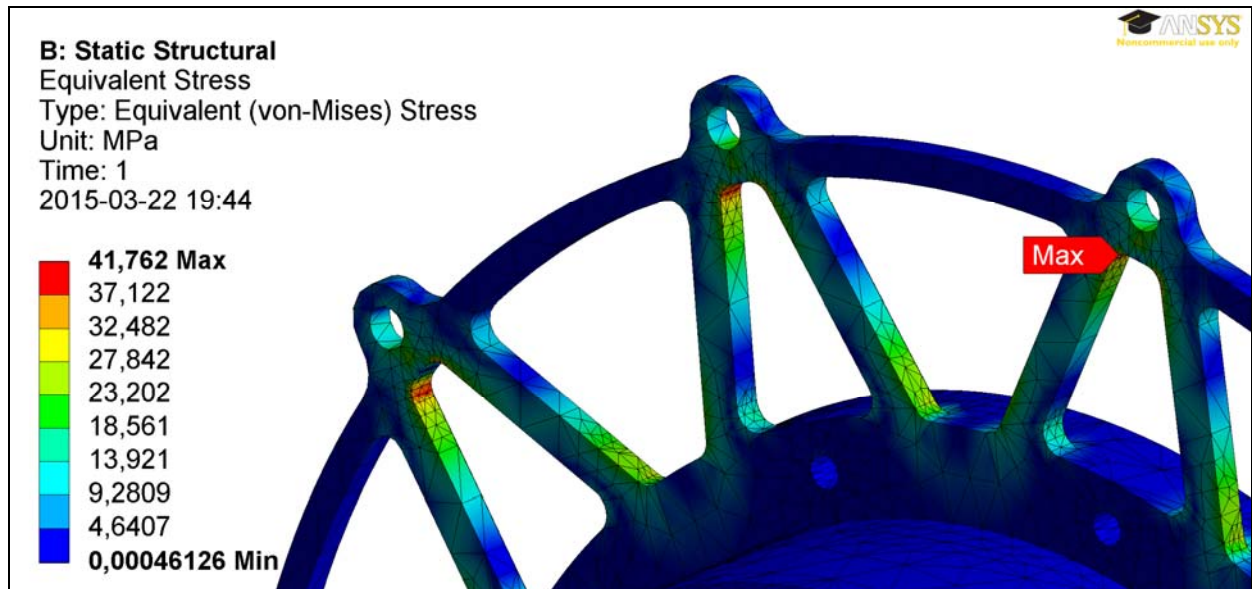


Figure A-III.6. The converged stress field in the rotor carrier.

Wheel hub

The wheel hub feature full symmetry across the vehicle centerline why it is split down the middle. Again a bonded contact region represents the bolted connection between the parts. The maximum stress arise at an edge of the steering axle hub covered by the outer hub illustrated by Figure A-III.3. The max stress in the model is also an edge stress concentration causing divergence when refining the mesh however the overall stress field converges in the analysis.

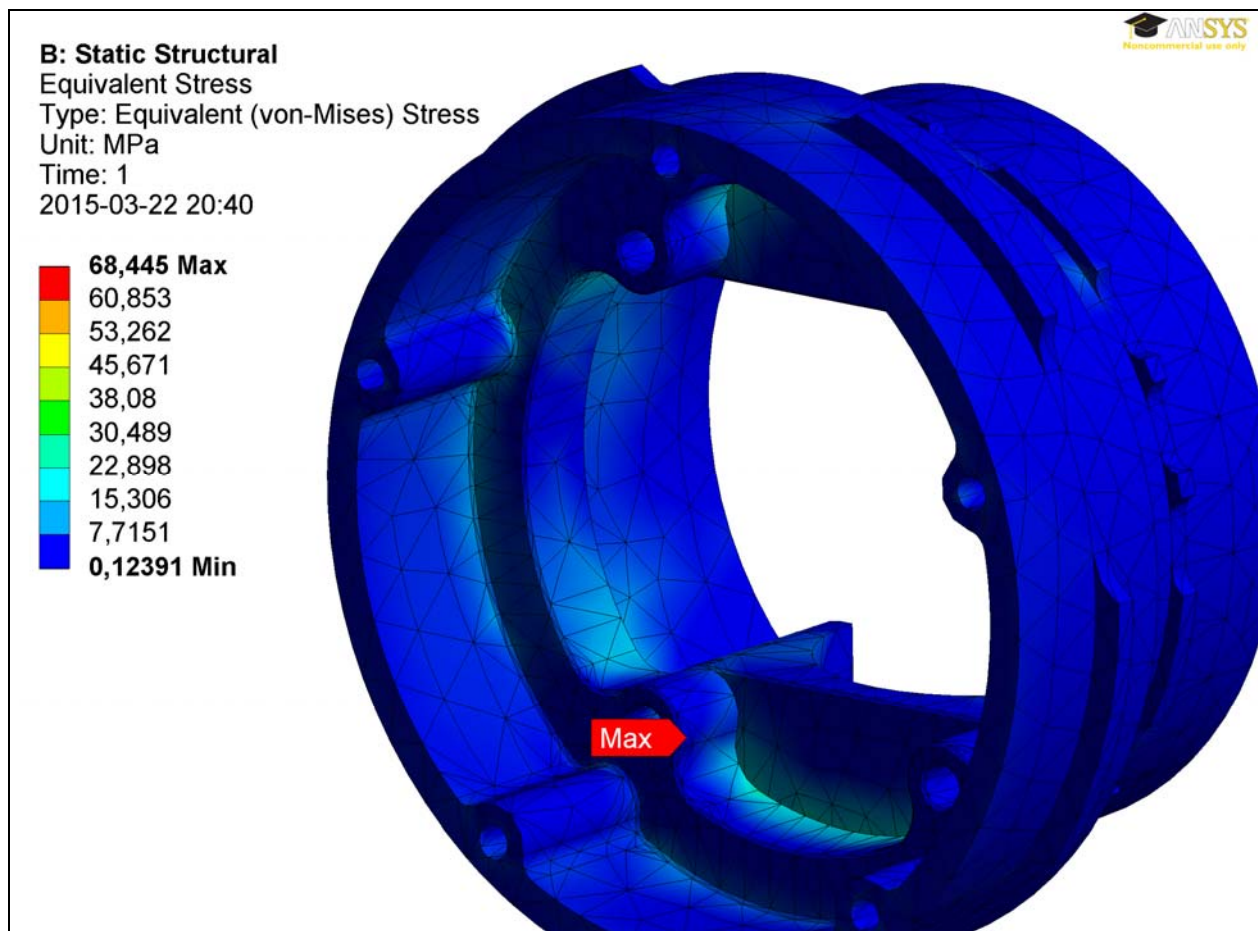


Figure A-III.3. The stress field in the wheel hub.

Motor cover

The motor cover is modeled as a single part and due to the non-symmetric loading it is not possible to simplify with symmetric conditions. With manual refinement of the mesh both overall and at highly stressed areas a convergence within 1.5% is archived. The resulting stress field is approximately uniform why only a half section is displayed in Figure A-III.7.



Figure A-III.7. The converged stress field for the motor cover.

Caliper bracket

The caliper bracket is another part with a converged stress field within 2%.

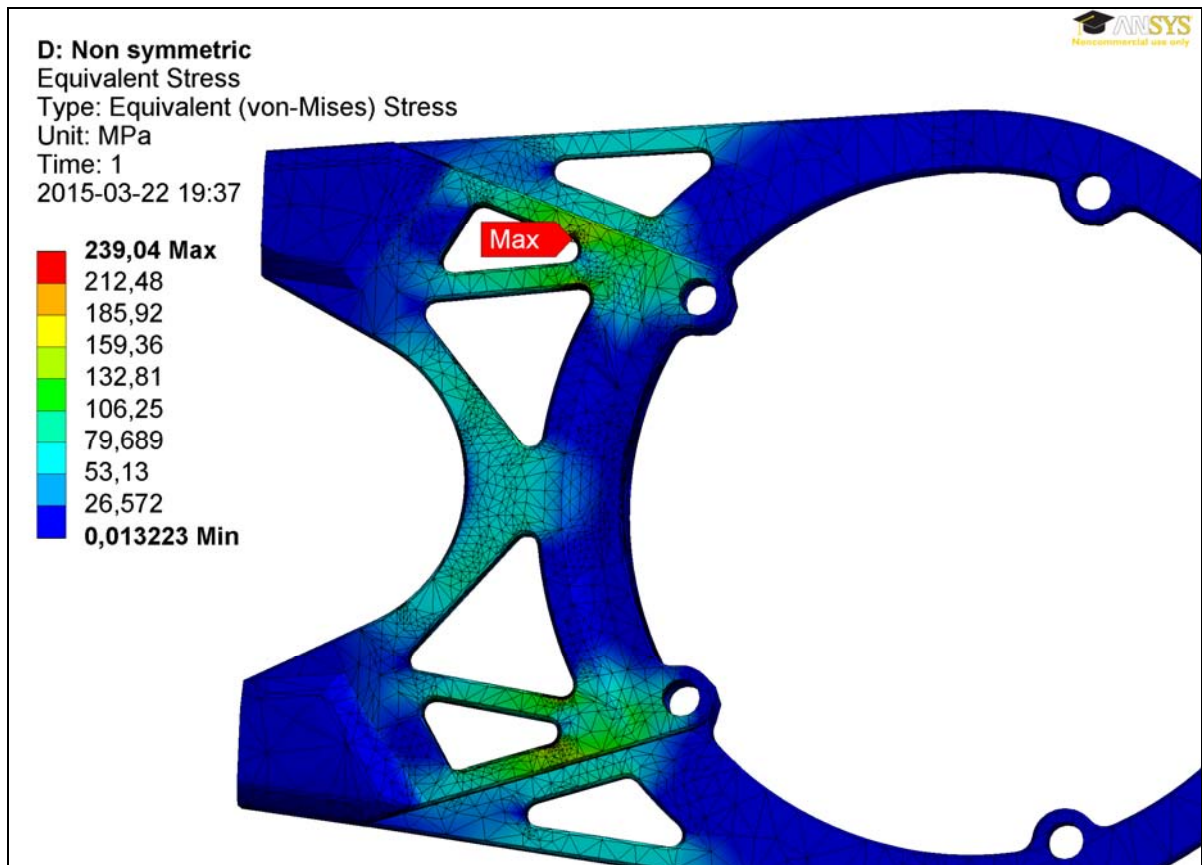


Figure A-III.5. The converged stress field in the caliper bracket.

Wheel center

The two pieces of the wheel center are assembled and the bolted connection is represented by a bonded contact region. A section of the overall converged uniform stress field is illustrated in Figure A-III.8 though a stress concentration arise at a line edge causing divergence when refining the mesh.

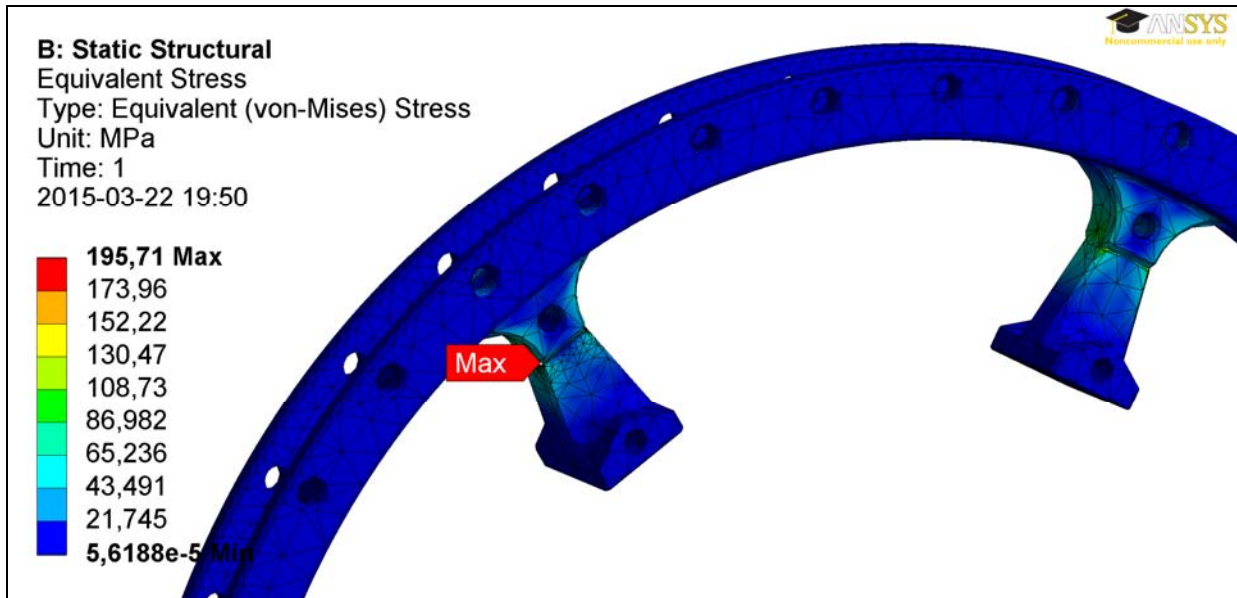


Figure A-III.8. The stress field in a segment of the wheel center.

APPENDIX IV - KINEMATIC ANALYSIS M-CODE

Main program

```
%% FILE INFORMATION

% File name: swingarm_kinematics    Created: 2014-10-20
% Master Thesis: Newt front suspension development
% Author: Joakim Lange
% Last updated: 2015-02-12
%
% This script is based on a 2D analysis on the kinematics of Newts front
% suspension. The mathematical model is derived and presented in the report

clc
clear all
close all

%% VARIABLES & PARAMETERS
travel = 0.1;           % [m] Total travel of wheel +- 50 mm
res     = 500;          % [-] Simulation resolution
step    = travel/res;   % [m] Step size of simulation
delta   = -travel/2:step:travel/2; % [m] Wheel displacement vector

%%%%%%%%%%%%%%%%%%%%%%%%%%%%%%%%%%%%%%%%%%%%%%%%%%%%%%%%%%%%%%%%%%%%%%%% 4 bar linkage model %%%%%%%%%%
% Geometry
y0s     = 0.318;        % [m] Ground to swing arm pivot
y0      = y0s+delta;   % [m]
yA      = 0.3157;      % [m] Wheel radius
% Linkage lengths
L1 = 0.42;             % [m] Swing arm
L3 = 0.45;             % [m] Torque strut
L2 = 0.15;             % [m] Torque arm
L4 = 0.12;             % [m] Pivot points distance
% Linkage angles
phid = 10;            % [deg] Pivot points angle
% Converting to radians
phi = degtorad(phid); % [rad]

% RESULTS AFTER OPTIMIZATION
% %%%%%%%%% 4 bar linkage model %%%%%%%%%
% % Geometry
% y0s     = 0.37046;    % [m] Ground to swing arm pivot
% y0      = y0s+delta;  % [m]
% yA      = 0.3157;    % [m] Wheel radius
% % Linkage lengths
% L1 = 0.46768;        % [m] Swing arm
% L3 = 0.36120;        % [m] Torque strut
% L2 = 0.19222;        % [m] Torque arm
% L4 = 0.15806;        % [m] Pivot points distance
% % Linkage angles
% phid = -29.63210;    % [deg] Pivot points angle
% % Converting to radians
% phi = degtorad(phid); % [rad]
```

```

var    = [delta;y0];
param = [L1,L2,L3,L4,phi,y0s,yA];

%% EQUATIONS - FOUR BAR LINKAGE MODEL
% Linkage equations (based on Sine and Cosine rule)
theta1 = acos((y0-yA)/L1);
theta2 = pi-theta1;
Ld = sqrt(L4^2+L1^2-2*L1*L4*cos(phi+theta2));
alpha = asin(sin(theta2+phi)./Ld*L1);
for n = 1:numel(y0)-1
    if alpha(n) < alpha(n+1)
        alpha(n) = pi-alpha(n);
        if n == numel(y0)-1
            alpha(n+1) = pi-alpha(n+1);
        end
    end
end
beta = acos((L3^2+Ld.^2-L2^2)./(2*L3*Ld));
theta3 = alpha+beta+phi;
% Coordinates
k = ones(1,numel(y0));
Ox = 0*k;           Oy = 0*k;
Ax = L1*sin(theta1);   Ay = -L1*cos(theta1);
Cx = -L4*sin(phi)*k;   Cy = L4*cos(phi)*k;
Bx = Cx+L3*sin(theta3); By = Cy-L3*cos(theta3);
gamma = atan((Ax-Bx)./(By-Ay));
%gamma = acos((By-Ay)/L2);
Ex = Ax; Ey = Ay-yA;

angf = [theta1; theta2; theta3; gamma];
coordfx = [Ox;Ax;Bx;Cx;Ex];
coordfy = [Oy;Ay;By;Cy;Ey];

%% EQUATIONS - ANTI-DIVE MODEL
% Distance equations
xi = L2*sin(gamma);
yi = L2*cos(gamma);
% b = Lv1, a = Lv2
b = (yi-xi./sin(theta1).*cos(theta1))./(sin(theta3)./...
    sin(theta1).*cos(theta1)-cos(theta3));
a = (b.*sin(theta3)+xi)./sin(theta1);
% X1 = ICx, Y1 = ICy
X1 = a.*sin(theta1); Y1 = a.*cos(theta1); % X & Y distances for virtual
pivot
% X3 = b.*sin(theta3); Y3 = b.*cos(theta3); % X & Y distance for upper
triangle used to compare with lower
% diff = X1-(X3+xi); % Check that it is correct
(==0)
% diff2 = Y1-(Y3+yi);

% Geometry
wb = 2.5;
xrw = wb-Ax; % [m] Horizontal distance 4 link origin to rear
wheel center
xCoG = 1.409-median(Ax); % [m] Horizontal distance 4 link origin to CoG
yCoGs = 0.56; % [m] Vertical distance from ground to CoG
CoG = [xCoG,yCoGs,xrw];

FB_ratio = 1; % [-] Front brake ratio (at severe braking only
front brake will be used)

```

```

% FB_ratio = (1-0.375);

yCoG = yCoGs+delta; % [m] CoG height over ground during
travel
ksi = atan((Y1+yA)./X1); % [rad] Angle to anti-dive force line
adr = FB_ratio*tan(ksi).*wb./yCoG; % [-] Anti-dive ratio according to
Milliken & Milliken
hadr = tan(ksi).*(xrw+Ax); % [m] Plot parameter

% Coordinates (4 bar linkage coordinate system)
Vpx = Ax-X1;
Vpy = Ay+Y1;

dive = [ksi;hadr;adr;Vpx;Vpy];

%% PLOTTING
anim = 0; % Show animation, Yes = 1, No = 0
kinematics_plot(var,param,angf,coordfx,coordfy,dive,anim,CoG)

```

Plot function file

```

function [] = kinematics_plot(var,param,angf,coordfx,coordfy,dive,anim,CoG)
% This function file named kinematics_plot plots the data generated in
% swingarm_kinematics.m

%% SETTING VALUES FROM swingarm_kinematics.m
% var = [delta;y0];
delta=var(1,:); y0=var(2,:);
% param = [L1 L2 L3 L4 phi xCoG yCoG, y0s yA];
y0s=param(6); yA=param(7); xCoG=CoG(1); yCoGs=CoG(2); yCoGc=yCoGs-y0s;
xrw=CoG(3:end);
% angf = [thetal theta2 theta3 gamma]s
thetal=angf(1,:); theta2=angf(2,:); theta3=angf(3,:); gamma=angf(4,:);
% coordfx = [Ox;Ax;Bx;Cx;Ex];
% coordfy = [Oy;Ay;By;Cy;Ey];
Ox=coordfx(1,:); Ax=coordfx(2,:); Bx=coordfx(3,:); Cx=coordfx(4,:);
Ex=coordfx(5,:);
Oy=coordfy(1,:); Ay=coordfy(2,:); By=coordfy(3,:); Cy=coordfy(4,:);
Ey=coordfy(5,:);
% dive = [ksi;hadr;adr;Vpx;Vpy];
ksi=dive(1,:); hadr=dive(2,:); adr=dive(3,:); Vpx=dive(4,:); Vpy=dive(5,:);

%% RECALCS
i = 1;
thetal_d = radtodeg(thetal);
theta3_d = radtodeg(theta3);
gamma_d = radtodeg(gamma);
delta_mm = delta*1e3;

%% SUSPENSION ANGLES
figure(i)
i = i+1;
% subplot(3,2,5);
% plot(delta_mm,thetal_d,'Color',[0 0 1],'LineWidth',2); % Suspension angles
% title('Swing arm angle')
% xlabel('Wheel Travel [mm]')
% ylabel('Angle [deg]')
% legend('\theta_{1}')
% subplot(3,2,6)
% plot(delta_mm,theta3_d,'Color',[1 0 0],'LineWidth',2); % Suspension angles

```

```

% title('Torque strut angle')
% xlabel('Wheel Travel [mm]')
% ylabel('Angle [deg]')
% legend('\theta_{3}')
%grid on
% subplot(3,2,4);

%subplot(2,1,2)                                %FOR REPORT FIGURES

plot(delta_mm,gamma_d,'Color',[0 0 0],'LineWidth',2); % Suspension angles
title('Torque arm angle','FontSize',18)
xlabel('Wheel Travel, mm','FontSize',18)
ylabel('Angle, {\circ}','FontSize',18)
legend('\gamma','FontSize',18)

set(gca,'FontSize',18);                        %FOR REPORT FIGURES

%% WHEEL DISPLACEMENT
% subplot(3,2,3);

% subplot(2,1,1)                                %FOR REPORT FIGURES
% plot(delta_mm,Ax*1000,'Color',[0 0 1],'LineWidth',2); % Wheel
displacement, x-direction
% axis([min(delta_mm)-2 max(delta_mm)+2 min(Ax*1000)-2 max(Ax*1000)+1]);
% title('Horizontal displacement of wheel contact point','FontSize',24)
% xlabel('Wheel Travel, mm','FontSize',24)
% ylabel('Displacement, mm','FontSize',24)
% set(gca,'FontSize',24);
% grid on

%set(gca,'FontSize',18);                        %FOR REPORT FIGURES

%% ANTI-DIVE GEOMETRY
%subplot(3,2,2);
hold on
figure(i)
i = i+1;
plot(delta_mm,adr,'LineWidth',2);
hold on
title('Anti-Dive','FontSize',24)
xlabel('Wheel Travel, mm','FontSize',24)
ylabel('Ratio of anti-dive','FontSize',24)
legend('ADR')
set(gca,'FontSize',24);
%% ANIMATION
% Setting up the tire and joints plot data
xf = Ax(1);   yf = Ay(1); r = yA;
xr = -xrw(1); yr = Ay(1);
[xp,yp] = circle(r);
X0 = [Ox(1) Ax(1) Bx(1) Cx(1)];
Y0 = [Oy(1) Ay(1) By(1) Cy(1)];

if anim == 1 % Only run animation if chosen
    figure(i)
    i = i+1;
    xgr = [-2.8 1.1];

    %xgr = [-0.4 1.1];

    ygr = [1 1];

```

```

% INITIATING THE FIGURE
% Linkages, joints & ground
h(1) = plot(X0,Y0,'Color',[1 0 0],'LineStyle','-','LineWidth',3);
% Linkages
hold on
h(2) = plot(X0,Y0,'ko','markerfacecolor',[0 0 0]);
% Joints
h(3) = plot(xf+xp,yf+yp,'k','LineWidth',2);
% Front Tire
h(4) = plot(xr+xp,yr+yp,'k','LineWidth',2);
% Rear Tire
h(5) = plot(xgr,Ey(1)*ygr,'k','LineWidth',1);
% Animated ground in contact to wheel
plot(xgr,Ey(1)*ygr,xgr,Ey(end)*ygr,'Color',[0 0 0],'LineStyle','--',
'LineWidth',1); % Fixed ground at bump/droop
plot(xgr,-y0s*ygr,'k','LineStyle',':','LineWidth',1);
% Fixed ground at ride height
plot(Ax,Ay,Bx,By,'Color',[0 0 0],'LineStyle','--','LineWidth',3);
% Traveled distance of outer joints
axis([-2.8 0.9 -0.55 0.6])
% Setting axis boundaries

%axis([-0.4 0.9 -0.55 0.6])
% Setting axis boundaries

axis equal
% Scaling x & y axis 1:1
title('Swing arm suspension kinematics animation','FontSize',24)
% Title
% Anti-dive geometry
g(1) = plot([-xrw(1) Ex(1)],[hadr(1)-y0(1) Ey(1)],'k','LineStyle','-.',
'LineWidth',1); % Contact patch to IC and rear wheel centerline
g(2) = plot([Vpx(1) Bx(1)],[Vpy(1) By(1)],'k','LineStyle','-.',
'LineWidth',1); % Torque strut to IC
g(3) = plot([Vpx(1) Ax(1)],[Vpy(1) Ay(1)],'k','LineStyle','-.',
'LineWidth',1); % Swing to IC
g(4) = plot(Vpx(1),Vpy(1),'ko','markerfacecolor',[1 1 1]);
% IC
plot(-xCoG,yCoGc,'ko','markerfacecolor',[0 0 0]);
% CoG
str1 = 'CoG';
% CoG
text(-xCoG-0.1,yCoGc+0.15,str1)
% CoG
g(5) = plot([-xCoG,-xrw(1)],yCoGc*ygr,'k','LineStyle','-.',
'LineWidth',1); % CoG to rear wheel
g(6) = plot(-xrw(1)*ygr,[-y0(1) 1.5],'k','LineStyle','-.','LineWidth',1);
% Rear wheel centerline
g(7) = plot(-xrw(1),hadr(1)-y0(1),'ko','markerfacecolor',[1 1 1]);
% AD force line intersection with rear wheel centerline

% UPDATING THE FIGURE (animating motion)
press = waitforbuttonpress;
if press == 1 || press == 0
for n = 1:numel(y0)
% frame = getframe;
% im = frame2im(frame);
% [imind,cm] = rgb2ind(im,256);
% if n == 1;
% imwrite(imind,cm,'kinematic.gif','gif','Loopcount',inf);
% else
% imwrite(imind,cm,'kinematic.gif','gif','WriteMode','append');
% end
end

```

```

xf = Ax(n); yf = Ay(n);
xr = -xrw(n);
hX = [Ox(n) Ax(n) Bx(n) Cx(n)];
hY = [Oy(n) Ay(n) By(n) Cy(n)];
gX = [Vpx(n) Ex(n) Bx(n) Ax(n)];
gY = [Vpy(n) Ey(n) By(n) Ay(n)];

set(h(1), 'XData', hX, 'YData', hY)
set(h(2), 'XData', hX, 'YData', hY)
set(h(3), 'XData', xf+xp, 'YData', yf+yp)
set(h(4), 'XData', xr+xp, 'YData', yf+yp)
set(h(5), 'XData', xgr, 'YData', Ey(n)*ygr)
set(g(1), 'XData', [-xrw(n), gX(2)], 'YData', [hadr(n)-y0(n), gY(2)])
set(g(2), 'XData', [gX(1) gX(3)], 'YData', [gY(1) gY(3)])
set(g(3), 'XData', [gX(1) gX(4)], 'YData', [gY(1) gY(4)])
set(g(4), 'XData', Vpx(n), 'YData', Vpy(n))
set(g(5), 'XData', [-xCoG, -xrw(n)])
set(g(6), 'XData', -xrw(n)*ygr, 'YData', [-y0(n) 1.5])
set(g(7), 'YData', hadr(n)-y0(n))
drawnow
end
else
    close(i-1)
end
end

end

```

Generating circle file

```

function [xp,yp] = circle(r)
% x and y are the coordinates of the center of the circle
% r is the radius of the circle
% 0.01 is the angle step, bigger values will draw the circle faster but
% you might notice imperfections (not very smooth)
ang = 0:0.01:2*pi;
xp = r*cos(ang);
yp = r*sin(ang);
end

```